

CLASSY XXXX: Radiation Transfer Modeling of UV light through Outflows in Local Star-Forming Galaxies

MASON HUBERTY,¹ CODY CARR,¹ CLAUDIA SCARLATA,¹ XINFENG XU,² TIM HECKMAN,² DANIELLE BERG,³ STÉPHANE CHARLOT,⁴ JOHN CHISHOLM,³ ALAINA HENRY,^{2,5} BETHAN JAMES,⁶ CRYSTAL MARTIN,⁷ MATILDE MINGOZZI,⁵ AND ET AL. WHOEVER ELSE IS INTERESTED!

¹ Minnesota Institute for Astrophysics, University of Minnesota, Minneapolis, MN 55455, USA

² Center for Astrophysical Sciences, Department of Physics Astronomy, Johns Hopkins University, Baltimore, MD 21218, USA

³ Department of Astronomy, The University of Texas at Austin, 2515 Speedway, Stop C1400, Austin, TX 78712, USA

⁴ Sorbonne Université, CNRS, UMR7095, Institut d’Astrophysique de Paris, F-75014, Paris, France

⁵ Space Telescope Science Institute, 3700 San Martin Drive, Baltimore, MD 21218, USA

⁶ AURA for ESA, Space Telescope Science Institute, 3700 San Martin Drive, Baltimore, MD 21218, USA

⁷ Department of Physics, University of California, Santa Barbara, Santa Barbara, CA 93106, USA

ABSTRACT

Massive outflows are an important component of a galaxy’s evolution, regulating star formation and affecting the dynamics of the surrounding media. Extracting outflow information from absorption spectra is difficult, but radiation transfer modeling offers an insight into these processes. As such, we analyze the signatures of galactic outflows in the spectra of local ultraviolet star-forming galaxies in the CLASSY survey using a semi-analytical line transfer model. We focus on the resonant lines of several ionization states of silicon that trace cool and warm gas, in order to study the geometric and physical characteristics of the outflowing gas. From the model constraints, we estimate the mass outflow rates for these galaxies and look for trends with other galactic properties. We compare our estimated relationships with those in previously established literature, and speculate about reasons for similarities and deviations between this work and others. In addition, we derive momentum and energy outflow rates. We find that our semi-analytical method captures the same trends as Gaussian fitting techniques with regards to outflow rates; however the magnitude of these values often differs. Our work also reiterates the positive correlation between the mass outflows rate and star-formation rates. These results also suggest that the analyzed star-forming galaxies host momentum driven, as opposed to energy driven outflows.

1. INTRODUCTION

The mass ejection of gas into the circumgalactic medium via galactic outflows is omnipresent in star-forming galaxies (e.g. Shapley et al. 2003, Martin 2005). This phenomenon heavily regulates star-formation in galaxies, and thus is a large influence in the study of galactic evolution (Hopkins et al. 2014). One of the defining characteristics of outflows is the mass outflow rate, and numerous techniques have been used in the past to attempt to estimate this physical parameter for a diverse background of galaxies (e.g. Heckman et al. 2015, Chisholm et al. 2017, Xu et al. 2022). Mass outflow rates vary substantially across different galaxies and models, not only because outflow geometry can vary from biconical to spherical (e.g. Carr et al. 2021), but because the mass outflow rate technically varies with radius inside the outflow (Chisholm et al. 2017). That said, determining the relationships between the mass

outflow rate and other properties of a galaxy is useful in understanding how outflows behave in different environments.

The absorption and emission features originating from the outflowing gas observed in the spectra of outflows depend on numerous parameters such as the gas optical depth, outflow geometry, and dust opacity. This complexity demands high-spectral resolution observations to distinguish the spectral details and provide tighter constraints on the underlying physics governing the radiation transfer (Carr et al. 2022). A data set that provides such opportunity to model these galactic properties with radiation transfer theory is the COS Legacy Archive Spectroscopy Survey (CLASSY as presented in Berg et al. 2022).

In Xu et al. (2022), Gaussian profiles were used to model the absorption and emission lines of the outflows identified in the spectra of CLASSY galaxies. These models estimate the CLASSY outflow velocities, gas

Table 1: Atomic Data for Si II Si III and Si IV ions. Data taken from the NIST Atomic Spectra Database^a

Ion	Wavelength (Å)	Type	$A_{ul}(s^{-1})$	f_{ul}
Si II	1190.42	Resonant	6.53×10^8	0.277
Si II	1193.28	Resonant	2.69×10^9	0.575
Si II	1194.50	Fluorescent	3.45×10^9	0.737
Si II	1197.39	Fluorescent	1.40×10^9	0.150
Si II	1260.42	Resonant	2.57×10^9	1.22
Si II	1265.02	Fluorescent	4.73×10^8	0.113
Si III	1206.50	Resonant	2.55×10^9	1.67
Si IV	1393.76	Resonant	8.80×10^8	0.513
Si IV	1402.77	Resonant	8.63×10^8	0.255

^a <http://www.nist.gov/pml/data/asd.cfm>

column densities, and the mass outflow rates for each galaxy. However, there are some limitations of this approach: absorption and emission features are modeled independently of each other, there is no way to account for a non-spherical outflow, and limits the number of parameters that could be extrapolated in contrast to an semi-analytical technique. On the other hand, radiation transfer modeling has the potential to provide tighter constraints on a wider range of parameters.

In this paper, we perform semi-analytical radiation transfer modeling of the starburst radiation passing through the outflows of the CLASSY galaxies, modeling the geometry and kinematics of the scattering gas using the Semi Analytical Radiative Transfer (SALT) model of Carr et al. (2022). We target the ultraviolet silicon resonant lines that trace cool and warm gas within outflows, and the resulting galactic properties and mass outflow rates that follow from the modeling of these lines.

This paper is structured as follows: In section 2, we discuss the CLASSY data and its importance. In section 3, we review the SALT model. In section 4, we discuss the fitting procedure and parameter estimates of SALT. The results of this analysis are discussed in section 5. A discussion of the mass outflow rates and their consequences follows in section 6. Comparisons to previous literature are included in section 7. Our conclusions are outlined in section 8.

This paper assumes standard cosmology ($H_0 = 70\text{km s}^{-1}\text{Mpc}^{-1}$, $\Omega_m = 0.3$, and $\Omega_\Lambda = 0.7$).

2. CLASSY

The COS Legacy Archive Spectroscopy Survey (CLASSY) provides high-resolution far-ultraviolet (FUV) Hubble Space Telescope observations of 45 nearby galaxies (Berg et al. 2022). This sample completes the FUV wavelength range in the observed frame between roughly 1200Å and 2000Å. This range includes

the silicon resonant absorption lines of Si II (1190.42Å, 1193.28Å, and 1260.42Å), Si III (1206.50Å), and Si IV (1393.76Å and 1402.77Å). It is these lines of silicon that we will use to analyze the properties of the galactic outflows in their host galaxies. Silicon II and III are good tracers of gas at around $T = 10^4\text{K}$, whereas silicon IV is a tracer of warmer gas of about 10^5K (see Tumlinson et al. 2017). Si II is of particular interest, as this line is believed to trace neutral hydrogen gas (e.g. Shapley et al. 2003).

Observations within CLASSY were taken with the Cosmic Origins Spectrograph (COS) on the Hubble Space Telescope. In order to determine the star-forming region of each galaxy, R_{SF} , we use the NUV half-light radii (r_{50}) as defined and calculated in Xu et al. 2022 (The radius of the galaxy within which half the photons in the COS image are contained). However, for some of the CLASSY galaxies, the photon counts do not flatten at large radii, as a result of being close to or larger than the size of the COS aperture. In these cases ($r_{50} > 0.35''$), SDSS u-band sizes are adopted instead (as in Xu et al. 2022).

As discussed in Carr et al. (2021), due to the aperture size of an observing instrument, SALT needs to account for spectral information that lies beyond a projected radius, R_{AP} , for which the corresponding velocity field is v_{AP} . COS has an aperture diameter of $2.5''$, and therefore we would take the radius of the aperture of the observing instrument, R_{AP} , to be the projected COS aperture radius on each galaxy, i.e. the physical distance of $1.25''$ at the red-shift of that galaxy in kPc . However, we modify this size for this study: The COS throughput in the NUV drops below 80% roughly at the offset of 0.7 arcseconds from the center, which we take to be R_{AP} for this study. It turns out this adjustment fits the data better (further commented on in Section 4).

In order to determine if the spectra of the 45 galaxies were viable for analysis, we first visually inspected the wavelength ranges of interest. In some cases, there was no coverage in the region of interest; in this case, the line is not modeled (although other lines from that same galaxy may still be modeled). The spectrum is also not modeled if there is too much noise in the region of interest. For example, the proximity of the Si III line to the geocoronal $Ly\alpha$ line of the milky way, occasionally results in no observable P-Cygni profile at 1206.50Å. As a result, seven galaxies are not modeled at the Si II 1190.42/1193.28Å wavelength range, thirteen galaxies at the Si II 1260.42Å wavelength range, and fifteen galaxies at the Si III 1206.50Å wavelength range were not analyzed.

In the event that a part of the wavelength range has to be thrown out due lack of data or noise (such as a galaxy's 1260.42Å being unusable, but the 1190.42/1193.28Å is usable or the 1393.76Å line is usable but the 1402.77Å line is not), only the usable portion of the spectrum is fit with SALT. Galaxies with only partial fits are indicated in the Table ? and sample plots in the Appendix.

We normalize the spectra to the stellar continuum (see Xu et al. 2022). If the presence of the Milky Way's Lyman α line resulted in a poor normalization of the absorption lines of interest, we manually renormalized the spectra to the surrounding continuum.

3. SALT MODELING

The Semi-Analytical Line Transfer (SALT) Model, as outlined in Scarlata & Panagia (2015), provides a case for the modeling of absorption and emission lines of spherical galactic outflows. This technique of developing a model for the observed spectra of galaxies has been used and adapted in Carr et al. (2018) and again in Carr et al. (2022), and has been used in the study of the properties of outflows in green pea galaxies (low mass, low metalicity, high star formation galaxies - see Carr et al. (2021)).

The SALT model pictures a spherical galaxy with an associated outflow that behaves as a series of concentric, expanding shells (Scarlata and Panagia (2015)). Photons from the galaxy are emitted uniformly in all directions, which then pass through the outflow, leading to elementally associated absorption and emission of said photons. The advantage of using the SALT model for analyzing P-Cygni profiles is that it consistently computes the absorption and re-emission, thus automatically accounting for emission infilling. Carr et al. (2018) included the modification of the geometry of the outflow to allow for biconically-shaped outflows.

SALT models the outflows with the following parameters; assuming that the velocity and density fields are power-laws (as in Carr et al. 2018, 2021):

- α , the opening angle of the bicone.
- ψ , the orientation angle of the bicone.
- γ , the wind velocity gradient of the gas.
- δ , the density gradient of the gas.
- τ_0 , the optical depth of the gas.
- f_c , the covering fraction of the outflow gas.
- k , the dust opacity.

- v_0 , the launch velocity of the gas in the outflow (the velocity at R_{SF}).
- v_w , the terminal velocity of the gas in the outflow (the velocity at R_w).
- v_{AP} , the velocity at the maximum radius observed withing the aperture of the observing instrument.

As in Carr et al. (2021), we constrain the aperture velocity:

$$v_{AP} = v_0 \left(\frac{R_{AP}}{R_{50}} \right)^\gamma. \quad (1)$$

We also constrain the dust opacity, k , using the measured color excess and assuming a Calzetti extinction law to compute A_{UV} . We convert A_{UV} to the dust optical depth with $A_{UV} \approx 1.086\tau_{UV}$. The dust optical depth and the dust opacity in the code are related by

$$\tau_d = \begin{cases} \frac{k}{\gamma} \ln\left(\frac{v_w}{v_0}\right) & \text{if } \delta = 1 \\ \frac{k}{1-\delta} \left[\left(\frac{v_w}{v_0}\right)^{(1-\delta)/\gamma} - 1 \right] & \text{otherwise.} \end{cases} \quad (2)$$

We extend SALT modeling to also include an absorption component at systematic velocity, which we use to describe absorption in the interstellar medium (ISM) of the galaxy. The presence of an interstellar medium component requires the addition of two additional parameters. We assume that any ISM absorption or emission component takes the form of a Gaussian (Xu et al. 2022, Carr et al. 2022 etc.).

- a , the height/depth of the Gaussian profile.
- σ , the width of the profile.

The ISM component is accounted for in the intrinsic profile, prior to any radiation transfer modeling with SALT. Furthermore, with a detectable ISM absorption component comes the possibility of a detectable ISM emission component (Carr et al. 2022). Thus in total, 8 free parameters are required to be fit with SALT; with the possible of 2 more free parameters for lines hosting a significant ISM component (a and σ).

In this study, we also considered models of a spherical SALT model (in which $\alpha = 90^\circ$, ϕ is irrelevant), with a modification of the wind covering fraction that allows for a power law over radius: $f_c = a_1 y^{-b_1}$. However, spherical SALT fits with this covering fraction resulted in b_1 values at a very small scale (ranging from 10^{-2} to 10^0). This small value close to 0 led us to the conclusion that f_c tends to be constant with radius, and thus as the spherical model is within the bicone model space, the bicone model is generally a more advantageous model, to allow for different geometry of outflows,

Table 2: Milky Way Lines Considered While Masking

Ion	Wavelength (\AA)
H I	1215.67
C I	1277.21
C II	1334.53, 1335.71
N I	1199.55, 1200.22, 1200.71
N V	1235.81, 1242.80
O I	1302.17
Si II	1190.42, 1193.28, 1260.42, 1304.37
Si III	1206.50
Si IV	1393.76, 1402.77
S II	1250.59, 1253.81, 1259.52

in addition to the purely spherical one. The biconical model does contain two additional parameter relative to the spherical one, but repeated AIC and BIC comparisons between the spherical and biconical models fitted to CLASSY lines showed little evidence to suggest that the spherical model was more favorable to the biconical one in the vast majority of tests.

The relevant resonant and fluorescent absorption and emission wavelengths that are analyzed are included in Table 1. The Si II 1190.42, 1193.28, and 1260.42 \AA lines are all modeled together (where possible), where all SALT parameters are kept consistent across all three absorption lines, with the exception of the ISM parameters (a and σ , because we do not perform any radiation transfer modeling in the ISM). Likewise, for the Si IV 1393.76 \AA and 1402.77 \AA lines, SALT models these two lines together (as was done in Carr et al. 2021), again with all the parameters kept the same except for the ISM parameters.

SALT assumes that the aperture of the observing instrument, in this case the COS onboard the Hubble Space Telescope, is larger than the star-forming region of the target galaxy. Therefore, any galaxies with a COS radius larger than R_{50} is not necessarily properly fitted with SALT. We still present the SALT fits of the lines in these galaxies, but we omit them from the subsequent analysis of mass outflow rates, when applicable (see Section 6). These galaxies are J0144+0453, J0337-0502, J0405-3648, J0934+5514, J0940+2935, J0944-0038, J1016+3754, J1105+4444, J1119+5130, J1132+5722, J1148+2546, J1150+1501, J1157+3220, J1225+6109, and J1444+4237.

We also mask Milky Way absorption lines that contaminate the spectra of our CLASSY galaxies. These lines appear in the rest frame of the Milky Way, and thus have no red-shift from their resonant lines. Relevant masking regions are included in table 2.

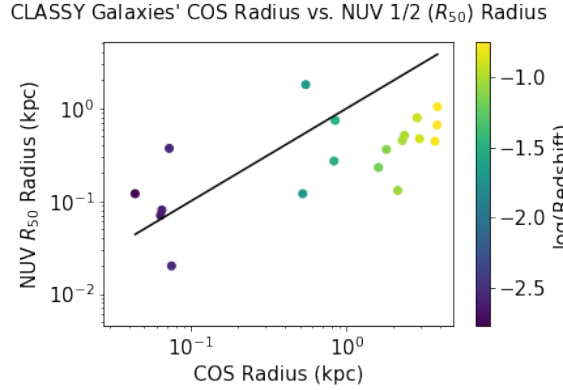


Figure 1: Size comparison between half-light radius (R_{50}) and the radius of the galaxy observed with the COS aperture. Galaxies above the black, one-to-one line are omitted from the SALT analysis, as SALT requires the star-forming region to be within the aperture of the observing instrument.

Masking is used during the fitting process, but any wavelength ranges with sufficiently overlapping outflow features and masks are also excluded from the fitting process, as it becomes too difficult to distinguish the two. As a result of masking, an additional 22 Si II 1190.42/1193.28 \AA , 2 Si II 1260.42 \AA , and 3 Si IV 1393.76/1402.77 \AA wavelength ranges were not fit with SALT.

Upon inspection of the spectra in galaxy J1416+1223, the absorption lines for the relevant Si II, III, and IV ions were noted to be asymmetric and containing a significant red-shifted component, more indicative of a galactic inflow than an outflow (Rubin 2017, Carr et al. 2022). Therefore, we do not fit SALT to this galaxy. Three galaxies that were not fit for any absorption line of silicon are J0808+3948, J1044+0353, and J1323-0132; (the explanation for this is included alongside their spectra in the Appendix).

For the galaxies that had SALT fits in all three ionization states of silicon, the galaxies' size distributions can be seen in Figure 1. It is these galaxies that we will conduct the full mass outflow rate calculation in Section 6. The five galaxies above this line are J0405-3648, J0934+5514, J0940+2935, J1105+4444, and J1150+1501 (the HST/COS and SDSS r-band images of these galaxies can be found in Berg et al. 2022). Unfortunately, the consequence of this omission means a large population of the lower mass galaxies are omitted from our mass outflow analysis, as many of these large galaxies were at low-redshift and thus by selection were low mass galaxies.

4. SALT PARAMETER ESTIMATES

Table 3: Free Parameter Fitting Ranges

Parameter	Range
v_0 (km s $^{-1}$)	[2.0,150.0]
v_w (km s $^{-1}$)	[200.0,1300.0]
γ	[0.5,2.0]
τ_0	[0.01,100.0]
f_c	[0.0,1.0]
α ($^{\circ}$)	[0.0,90.0]
ψ ($^{\circ}$)	[0.0,90.0]
a	[0.0,1.0]
σ (km s $^{-1}$)	[0.0,500.0]

Through the use of the `emcee` Markov Chain Monte-Carlo sampler, the SALT code fits the outflow parameters to the masked normalized spectrum of the galaxy (Foreman-Mackey et al. 2013) using a maximum likelihood estimation (Ivezić et al. 2014).

The ranges allowed for the free parameters in the fitting process can be found in Table ?.

Parameter δ is a special case: The mass outflow rate should not deviate substantially from the constant mass outflow rate that would predict a value of $\delta = \gamma + 2$ (Carr et al. 2018). Therefore δ is restricted to be within a value of 1.5 from the constant mass outflow rate prediction, i.e. $\gamma + 0.5 \leq \delta \leq \gamma + 3.5$. The τ_0 parameter is sampled logarithmically, so that both small and large scale predictions for this parameter is tested.

During the `emcee` fitting process, after each model is generated, it undergoes a Gaussian smoothing, prior to being tested against the data. As many of the CLASSY galaxies are comparatively large relative to R_{COS} , we adjust the standard deviation of the Gaussian used in the smoothing for each galaxy. The deviation of this Gaussian is chosen as the physical size of the galaxy is determined from the COS arcseconds/Pixel ratio (0.0285) and the grating used to image the CLASSY galaxies (which has a ratio of 9.97mÅ/Pixel for the G130M images and 12.23mÅ/Pixel for the G160M images), which is then divided by the velocity separation of data points in each galactic spectrum. For galaxies with an R_{50} larger than R_{cos} , the angular size of the imaged galaxy is replaced with the angular size of COS (in which $R_{COS} = 0.7$ arcseconds). For these extended galaxies, if a value of 1.25 arcseconds is used instead, the resolution is to large and results in oversmoothing of the model, which creates a poor model fit to the data.

Uncertainties for each parameter are taken to be the median of the deviations of the parameter about the chosen maximum likelihood estimation parameter, from the MCMC chains. Once the fitting is complete, the fit is visually inspected. If the fit deviates from the CLASSY

data to an extent that it appears the shape of the data does not match that of the fit, the fitting process was repeated.

5. RESULTS

Example fits for each of the silicon lines for one of the CLASSY galaxies can be seen in Figure 2. The fits for all galaxies in CLASSY can be found in the Appendix. The best-fit parameters of the outflows derived modeling the Si II, III, and IV lines for each galaxy can be found in Table 4. In addition to the free and constrained parameters, the number density n_0 , the terminal radius R_w , and the column density N of the silicon ionization states was also computed. The relevant calculations are below:

$$n_0 = \frac{mc\tau_0 v_0}{\pi e^2 R_{SF}}. \quad (3)$$

$$R_w = R_{SF} \left(\frac{v_w}{v_0} \right)^{1/\gamma}. \quad (4)$$

$$N = \begin{cases} n_0 R_{SF} \ln(R_w/R_{SF}) & \text{if } \delta = 1 \\ n_0 \frac{R_{SF} - R_w (R_w/R_{SF})^{-\delta}}{\delta - 1.0} & \text{otherwise.} \end{cases} \quad (5)$$

5.1. ISM Model Selection

THIS SECTION NEEDS SOME QUANTITATIVE ANALYSIS: Galaxies can roughly be divided into three categories: (1): Those without a prominent ISM component, (2): Those with a prominent ISM absorption component, and (3): Those with a prominent ISM absorption and a prominent ISM emission component. All lines were fit with all three of these models; the model that best fits the data is chosen as the most appropriate model for that absorption line for that galaxy. For example, if there is no major ISM component, it is inconvenient to add two extra parameters representing the ISM absorption (in fact, if these parameters are included in the modeling of an absorption line with no ISM, `emcee` still tries to add a Gaussian distribution, which actually makes the fit worse). In some cases, we see significant red and blue-shifted absorption around the absorption line, which could be due to turbulent broadening, which at present SALT has no capacity to compute. In this case an ISM absorption component with no ISM emission is the best way to proceed (it is evident in the spectra if no ISM emission is present in these situations).

5.2. Outflow Geometry

This section is not complete yet. Note abundance of spheres, large opening angles Do Si II, III, IV tend to overlap to some extend, but are often independent of each other. See Table 4 and Figure 12.

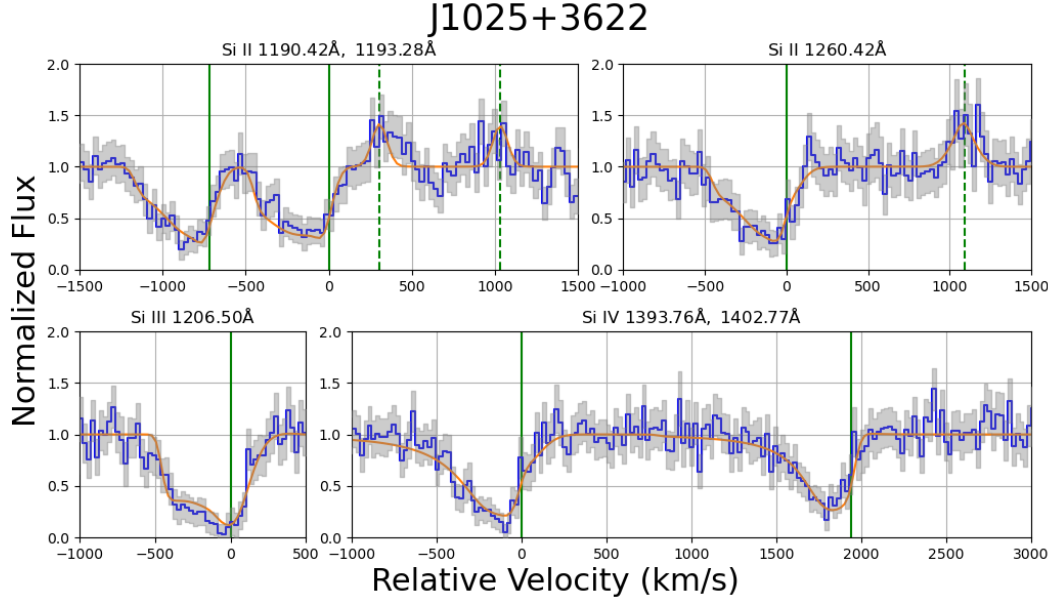


Figure 2: Example SALT fits for CLASSY galaxy J1025+3622.

6. DISCUSSION

We now investigate the derived mass outflow rate of each galaxy, and the related momentum and energy outflow rates. In addition to finding relationships between these fluxes and other galactic properties, we also make predictions on the fundamental physics of these outflows, such as if they are momentum or energy driven processes.

6.1. Mass Outflow Rates

The derived outflow parameters can be used to calculate the mass outflow rate of the corresponding ions of silicon. The mass outflow rate (\dot{M}) is defined as the mass passing through a radius r within the outflow. We use

$$\dot{M}(r) = \Omega f_c m_{Si} n_{0,Si} v_0 R_{SF}^2 \left(\frac{r}{R_{SF}} \right)^{(2+\gamma-\delta)}. \quad (6)$$

where

$$\Omega = 4\pi(1 - \cos(\alpha)). \quad (7)$$

as the definition for the mass outflow rate, where m_{Si} is the mass of the silicon ion. Evidently, the mass outflow rate is dependent on the radius r , corresponding to a specific velocity v within the outflow (Burchett et al. 2021). We choose to present the mass outflow rates as calculated at $r = R_{SF}$, corresponding to $v = v_0$. This is done not only to establish a baseline comparison value between each CLASSY galaxy, but also to remove the dependence of this calculation on the γ and δ SALT parameters. The simulations conducted in Carr et al. (2022), suggests that these two free parameters

in particular do not converge as well as the other SALT parameters.

In order to compute the total mass outflow rate for each galaxy, we must first determine the mass outflow rate for each of the individual ionization states of silicon. We assume that silicon only exists in the three ionization states of Si II, III, and IV (see Chisholm et al. 2018, McKinney 2019 et al.); thus the total silicon mass outflow rate can be determined by summing the three individual components.

One consequence of this is that only galaxies that have successfully been fitted for the Si II, III, and IV lines can be included (i.e. fits must be obtained from all three states).

Given the metallicity of each CLASSY galaxy (referenced from Berg et al. 2022) relative to the solar metallicity and the ratio of hydrogen to silicon in the sun, we scale the silicon mass outflow rate to that of the hydrogen mass outflow rate:

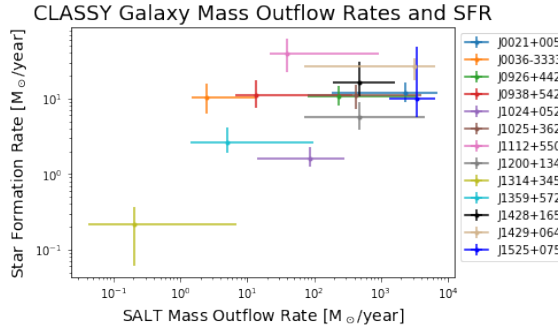
$$\dot{M}_H = \dot{M}_{Si} \frac{Z_{Galaxy}}{Z_\odot} \frac{n_{H,\odot}}{n_{Si,\odot}}. \quad (8)$$

The mass outflow rates for each relevant galaxy can be found in Table 3.

In Figure 3 we show the relationship between the galaxies mass outflow rate, \dot{M} , computed with SALT and the SFR taken from Berg et al. (2022). We confirm the direct correlation between \dot{M} and SFR as found in other surveys of low- and high-redshift galaxies (e.g. Heckman et al. 2015, and supported by the CLASSY analysis in Xu et al. 2022). This relation implies that

Table 4: Main Outflow Rates

Galaxy	$\log(\text{SFR})$ ($M_{\odot} \text{yr}^{-1}$)	$\log(\dot{M})$ ($M_{\odot} \text{yr}^{-1}$)	$\log(\eta)$	$\log(\dot{p})$ (dynes)	$\log(p_*)$ (dynes)	$\log(\eta_p)$	$\log(\dot{E})$ (erg/s)	$\log(E_*)$ (erg/s)	$\log(\eta_E)$
J0021+0052	$1.07^{+0.14}_{-0.11}$	$3.37^{+0.48}_{-1.1}$	$2.3^{+0.48}_{-1.1}$	$36.31^{+0.48}_{-1.17}$	$34.37^{+0.14}_{-0.11}$	$1.94^{+0.49}_{-1.38}$	$43.16^{+0.49}_{-1.23}$	$42.56^{+0.14}_{-0.11}$	$0.61^{+0.5}_{-1.48}$
J0036-3333	$1.01^{+0.19}_{-0.21}$	$0.39^{+0.74}_{-0.22}$	$-0.62^{+0.74}_{-0.22}$	$32.34^{+1.09}_{-0.18}$	$34.31^{+0.19}_{-0.21}$	$-1.97^{+1.09}_{-0.31}$	$38.23^{+1.55}_{-0.18}$	$42.5^{+0.19}_{-0.21}$	$-4.25^{+1.55}_{-0.31}$
J0926+4427	$1.03^{+0.13}_{-0.13}$	$2.37^{+1.17}_{-0.47}$	$1.34^{+1.17}_{-0.47}$	$34.93^{+1.36}_{-0.45}$	$34.33^{+0.13}_{-0.13}$	$0.6^{+1.36}_{-0.51}$	$41.47^{+1.5}_{-0.37}$	$42.52^{+0.13}_{-0.13}$	$-1.03^{+1.5}_{-0.43}$
J0938+5428	$1.05^{+0.2}_{-0.17}$	$1.13^{+1.44}_{-0.3}$	$-0.1^{+1.6}_{-0.37}$	$33.56^{+1.84}_{-0.46}$	$34.35^{+0.2}_{-0.17}$	$-0.79^{+1.84}_{-0.57}$	$40.1^{+2.1}_{-0.57}$	$42.54^{+0.2}_{-0.17}$	$-2.43^{+2.1}_{-0.7}$
J1024+0524	$0.21^{+0.14}_{-0.12}$	$1.94^{+0.51}_{-0.78}$	$1.73^{+0.51}_{-0.78}$	$34.21^{+0.71}_{-0.83}$	$33.51^{+0.14}_{-0.12}$	$0.69^{+0.71}_{-0.95}$	$40.38^{+0.92}_{-0.93}$	$41.7^{+0.14}_{-0.12}$	$-1.31^{+0.92}_{-1.08}$
J1025+3622	$1.04^{+0.14}_{-0.18}$	$2.62^{+0.99}_{-0.72}$	$1.56^{+0.87}_{-0.82}$	$35.11^{+1.16}_{-0.73}$	$34.34^{+0.14}_{-0.18}$	$0.76^{+1.16}_{-0.93}$	$41.49^{+1.36}_{-0.73}$	$42.53^{+0.14}_{-0.18}$	$-1.02^{+1.36}_{-0.93}$
J1112+5503	$1.6^{+0.2}_{-0.25}$	$1.59^{+1.38}_{-0.25}$	$-0.01^{+1.38}_{-0.25}$	$34.39^{+1.04}_{-0.3}$	$34.9^{+0.2}_{-0.25}$	$-0.51^{+1.04}_{-0.47}$	$41.12^{+0.85}_{-0.36}$	$43.09^{+0.2}_{-0.25}$	$-1.95^{+0.85}_{-0.54}$
J1200+1343	$0.75^{+0.2}_{-0.16}$	$2.69^{+0.97}_{-0.84}$	$1.48^{+0.96}_{-0.77}$	$35.17^{+1.07}_{-0.98}$	$34.05^{+0.2}_{-0.16}$	$1.11^{+1.07}_{-1.28}$	$41.55^{+1.22}_{-1.05}$	$42.24^{+0.2}_{-0.16}$	$-0.68^{+1.22}_{-1.42}$
J1314+3452	$-0.67^{+0.23}_{-0.55}$	$-0.69^{+1.54}_{-0.69}$	$-0.02^{+1.54}_{-0.69}$	$30.43^{+3.1}_{-0.67}$	$32.63^{+0.23}_{-0.55}$	$-2.2^{+3.1}_{-nan}$	$35.45^{+4.65}_{-0.67}$	$40.82^{+0.23}_{-0.55}$	$-5.36^{+4.65}_{-nan}$
J1359+5726	$0.42^{+0.2}_{-0.14}$	$0.7^{+1.3}_{-0.55}$	$0.28^{+1.32}_{-0.55}$	$32.53^{+2.09}_{-0.53}$	$33.72^{+0.2}_{-0.14}$	$-1.19^{+2.09}_{-0.61}$	$38.36^{+2.95}_{-0.36}$	$41.91^{+0.2}_{-0.14}$	$-3.53^{+2.95}_{-0.43}$
J1428+1653	$1.22^{+0.26}_{-0.19}$	$2.68^{+0.54}_{-0.39}$	$1.55^{+0.6}_{-0.38}$	$34.84^{+0.78}_{-0.45}$	$34.52^{+0.26}_{-0.19}$	$0.32^{+0.78}_{-0.58}$	$41.06^{+0.98}_{-0.6}$	$42.71^{+0.26}_{-0.19}$	$-1.63^{+0.98}_{-0.76}$
J1429+0643	$1.42^{+0.11}_{-0.17}$	$3.5^{+0.31}_{-1.65}$	$2.08^{+0.31}_{-1.66}$	$36.17^{+0.46}_{-1.66}$	$34.72^{+0.11}_{-0.17}$	$1.45^{+0.46}_{-nan}$	$42.73^{+0.6}_{-1.65}$	$42.91^{+0.11}_{-0.17}$	$-0.17^{+0.6}_{-nan}$
J1525+0757	$1.0^{+0.69}_{-0.24}$	$3.53^{+0.28}_{-0.41}$	$2.53^{+0.28}_{-0.41}$	$36.18^{+0.3}_{-0.43}$	$34.3^{+0.69}_{-0.24}$	$1.88^{+0.7}_{-0.62}$	$42.73^{+0.33}_{-0.44}$	$42.49^{+0.69}_{-0.24}$	$0.25^{+0.7}_{-0.64}$

**Figure 3:** The predicted mass outflow rate as a function of the star-formation rate for the CLASSY galaxies.

galaxies with higher rates of SF tend to eject more material into the circumgalactic medium.

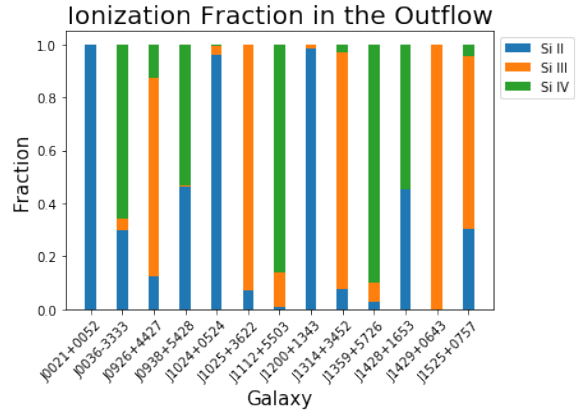
6.1.1. Outflow Silicon Ionization Distribution

As the total mass outflow rate of silicon is dependent upon the outflow rates of the individual ionization states, we can determine what proportion of the mass outflow results from which ionization state, as predicted by SALT. As seen in Figure 4, SALT does not predict a consistent distribution of ionization states, in contrast to the assumption of CLOUDY modeling.

6.2. Mass loading Factor

As star formation results in the deposition of momentum and energy into the interstellar medium surrounding the star-forming regions, star-formation can be used to normalize the mass outflow rates (e.g., Chisholm et al. 2017). This normalized value is defined as $\eta = \dot{M}/\text{SFR}$, the mass loading factor.

Previously, papers have noted the inverse relation between η and the stellar mass and SFR of galaxies (Heck-

**Figure 4:** The distribution of the mass outflow rate for each galaxy that arises from each ionization state of silicon.

man et al. 2015, Xu et al. 2022). This inverse relation is also expected theoretically (see, e.g., XXX). In Figure 5 we show the mass loading factor as a function of the galaxies’ stellar mass (left panel) and SFR (right panel). Our results do not support the existence of strong correlations between η and either the stellar mass or the galaxies’ SFR. Compared with the theoretical expectations established in previous studies (Hayward & Hopkins 2017 and Pandya et al. 2021), we find that the range of mass loading factors for the CLASSY galaxies computed using the best-fit SALT parameters tend to be systematically higher than models, although both the scatter among measurements and the uncertainties on the individual measurements are large.

6.3. Momentum and Energy Outflow Rates

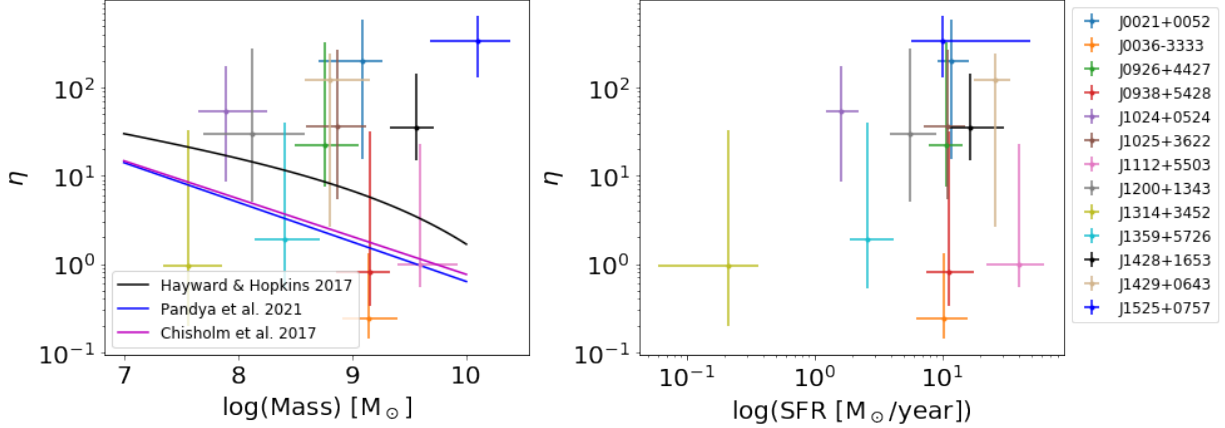


Figure 5: Left: The mass outflow factor and the total galactic mass. A few models established in previous works are included as a reference. Right: The mass outflow factor and star-formation rate.

We now have the ability to estimate the momentum and energy outflow rates for the CLASSY galaxies. The momentum outflow rate (the momentum flux carried through the outflow) is given by $\dot{p} = \dot{M}v_o$ whereas the energy outflow rate (the kinetic energy flux carried through the outflow) is given by $\dot{E} = \frac{1}{2}\dot{M}v_0^2$ (Chisholm et al. 2017). We choose v_0 since \dot{M} is computed at R_{SF} . The momentum and energy outflow rates are computed individually for each ionization state of silicon, and then summed together to get the total outflow rates of silicon. We scale the silicon outflow rates to hydrogen as we did for the mass outflow rate.

We compute the \dot{p} and \dot{E} values at $R_{SF} = R_{50}$, for the same reasons mentioned in the discussion of the mass outflow rates.

It is interesting to see how the momentum and energy outflow rates correlate with the momentum and kinetic energy flux deposited by the starburst. To compute the latter, we use the relations between \dot{p} and \dot{E} and the galaxies SFRs presented in Murray et al. (2005) and Leitherer et al. (1999), where the momentum and energy deposition rates from supernovae are given by $\dot{p}_{SF} = 2 \times 10^{33} \left(\frac{\text{SFR}}{1 \text{M}_\odot \text{yr}^{-1}} \right)$ dynes and $\dot{E}_{SF} = 3 \times 10^{41} \left(\frac{\text{SFR}}{1 \text{M}_\odot \text{yr}^{-1}} \right)$ erg/s. These relations only include direct energy and momentum deposition from supernovae, and would change with the inclusion of other factors such as stellar winds. Comparisons between \dot{p} and \dot{E} with their predicted counterparts can be seen in Figure 6 and 7.

The momentum deposition rate provided by the starbursts observed in the CLASSY galaxies is consistent with the observed momentum outflow rate. On the other hand, the energy deposition rate is about an order of magnitude higher than the estimated energy outflow rates, suggesting that while momentum is transferred

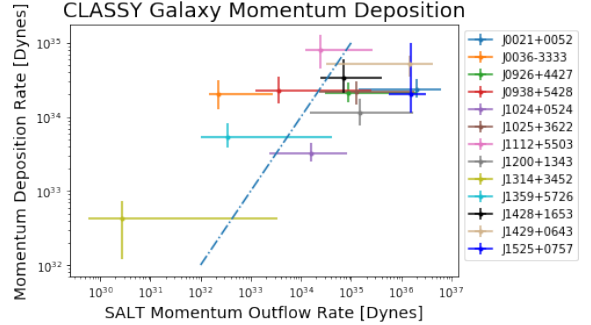


Figure 6: Estimated momentum outflow rates vs. the direct momentum deposition rate from supernovae as derived from star-formation rates. The positive correlation between the results and the fact that most galaxies lie within an order of magnitude off the one-to-one line implies an efficient transfer of momentum in these CLASSY galaxies.

fairly efficiently, energy is not, and the outflows in these CLASSY galaxies are momentum driven rather than energy driven.

In Figures 8 we show the dependency of the momentum loading factors (η_p , left) and energy loading factors (η_E , right) with galaxy stellar mass. In these figures we also show the predictions from the FIRE-2 hydrodynamical simulations of Pandya et al. (2021).

We find that the momentum loading factor does not depend on the galaxy stellar mass, at odd with the results of simulations that would predict an inverse correlation between η_p and $\text{Log}(M)$. Even though the predicted correlation is weak, our observed values are nevertheless systematically higher than the predicted values (by up to an order of magnitude). We find an even stronger discrepancy between the observed energy loading factor and the predicted trend. While simulations do again predict an inverse correlation between η_E and

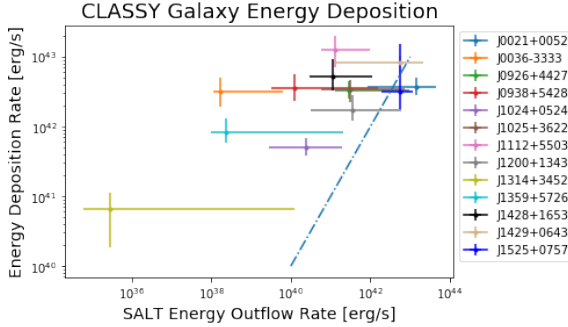


Figure 7: Estimated energy outflow rates vs. the direct energy deposition rate from supernovae as derived from star-formation rates. There does exist a positive correlation between the results, implying that as SFR increases, so does the energy outflow rate (which is logical from the mass outflow rate/star-formation rate association). However, the fact that most galaxies lie over two orders of magnitude off the one-to-one line implies there does not exist an efficient transfer of energy in most of these CLASSY galaxies. The two prominent exceptions are J0021+0052 and J1525+0757.

$\text{Log}(M)$, we do see a positive correlation between these two quantities. One possible explanation for these discrepancies is that Pandya et al. (2021) found that the energy loading factor is much more heavily influenced by hot gases (of the order $10^5 K$ and above) than by the warm gases (of order $10^3 - 10^5 K$), of which the Si II, III, and IV are tracers (Tumlinson et al. 2017). In contrast, Pandya et al. (2021) found that for the mass and momentum loading factors, the warm and hot gases contribute by a similar amount. Therefore our energy loading factor may be underestimated to a large extent, as it does not consider hotter gases in its computation of the hydrogen energy outflow rate.

7. COMPARISON TO XU ET AL. (2022)

Here we compare our results to those presented in Xu et al. (2022). Xu et al. perform a Gaussian fit to the absorption and emission lines observed in the COS spectra and derive the mass outflow rates from the best fit velocity centroids. In contrast to the assumption made in this paper, Xu et al. (2022) assumed the outflow velocity is constant (i.e. $\gamma = 0$), $\delta = 2$, $R_{SF} = 2 \times R_{50}$, and that the outflows are spherical. In addition, Xu et al. only considers Si II absorption lines and uses CLOUDY to compute the silicon ionization state and go from the column density of Si II to total silicon column density.

We now show the comparison between SALT and Xu's outflows properties. Specifically, we compare the mass outflow rates in Figure 9, the momentum outflow rates in Figure 10 and the Energy outflow rates in Figure 11. In

Figure 9, we see that for the two galaxies with the lowest mass outflow rates, the two analysis agree. At larger values, however, SALT results are systematically higher than those based on a Gaussian analysis. Similar trends are seen in Figure 10 and 11. While the magnitudes of the reported values differ, we do find that Xu's and SALT's parameters are positively correlated. Thus the two analysis will likely capture the same trends when compared with other galactic properties.

Even though the uncertainties in the SALT estimates are large, the difference between the two analyses are significant. This result suggests that in reality the empirical knowledge of mass outflow rates in galaxies is limited by the analysis rather than the quality of the data. In other words, we are unlikely to improve on the model discrepancies with either deeper or higher resolution data. Therefore systematic uncertainties set the limit on what we can learn from absorption line studies. What is needed to move forward is a comparison of the performance of these two analysis on synthetic spectra created from simulations.

8. CONCLUSION

In this work, we have conducted a semi-analytical line transfer analysis upon the ultraviolet P-Cygni profiles on the local, star-forming CLASSY galaxies. From these results, we estimated these galaxies mass, momentum, and energy outflow rates.

Our primary conclusions are as follows:

- The average opening angle has a value of (INSERT AMOUNT HERE), which suggests that most outflows have large opening angles.
- The semi-analytical methods presented in this paper reveal similar trends to the Gaussian fitting techniques used in Xu et al. 2022 to analyze outflows; that said, the magnitude of these values vary.
- The mass outflow rates vary directly with star-formation rates, but there exists much scatter within these results.
- These galaxies exhibit momentum-driven behavior in their outflows rather than energy-driven.

The spread of results may indicate there is large uncertainty within these results, and while this may be true, it could also be noted as signifying the complexity and diversity amongst different galactic systems. In further work, these semi-analytical methods can be used in future for work on lines that trace hotter gas, like Carbon IV.

Mention surveys here

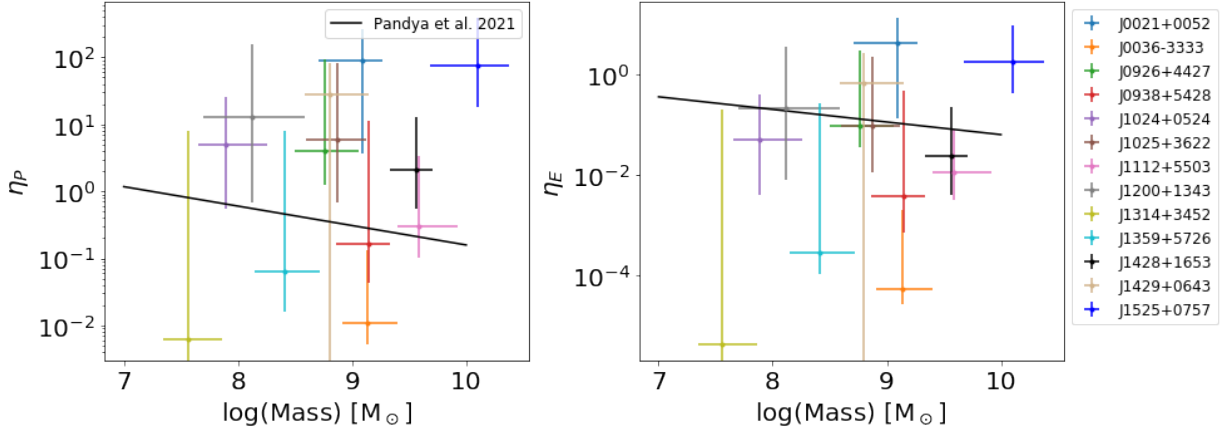


Figure 8: CHECK ERROR BARS Left: Momentum loading factor vs. galactic mass. Right: Energy loading factor vs. galactic mass. Both plots include a black line as predicted from the Fire-2 simulations (Pandya et al. 2021). Our predicted momentum loading factor tends to agree within two orders of magnitude with the Fire-2 simulations, but the difference between our predictions and the Fire-2 predictions for the energy loading factor is generally several orders of magnitude.

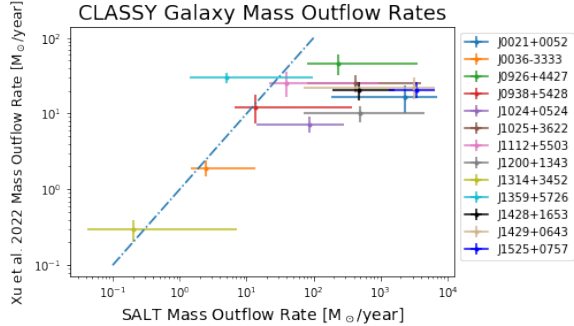


Figure 9: Comparison between the CLASSY galaxies mass outflow rates computed in Xu et al. 2022 with the outflow rates we computed given the SALT analysis. The blue line gives the one-to-one line between the two variables. While there exists a positive correlation between the two results, the magnitudes of our values tend to be larger.

9. ACKNOWLEDGEMENT

We would like to acknowledge and thank the CLASSY team for their input and feedback, as well as providing the stellar continuum fits used for normalization. Supported for this research was provided by the University of Minnesota Undergraduate Research Opportunities Program Grant (UROP).

APPENDIX

- A. OUTFLOW GEOMETRY PLOTS
- B. SALT PARAMETER RESULTS
- C. SALT FITS

Table 5: Parameter Values

Name	Ion	$\alpha(^{\circ})$	$\psi(^{\circ})$	γ	δ	$\log(\tau)$	f_c	$\log(k)$	$v_0(km/s)$	$v_w(km/s)$	$v_{ap}(km/s)$	$\log(n_0)$	RSF	RW	N
J0021+0052	Si II	58 ₋₁₇ ⁺¹⁷	65 ₋₂₈ ⁺¹¹	0.8 _{-0.1} ^{+0.6}	2.4 _{-0.4} ^{+1.3}	2.0 _{-2.1} ^{+0.5}	0.78 _{-0.41} ^{+0.1}	fix_{-fix}^{+fix}	109 ₋₄₀ ⁺²⁰	66 ₋₂₀₂ ⁺²⁶⁰	411 ₋₁₃₃ ⁺⁷⁴²	0.0 _{-0.0} ^{+0.0}	0.0 _{-0.0} ^{+0.0}	0.0 _{-0.0} ^{+0.0}	0.0 _{-0.0} ^{+0.0}
	Si III	49 ₋₁₃ ⁺¹⁹	33 ₋₁₉ ⁺¹⁵	0.5 _{-0.0} ^{+0.5}	1.4 _{-0.2} ^{+1.0}	0.3 _{-0.7} ^{+1.1}	0.7 _{-0.05} ^{+0.05}	fix_{-fix}^{+fix}	3 ₋₁ ⁺⁸	766 ₋₄₄ ⁺¹²⁸	7 ₋₁ ⁺⁶²	0.0 _{-0.0} ^{+0.0}			
	Si IV	84 ₋₂₇ ⁺³	62 ₋₃₆ ⁺¹²	0.8 _{-0.2} ^{+0.5}	1.4 _{-0.2} ^{+0.7}	-0.8 _{-0.5} ^{+1.1}	0.62 _{-0.04} ^{+0.04}	fix_{-fix}^{+fix}	20 ₋₁₀ ⁺⁸	929 ₋₂₆ ⁺⁸⁹	78 ₋₃₇ ⁺¹¹⁷	0.0 _{-0.0} ^{+0.0}			
J0036-3333	Si II	36 ₋₇ ⁺¹²	9 ₋₄ ⁺¹⁶	0.5 _{-0.0} ^{+0.4}	2.4 _{-0.2} ^{+1.0}	1.9 _{-1.0} ^{+0.4}	0.55 _{-0.02} ^{+0.03}	fix_{-fix}^{+fix}	12 ₋₃ ⁺¹³	580 ₋₇₈ ⁺³⁵⁶	26 ₋₆ ⁺⁸⁴	0.0 _{-0.0} ^{+0.0}	0.0 _{-0.0} ^{+0.0}	0.0 _{-0.0} ^{+0.0}	0.0 _{-0.0} ^{+0.0}
	Si III	56 ₋₁₆ ⁺¹⁶	50 ₋₁₀ ⁺¹⁰	0.7 _{-0.1} ^{+0.4}	1.9 _{-0.2} ^{+0.6}	0.8 _{-0.4} ^{+0.7}	0.95 _{-0.04} ^{+0.02}	fix_{-fix}^{+fix}	6 ₋₂ ⁺⁷	583 ₋₂₇ ⁺³⁸	17 ₋₆ ⁺²⁵	0.0 _{-0.0} ^{+0.0}			
	Si IV	54 ₋₁₁ ⁺⁸	6 ₋₃ ⁺⁹	1.8 _{-0.4} ^{+0.4}	4.2 _{-0.9} ^{+0.2}	1.4 _{-0.6} ^{+0.4}	0.9 _{-0.07} ^{+0.05}	fix_{-fix}^{+fix}	12 ₋₂ ⁺⁵	1203 ₋₂₂₁ ⁺²⁰	211 ₋₉₃ ⁺⁷⁷	0.0 _{-0.0} ^{+0.0}			
J0127-0619	Si II	27 ₋₈ ⁺¹⁹	10 ₋₆ ⁺²¹	0.7 _{-0.1} ^{+0.4}	1.5 _{-0.2} ^{+1.6}	0.1 _{-1.0} ^{+1.4}	0.69 _{-0.15} ^{+0.15}	fix_{-fix}^{+fix}	128 ₋₅₇ ⁺¹²	261 ₋₁₂ ⁺⁷³	502 ₋₂₃₉ ⁺⁹⁹⁷	0.0 _{-0.0} ^{+0.1}	0.0 _{-0.0} ^{+0.0}	0.0 _{-0.0} ^{+0.0}	0.0 _{-0.0} ^{+0.0}
	Si III	-	-	-	-	-	-	-	-	-	-	-			
	Si IV	-	-	-	-	-	-	-	-	-	-	-			
J0144+0453	Si II	7 ₋₄ ⁺²⁹	40 ₋₁₄ ⁺²⁹	1.8 _{-0.6} ^{+0.1}	4.2 _{-1.2} ^{+0.5}	-1.4 _{-0.3} ^{+2.2}	0.56 _{-0.3} ^{+0.22}	fix_{-fix}^{+fix}	19 ₋₉ ⁺⁵⁷	1175 ₋₅₂₉ ⁺⁵⁹	2 ₋₁ ⁺¹⁶	0.0 _{-0.0} ^{+0.0}	0.0 _{-0.0} ^{+0.0}	0.0 _{-0.0} ^{+0.0}	0.0 _{-0.0} ^{+0.0}
	Si III	-	-	-	-	-	-	-	-	-	-	-			
	Si IV	30 ₋₁₁ ⁺³⁶	1 ₋₁ ⁺³⁵	1.0 _{-0.3} ^{+0.4}	3.8 _{-0.9} ^{+0.5}	-0.1 _{-0.7} ^{+1.2}	0.48 _{-0.13} ^{+0.25}	fix_{-fix}^{+fix}	20 ₋₉ ⁺²⁷	298 ₋₇₇ ⁺⁴²⁷	6 ₋₃ ⁺⁹	0.0 _{-0.0} ^{+0.0}			
J0337-0502	Si II	-	-	-	-	-	-	-	-	-	-	-	-	-	-
	Si III	-	-	-	-	-	-	-	-	-	-	-			
	Si IV	-	-	-	-	-	-	-	-	-	-	-			
J0405-3648	Si II	69 ₋₃₀ ⁺¹¹	69 ₋₃₈ ⁺¹⁰	0.9 _{-0.2} ^{+0.6}	3.0 _{-0.7} ^{+0.9}	2.4 _{-2.4} ^{+0.3}	0.48 _{-0.27} ^{+0.2}	fix_{-fix}^{+fix}	48 ₋₂₃ ⁺³⁶	796 ₋₃₇₂ ⁺²¹	9 ₋₆ ⁺⁹	0.0 _{-0.0} ^{+0.0}	0.0 _{-0.0} ^{+0.0}	0.0 _{-0.0} ^{+0.0}	0.0 _{-0.0} ^{+0.0}
	Si III	77 ₋₂₆ ⁺⁷	39 ₋₂₂ ⁺¹⁸	1.1 _{-0.3} ^{+0.4}	3.3 _{-0.7} ^{+0.7}	-0.7 _{-0.8} ^{+1.6}	0.57 _{-0.13} ^{+0.17}	fix_{-fix}^{+fix}	28 ₋₁₁ ⁺¹⁸	209 ₋₁₀ ⁺³⁹⁸	3 ₋₂ ⁺⁵	0.0 _{-0.0} ^{+0.0}			
	Si IV	89 ₋₂₈ ⁺⁰	39 ₋₁₉ ⁺²⁰	1.6 _{-0.5} ^{+0.2}	4.8 _{-1.7} ^{+0.3}	-0.1 _{-1.0} ^{+1.6}	0.35 _{-0.05} ^{+0.21}	fix_{-fix}^{+fix}	42 ₋₁₅ ⁺¹⁵	867 ₋₄₇₀ ⁺¹⁸³	2 ₋₁ ⁺⁵	0.0 _{-0.0} ^{+0.0}			
J0808+3948	Si II	-	-	-	-	-	-	-	-	-	-	-	-	-	-
	Si III	-	-	-	-	-	-	-	-	-	-	-			
	Si IV	-	-	-	-	-	-	-	-	-	-	-			
J0823+2806	Si II	54 ₋₂₄ ⁺²⁴	66 ₋₂₃ ⁺¹⁴	1.7 _{-0.2} ^{+0.2}	2.8 _{-0.4} ^{+1.4}	0.5 _{-0.7} ^{+0.4}	0.83 _{-0.42} ^{+0.08}	fix_{-fix}^{+fix}	92 ₋₂₀ ⁺²⁰	1104 ₋₂₀₇ ⁺⁸³	1162 ₋₃₀₉ ⁺³⁹⁶	0.0 _{-0.0} ^{+0.0}	0.0 _{-0.0} ^{+0.0}	0.0 _{-0.0} ^{+0.0}	0.0 _{-0.0} ^{+0.0}
	Si III	-	-	-	-	-	-	-	-	-	-	-			
	Si IV	40 ₋₂₀ ⁺²⁰	6 ₋₃ ⁺²¹	1.0 _{-0.3} ^{+0.3}	3.5 _{-0.6} ^{+0.5}	1.4 _{-0.5} ^{+0.9}	0.71 _{-0.03} ^{+0.05}	fix_{-fix}^{+fix}	28 ₋₁₀ ⁺⁹	326 ₋₁₀ ⁺³²⁹	121 ₋₄₆ ⁺⁴⁵	0.0 _{-0.0} ^{+0.0}			
J0926+4427	Si II	88 ₋₁₄ ⁺¹	38 ₋₁₈ ⁺²⁶	1.3 _{-0.2} ^{+0.4}	3.4 _{-0.5} ^{+1.4}	0.5 _{-0.7} ^{+0.4}	0.83 _{-0.42} ^{+0.08}	fix_{-fix}^{+fix}	13 ₋₄ ⁺⁶	425 ₋₂₅ ⁺²⁸³	69 ₋₁₈ ⁺⁵²	0.0 _{-0.0} ^{+0.0}	0.0 _{-0.0} ^{+0.0}	0.0 _{-0.0} ^{+0.0}	0.0 _{-0.0} ^{+0.0}
	Si III	58 ₋₁₂ ⁺¹⁵	38 ₋₁₃ ⁺¹⁷	1.9 _{-0.7} ^{+0.7}	3.8 _{-0.9} ^{+0.6}	1.4 _{-1.5} ^{+0.7}	0.79 _{-0.06} ^{+0.09}	fix_{-fix}^{+fix}	55 ₋₁₅ ⁺³²	495 ₋₁₁ ⁺²⁰⁹	1620 ₋₁₀₄₁ ⁺⁶¹¹	0.0 _{-0.0} ^{+0.0}			
	Si IV	72 ₋₂₁ ⁺⁸	4 ₋₂ ⁺²⁹	0.8 _{-0.1} ^{+0.4}	3.6 _{-0.8} ^{+0.6}	-0.1 _{-0.5} ^{+0.9}	0.72 _{-0.07} ^{+0.09}	fix_{-fix}^{+fix}	116 ₋₄₅ ⁺¹⁴	1244 ₋₄₈₄ ⁺²⁹	438 ₋₁₂₉ ⁺³⁴⁵	0.0 _{-0.0} ^{+0.0}			
J0934+5514	Si II	80 ₋₃₁ ⁺⁵	40 ₋₂₀ ⁺²⁰	1.8 _{-0.6} ^{+0.1}	4.0 _{-1.2} ^{+0.5}	1.9 _{-2.1} ^{+0.6}	0.18 _{-0.05} ^{+0.2}	fix_{-fix}^{+fix}	119 ₋₃₄ ⁺¹⁸	232 ₋₂₂ ⁺⁸⁵	47 ₋₁₆ ⁺²⁴	0.0 _{-0.0} ^{+0.0}	0.0 _{-0.0} ^{+0.0}	0.0 _{-0.0} ^{+0.0}	0.0 _{-0.0} ^{+0.0}
	Si III	32 ₋₁₇ ⁺²⁷	84 ₋₃ ⁺³	2.0 _{-0.7} ^{+0.0}	5.1 _{-1.7} ^{+0.1}	-0.6 _{-0.7} ^{+1.8}	0.72 _{-0.13} ^{+0.13}	fix_{-fix}^{+fix}	90 ₋₄₃ ⁺²⁹	508 ₋₂₂₃ ⁺³⁷³	32 ₋₁₅ ⁺²⁶	0.0 _{-0.0} ^{+0.0}			
	Si IV	65 ₋₂₄ ⁺¹¹	39 ₋₂₀ ⁺²⁴	1.8 _{-0.6} ^{+0.1}	2.5 _{-1.3} ^{+1.3}	2.0 _{-2.0} ^{+0.5}	0.19 _{-0.03} ^{+0.44}	fix_{-fix}^{+fix}	49 ₋₁₅ ⁺¹⁴	203 ₋₂₉ ⁺²⁰⁹	19 ₋₁₁ ⁺¹¹	0.0 _{-0.0} ^{+0.0}			
J0938+5428	Si II	70 ₋₁₁ ⁺¹	19 ₋₈ ⁺⁵	0.9 _{-0.2} ^{+0.2}	3.3 _{-0.7} ^{+0.6}	1.5 _{-0.7} ^{+0.8}	0.72 _{-0.02} ^{+0.02}	fix_{-fix}^{+fix}	57 ₋₁₄ ⁺¹⁵	899 ₋₂₅ ⁺¹⁹⁹	313 ₋₈₀ ⁺⁸⁰	0.0 _{-0.0} ^{+0.0}	0.0 _{-0.0} ^{+0.0}	0.0 _{-0.0} ^{+0.0}	0.0 _{-0.0} ^{+0.0}
	Si III	11 ₋₄ ⁺²²	6 ₋₃ ⁺⁸	1.0 _{-0.3} ^{+0.5}	1.6 _{-0.2} ^{+1.6}	0.6 _{-1.6} ^{+1.1}	0.57 _{-0.15} ^{+0.15}	fix_{-fix}^{+fix}	20 ₋₉ ⁺⁸⁴	479 ₋₅₁ ⁺⁹⁹	91 ₋₇₅ ⁺⁷⁵	0.0 _{-0.0} ^{+0.0}			
	Si IV	59 ₋₂₁ ⁺¹³	52 ₋₂₂ ⁺¹³	1.6 _{-0.6} ^{+0.2}	4.8 _{-1.3} ^{+0.2}	-0.2 _{-0.6} ^{+1.0}	0.67 _{-0.18} ^{+0.14}	fix_{-fix}^{+fix}	74 ₋₃₄ ⁺²⁶	1228 ₋₃₀₄ ⁺³⁸	882 ₋₅₉₅ ⁺⁴⁰⁴	0.0 _{-0.0} ^{+0.0}			

Table 6: Parameter Values

Name	Ion	$\alpha(^{\circ})$	$\psi(^{\circ})$	γ	δ	$\log(\tau)$	f_c	$\log(k)$	$v_0(km/s)$	$v_w(km/s)$	$v_{ap}(km/s)$	$\log(n_0)$	RSF	RW	N
J0940+2935	Si II	53^{+19}_{-16}	21^{+25}_{-10}	$0.9^{+0.5}_{-0.2}$	$1.4^{+1.7}_{-0.1}$	$-2.0^{+2.6}_{-0.0}$	$0.48^{+0.18}_{-0.25}$	fix^{+fix}_{-fix}	19^{+42}_{-8}	1282^{+7}_{-698}	6^{+10}_{-3}	$0.0^{+0.0}_{-0.0}$			
	Si III	59^{+17}_{-25}	30^{+24}_{-15}	$0.5^{+0.7}_{-0.0}$	$3.8^{+0.6}_{-0.9}$	$-0.8^{+1.7}_{-0.6}$	$0.66^{+0.18}_{-0.27}$	fix^{+fix}_{-fix}	19^{+40}_{-9}	1063^{+119}_{-557}	9^{+12}_{-6}	$0.0^{+0.0}_{-0.0}$			
	Si IV	15^{+45}_{-5}	11^{+30}_{-5}	$1.9^{+0.0}_{-0.6}$	$5.1^{+0.2}_{-1.9}$	$2.5^{+0.2}_{-2.7}$	$0.21^{+0.33}_{-0.03}$	fix^{+fix}_{-fix}	10^{+27}_{-4}	260^{+362}_{-32}	1^{+6}_{-0}	$0.0^{+0.0}_{-0.0}$			
J0942+3547	Si II	-5672^{+5672}_{-5672}	-5672^{+5672}_{-5672}	$-+-$	$-+-$	$-+-$	$-+-$	fix^{+fix}_{-fix}	$-+-$	$-+-$	$-+-$	$-+-$	$-+-$	$-+-$	
	Si III	36^{+15}_{-15}	5^{+9}_{-3}	$1.8^{+0.1}_{-0.4}$	$3.0^{+1.2}_{-0.5}$	$0.7^{+1.1}_{-2.0}$	$0.64^{+0.18}_{-0.1}$	fix^{+fix}_{-fix}	26^{+31}_{-7}	234^{+272}_{-32}	264^{+224}_{-80}	$0.0^{+0.0}_{-0.0}$			
	Si IV	55^{+14}_{-15}	6^{+23}_{-3}	$1.0^{+0.4}_{-0.3}$	$2.8^{+0.8}_{-0.6}$	$-1.3^{+0.6}_{-0.3}$	$0.64^{+0.09}_{-0.06}$	fix^{+fix}_{-fix}	60^{+10}_{-17}	945^{+213}_{-279}	228^{+197}_{-94}	$0.0^{+0.0}_{-0.0}$			
J0944-0038	Si II	41^{+26}_{-18}	80^{+5}_{-44}	$1.0^{+0.5}_{-0.3}$	$1.7^{+1.6}_{-0.2}$	$1.3^{+0.8}_{-1.8}$	$0.65^{+0.15}_{-0.37}$	fix^{+fix}_{-fix}	98^{+26}_{-50}	560^{+330}_{-190}	8^{+9}_{-5}	$0.0^{+0.0}_{-0.0}$			
	Si III	-5672^{+5672}_{-5672}	-5672^{+5672}_{-5672}	$-+-$	$-+-$	$-+-$	$-+-$	fix^{+fix}_{-fix}	$-+-$	$-+-$	$-+-$	$-+-$	$-+-$	$-+-$	
	Si IV	10^{+46}_{-5}	12^{+37}_{-6}	$0.8^{+0.5}_{-0.2}$	$1.8^{+1.7}_{-0.3}$	$-1.5^{+1.8}_{-0.2}$	$0.68^{+0.16}_{-0.42}$	fix^{+fix}_{-fix}	11^{+47}_{-5}	550^{+331}_{-198}	1^{+6}_{-1}	$0.0^{+0.0}_{-0.0}$			
J0944+3442	Si II	—	—	—	—	—	—	—	—	—	—	—	—	—	
	Si III	—	—	—	—	—	—	—	—	—	—	—	—	—	
	Si IV	—	—	—	—	—	—	—	—	—	—	—	—	—	
J1016+3754	Si II	28^{+20}_{-15}	85^{+2}_{-28}	$0.9^{+0.6}_{-0.2}$	$3.7^{+0.6}_{-1.1}$	$-0.9^{+2.0}_{-0.6}$	$0.54^{+0.23}_{-0.29}$	fix^{+fix}_{-fix}	16^{+62}_{-7}	362^{+460}_{-94}	11^{+38}_{-5}	$0.0^{+0.0}_{-0.0}$			
	Si III	-5672^{+5672}_{-5672}	-5672^{+5672}_{-5672}	$-+-$	$-+-$	$-+-$	$-+-$	fix^{+fix}_{-fix}	$-+-$	$-+-$	$-+-$	$-+-$	$-+-$	$-+-$	
	Si IV	48^{+24}_{-13}	35^{+17}_{-19}	$1.0^{+0.4}_{-0.3}$	$3.3^{+0.8}_{-0.7}$	$-0.2^{+0.8}_{-0.5}$	$0.84^{+0.07}_{-0.11}$	fix^{+fix}_{-fix}	21^{+8}_{-6}	1288^{+6}_{-815}	14^{+5}_{-4}	$0.0^{+0.0}_{-0.0}$			
J1024+0524	Si II	79^{+3}_{-7}	76^{+8}_{-18}	$1.9^{+0.0}_{-0.3}$	$3.2^{+0.8}_{-0.5}$	$-0.5^{+1.5}_{-0.4}$	$0.82^{+0.09}_{-0.14}$	fix^{+fix}_{-fix}	58^{+11}_{-11}	201^{+24}_{-141}	536^{+81}_{-150}	$0.0^{+0.0}_{-0.0}$			
	Si III	77^{+7}_{-26}	8^{+24}_{-4}	$1.4^{+0.2}_{-0.5}$	$4.9^{+0.2}_{-0.7}$	$1.1^{+0.9}_{-1.0}$	$0.8^{+0.06}_{-0.04}$	fix^{+fix}_{-fix}	18^{+9}_{-8}	314^{+67}_{-36}	90^{+32}_{-45}	$0.0^{+0.0}_{-0.0}$			
	Si IV	86^{+2}_{-28}	56^{+10}_{-32}	$1.4^{+0.3}_{-0.4}$	$3.9^{+0.5}_{-0.5}$	$-0.3^{+1.3}_{-0.5}$	$0.85^{+0.07}_{-0.12}$	fix^{+fix}_{-fix}	30^{+12}_{-15}	580^{+251}_{-180}	151^{+71}_{-82}	$0.0^{+0.0}_{-0.0}$			
J1025+3622	Si II	60^{+14}_{-19}	35^{+15}_{-18}	$0.5^{+0.4}_{-0.0}$	$3.0^{+0.8}_{-0.9}$	$2.2^{+0.4}_{-1.1}$	$0.85^{+0.03}_{-0.03}$	fix^{+fix}_{-fix}	39^{+14}_{-19}	644^{+95}_{-135}	71^{+47}_{-28}	$0.0^{+0.0}_{-0.0}$			
	Si III	85^{+2}_{-27}	70^{+7}_{-45}	$1.1^{+0.4}_{-0.3}$	$2.7^{+0.9}_{-0.6}$	$1.6^{+0.7}_{-0.4}$	$0.66^{+0.1}_{-0.04}$	fix^{+fix}_{-fix}	48^{+25}_{-21}	458^{+97}_{-26}	205^{+52}_{-95}	$0.0^{+0.0}_{-0.0}$			
	Si IV	36^{+29}_{-9}	25^{+17}_{-13}	$1.4^{+0.3}_{-0.5}$	$3.0^{+0.8}_{-0.7}$	$1.6^{+0.6}_{-1.2}$	$0.76^{+0.07}_{-0.05}$	fix^{+fix}_{-fix}	6^{+17}_{-1}	1134^{+84}_{-451}	36^{+65}_{-8}	$0.0^{+0.0}_{-0.0}$			
J1044+0353	Si II	—	—	—	—	—	—	—	—	—	—	—	—	—	
	Si III	—	—	—	—	—	—	—	—	—	—	—	—	—	
	Si IV	—	—	—	—	—	—	—	—	—	—	—	—	—	
J1105+4444	Si II	48^{+22}_{-15}	36^{+15}_{-11}	$1.6^{+0.2}_{-0.5}$	$3.8^{+0.5}_{-1.3}$	$2.6^{+0.2}_{-1.4}$	$0.92^{+0.04}_{-0.05}$	fix^{+fix}_{-fix}	17^{+19}_{-6}	313^{+32}_{-12}	3^{+7}_{-1}	$0.0^{+0.0}_{-0.0}$			
	Si III	64^{+14}_{-21}	31^{+19}_{-16}	$1.7^{+0.2}_{-0.6}$	$2.4^{+1.3}_{-0.5}$	$-0.0^{+1.5}_{-0.7}$	$0.82^{+0.1}_{-0.08}$	fix^{+fix}_{-fix}	16^{+23}_{-6}	269^{+145}_{-20}	2^{+8}_{-1}	$0.0^{+0.0}_{-0.0}$			
	Si IV	88^{+1}_{-32}	59^{+14}_{-35}	$1.3^{+0.3}_{-0.3}$	$3.3^{+0.8}_{-0.8}$	$0.5^{+0.6}_{-0.9}$	$0.75^{+0.08}_{-0.06}$	fix^{+fix}_{-fix}	14^{+16}_{-4}	272^{+238}_{-24}	3^{+5}_{-1}	$0.0^{+0.0}_{-0.0}$			
J1112+5503	Si II	56^{+19}_{-5}	19^{+17}_{-9}	$1.5^{+0.2}_{-0.6}$	$2.0^{+0.6}_{-0.5}$	$1.4^{+0.2}_{-0.8}$	$0.99^{+0.01}_{-0.04}$	fix^{+fix}_{-fix}	3^{+3}_{-0}	728^{+47}_{-131}	24^{+50}_{-11}	$0.0^{+0.0}_{-0.0}$			
	Si III	87^{+2}_{-27}	78^{+3}_{-49}	$0.8^{+0.3}_{-0.2}$	$2.0^{+0.8}_{-0.4}$	$-0.0^{+1.9}_{-0.7}$	$0.82^{+0.1}_{-0.08}$	fix^{+fix}_{-fix}	25^{+11}_{-9}	957^{+54}_{-33}	111^{+43}_{-34}	$0.0^{+0.0}_{-0.0}$			
	Si IV	58^{+12}_{-14}	31^{+14}_{-16}	$1.9^{+0.2}_{-0.8}$	$4.7^{+0.2}_{-1.0}$	$-0.1^{+1.0}_{-0.3}$	$0.82^{+0.05}_{-0.11}$	fix^{+fix}_{-fix}	112^{+11}_{-34}	947^{+257}_{-75}	3948^{+233}_{-3170}	$0.0^{+0.0}_{-0.0}$			
J1119+5130	Si II	29^{+24}_{-15}	24^{+37}_{-10}	$1.0^{+0.5}_{-0.2}$	$4.3^{+0.4}_{-1.2}$	$-1.8^{+2.4}_{-0.1}$	$0.49^{+0.25}_{-0.27}$	fix^{+fix}_{-fix}	65^{+44}_{-32}	468^{+394}_{-151}	58^{+36}_{-29}	$0.0^{+0.0}_{-0.0}$			
	Si III	—	—	—	—	—	—	—	—	—	—	—	—	—	
	Si IV	54^{+18}_{-16}	9^{+31}_{-5}	$1.5^{+0.2}_{-0.5}$	$3.9^{+0.5}_{-1.0}$	$-1.6^{+2.0}_{-0.2}$	$0.93^{+0.04}_{-0.04}$	fix^{+fix}_{-fix}	23^{+23}_{-11}	891^{+174}_{-532}	19^{+20}_{-9}	$0.0^{+0.0}_{-0.0}$			
J1129+2034	Si II	29^{+7}_{-4}	1^{+7}_{-1}	$0.7^{+0.4}_{-0.1}$	$3.7^{+0.4}_{-1.2}$	$-0.8^{+2.1}_{-0.6}$	$0.97^{+0.02}_{-0.17}$	fix^{+fix}_{-fix}	147^{+1}_{-16}	250^{+27}_{-4}	304^{+185}_{-46}	$0.0^{+0.0}_{-0.0}$			
	Si III	—	—	—	—	—	—	—	—	—	—	—	—	—	
	Si IV	77^{+7}_{-27}	26^{+25}_{-13}	$1.0^{+0.4}_{-0.2}$	$4.4^{+0.3}_{-1.3}$	$0.3^{+1.0}_{-0.9}$	$0.67^{+0.2}_{-0.21}$	fix^{+fix}_{-fix}	22^{+40}_{-12}	321^{+422}_{-79}	65^{+175}_{-34}	$0.0^{+0.0}_{-0.0}$			

Table 7: Parameter Values

Name	Ion	$\alpha(^{\circ})$	$\psi(^{\circ})$	γ	δ	$\log(\tau)$	f_c	$\log(k)$	$v_0(km/s)$	$v_w(km/s)$	$v_{ap}(km/s)$	$\log(n_0)$	RSF	RW	N	
J1132+5722	Si II	87 ₋₅₀ ⁺¹	30 ₋₁₅ ⁺³⁰	1.5 _{-0.4} ^{+0.3}	4.6 _{-1.5} ^{+0.3}	0.9 _{-1.5} ^{+1.1}	0.1 _{-0.04} ^{+0.35}	fix_{-fix}^{+fix}	74 ₋₃₇ ⁺³⁶	1088 ₋₅₃₇ ⁺¹⁰⁷	1 ₋₀ ⁺⁴	0.0 _{-0.0} ^{+0.0}				
Si III	—	—	—	—	—	—	—	fix_{-fix}^{+fix}	—	—	—	—	—	—	—	
Si IV	—	—	—	—	—	—	—	fix_{-fix}^{+fix}	—	—	—	—	—	—	—	
J1132+1411	Si II	—	—	—	—	—	—	fix_{-fix}^{+fix}	—	—	—	—	—	—	—	
Si III	81 ₋₃₅ ⁺⁴	62 ₋₄₃ ⁺¹¹	0.5 _{-0.0} ^{+0.5}	1.3 _{-0.1} ^{+1.9}	0.6 _{-1.0} ^{+1.1}	0.8 _{-0.13} ^{+0.11}	fix_{-fix}^{+fix}	10 ₋₄ ⁺²⁸	206 ₋₉ ⁺¹⁰	23 ₋₇ ⁺⁸⁶	0.0 _{-0.0} ^{+0.0}					
Si IV	36 ₋₇ ⁺¹⁹	19 ₋₁₁ ⁺¹⁷	0.7 _{-0.1} ^{+0.5}	2.4 _{-0.3} ^{+0.9}	2.3 _{-0.8} ^{+0.3}	0.97 _{-0.12} ^{+0.04}	fix_{-fix}^{+fix}	2 ₋₀ ⁺⁵	905 ₋₄₄₄ ⁺¹⁰⁴	6 ₋₁ ⁺⁴⁴	0.0 _{-0.0} ^{+0.0}					
J1144+4012	Si II	86 ₋₂₉ ⁺²	32 ₋₁₆ ⁺¹⁴	1.8 _{-0.5} ^{+0.1}	3.9 _{-1.2} ^{+0.5}	2.8 _{-1.1} ^{+0.1}	0.84 _{-0.04} ^{+0.04}	fix_{-fix}^{+fix}	25 ₋₁₀ ⁺⁸	242 ₋₉ ⁺²⁸	23 ₋₉ ⁺⁸	0.0 _{-0.0} ^{+0.0}				
Si III	—	—	—	—	—	—	—	fix_{-fix}^{+fix}	—	—	—	—	—	—	—	
Si IV	60 ₋₁₉ ⁺¹³	45 ₋₂₇ ⁺¹⁰	1.3 _{-0.4} ^{+0.3}	3.8 _{-1.3} ^{+0.5}	2.0 _{-1.4} ^{+0.4}	0.69 _{-0.07} ^{+0.08}	fix_{-fix}^{+fix}	10 ₋₃ ⁺¹²	848 ₋₂₄₄ ⁺²¹¹	43 ₋₁₈ ⁺⁵³	0.0 _{-0.0} ^{+0.0}					
J1148+2546	Si II	50 ₋₉ ⁺¹⁰	23 ₋₁₃ ⁺⁸	1.6 _{-0.4} ^{+0.2}	4.3 _{-1.3} ^{+0.3}	1.6 _{-0.8} ^{+0.7}	0.77 _{-0.03} ^{+0.03}	fix_{-fix}^{+fix}	12 ₋₅ ⁺⁹	325 ₋₅₃ ⁺³²	288 ₋₁₅₄ ⁺²⁹⁴	0.0 _{-0.0} ^{+0.0}				
Si III	—	—	—	—	—	—	—	fix_{-fix}^{+fix}	—	—	—	—	—	—	—	
Si IV	52 ₋₁₄ ⁺²¹	49 ₋₃₀ ⁺¹⁴	1.7 _{-0.6} ^{+0.1}	3.0 _{-0.6} ^{+0.9}	-1.3 _{-0.3} ^{+1.6}	0.9 _{-0.27} ^{+0.05}	fix_{-fix}^{+fix}	58 ₋₂₈ ⁺¹⁰	340 ₋₉₅ ⁺³¹²	53 ₋₂₅ ⁺⁹	0.0 _{-0.0} ^{+0.0}					
J1150+1501	Si II	69 ₋₂₁ ⁺¹⁰	68 ₋₃₇ ⁺⁷	1.4 _{-0.3} ^{+0.3}	2.6 _{-0.4} ^{+1.0}	2.1 _{-2.7} ^{+0.4}	0.92 _{-0.45} ^{+0.04}	fix_{-fix}^{+fix}	147 ₋₄₃ ⁺¹	268 ₋₁₁ ⁺³⁵	92 ₋₃₀ ⁺¹²	0.0 _{-0.0} ^{+0.0}				
Si III	69 ₋₂₂ ⁺¹¹	40 ₋₂₁ ⁺¹⁸	0.5 _{-0.9} ^{+0.7}	3.9 _{-0.9} ^{+0.5}	-0.5 _{-0.7} ^{+1.6}	0.84 _{-0.28} ^{+0.09}	fix_{-fix}^{+fix}	42 ₋₂₂ ⁺³⁴	1221 ₋₇₉₂ ⁺⁴⁴	35 ₋₂₀ ⁺²³	0.0 _{-0.0} ^{+0.0}					
Si IV	84 ₋₃ ⁺³	61 ₋₆ ⁺⁶	1.1 _{-0.3} ^{+0.5}	3.4 _{-0.9} ^{+1.0}	2.0 _{-1.1} ^{+0.3}	1.0 _{-0.09} ^{+0.0}	fix_{-fix}^{+fix}	3 ₋₁ ⁺⁶	844 ₋₃₁₈ ⁺²¹⁸	2 ₋₁ ⁺⁴	0.0 _{-0.0} ^{+0.0}					
J1157+3220	Si II	-	-5672 ₋₅₆₇₂ ⁺⁵⁶⁷²	-5672 ₋₅₆₇₂ ⁺⁵⁶⁷²	- ₋ ⁺	- ₋ ⁺	- ₋ ⁺	fix_{-fix}^{+fix}	- ₋ ⁺	- ₋ ⁺	- ₋ ⁺	- ₋ ⁺	- ₋ ⁺	- ₋ ⁺	- ₋ ⁺	
Si III	—	—	—	—	—	—	—	fix_{-fix}^{+fix}	—	—	—	—	—	—	—	
Si IV	54 ₋₁₆ ⁺¹⁸	20 ₋₁₀ ⁺²⁷	1.2 _{-0.2} ^{+0.3}	4.2 _{-0.8} ^{+0.4}	0.1 _{-0.2} ^{+0.7}	0.5 _{-0.03} ^{+0.12}	fix_{-fix}^{+fix}	57 ₋₁₈ ⁺⁷	856 ₋₂₄₆ ⁺¹⁸⁷	21 ₋₈ ⁺⁶	0.0 _{-0.0} ^{+0.0}					
J1200+1343	Si II	88 ₋₁₀ ⁺¹	81 ₋₄₃ ⁺⁴	1.1 _{-0.2} ^{+0.5}	3.5 _{-0.6} ^{+0.9}	1.4 _{-0.8} ^{+0.7}	0.65 _{-0.05} ^{+0.09}	fix_{-fix}^{+fix}	48 ₋₁₇ ⁺¹⁰	317 ₋₁₀ ⁺²⁴⁵	200 ₋₅₂ ⁺⁸⁷	0.0 _{-0.0} ^{+0.0}				
Si III	46 ₋₁₂ ⁺¹²	20 ₋₁₁ ⁺¹¹	0.5 _{-0.1} ^{+0.1}	2.2 _{-0.5} ^{+0.3}	2.5 _{-1.1} ^{+0.2}	0.96 _{-0.05} ^{+0.02}	fix_{-fix}^{+fix}	4 ₋₂ ⁺¹⁰	750 ₋₂₆₆ ⁺²⁸⁷	12 ₋₄ ⁺⁴⁴	0.0 _{-0.0} ^{+0.0}					
Si IV	36 ₋₃ ⁺⁴	5 ₋₃ ⁺⁷	2.0 _{-0.5} ^{+0.6}	4.2 _{-1.4} ^{+0.6}	2.2 _{-0.6} ^{+0.5}	0.97 _{-0.06} ^{+0.01}	fix_{-fix}^{+fix}	4 ₋₁ ⁺⁴	1125 ₋₃₅₉ ⁺¹⁹⁷	217 ₋₁₀₇ ⁺⁵⁷	0.0 _{-0.0} ^{+0.0}					
J1225+6109	Si II	46 ₋₁₇ ⁺²⁴	37 ₋₂₀ ⁺¹⁹	1.2 _{-0.4} ^{+0.4}	4.0 _{-1.1} ^{+0.4}	1.6 _{-2.2} ^{+0.7}	0.58 _{-0.26} ^{+0.11}	fix_{-fix}^{+fix}	148 ₋₂₉ ⁺¹	249 ₋₁₅ ⁺¹⁸	33 ₋₁₄ ⁺¹⁸	0.0 _{-0.0} ^{+0.0}				
Si III	—	—	—	—	—	—	—	fix_{-fix}^{+fix}	—	—	—	—	—	—	—	
Si IV	72 ₋₁₇ ⁺¹⁰	40 ₋₂₂ ⁺¹⁸	1.1 _{-0.3} ^{+0.5}	3.9 _{-1.0} ^{+0.6}	0.1 _{-1.0} ^{+1.3}	0.89 _{-0.31} ^{+0.05}	fix_{-fix}^{+fix}	18 ₋₄ ⁺¹⁸	603 ₋₂₈₅ ⁺²⁸⁵	5 ₋₂ ⁺⁵	0.0 _{-0.0} ^{+0.0}					
J1253-0312	Si II	-5672 ₋₅₆₇₂ ⁺⁵⁶⁷²	-5672 ₋₅₆₇₂ ⁺⁵⁶⁷²	- ₋ ⁺	- ₋ ⁺	- ₋ ⁺	fix_{-fix}^{+fix}	- ₋ ⁺	- ₋ ⁺	- ₋ ⁺	- ₋ ⁺	- ₋ ⁺	- ₋ ⁺	- ₋ ⁺	- ₋ ⁺	
Si III	64 ₋₁₄ ⁺¹³	23 ₋₁₂ ⁺¹⁵	1.2 _{-0.3} ^{+0.3}	4.3 _{-1.5} ^{+0.4}	1.3 _{-0.6} ^{+0.7}	1.0 _{-0.04} ^{+0.0}	fix_{-fix}^{+fix}	15 ₋₁₀ ⁺¹⁴	498 ₋₁₇₇ ⁺³⁵	23 ₋₁₆ ⁺²²	0.0 _{-0.0} ^{+0.0}					
Si IV	—	—	—	—	—	—	—	fix_{-fix}^{+fix}	—	—	—	—	—	—	—	
J1314+3452	Si II	85 ₋₁₃ ⁺³	21 ₋₁₀ ⁺²⁴	1.2 _{-0.3} ^{+0.5}	1.7 _{-0.2} ^{+1.3}	-1.6 _{-0.2} ^{+1.6}	0.92 _{-0.13} ^{+0.02}	fix_{-fix}^{+fix}	18 ₋₅ ⁺⁷	295 ₋₁₁ ⁺⁶⁵	52 ₋₁₄ ⁺²³	0.0 _{-0.0} ^{+0.0}				
Si III	41 ₋₈ ⁺¹³	21 ₋₁₂ ⁺¹⁰	0.6 _{-0.1} ^{+0.2}	2.5 _{-0.6} ^{+0.6}	2.7 _{-1.8} ^{+0.2}	0.99 _{-0.08} ^{+0.01}	fix_{-fix}^{+fix}	2 ₋₀ ⁺⁸	205 ₋₈₅ ⁺⁶⁴	4 ₋₀ ⁺²⁸	0.0 _{-0.0} ^{+0.0}					
Si IV	32 ₋₆ ⁺²⁷	19 ₋₁₀ ⁺¹⁵	0.6 _{-0.0} ^{+0.2}	1.9 _{-0.3} ^{+0.4}	1.4 _{-1.0} ^{+0.4}	0.89 _{-0.13} ^{+0.06}	fix_{-fix}^{+fix}	2 ₋₀ ⁺⁴	527 ₋₂₃₀ ⁺⁶⁴	4 ₋₀ ⁺⁹	0.0 _{-0.0} ^{+0.0}					
J1323-0132	Si II	-5672 ₋₅₆₇₂ ⁺⁵⁶⁷²	-5672 ₋₅₆₇₂ ⁺⁵⁶⁷²	- ₋ ⁺	- ₋ ⁺	- ₋ ⁺	fix_{-fix}^{+fix}	- ₋ ⁺	- ₋ ⁺	- ₋ ⁺	- ₋ ⁺	- ₋ ⁺	- ₋ ⁺	- ₋ ⁺	- ₋ ⁺	
Si III	76 ₋₂₇ ⁺⁵	79 ₋₂₅ ⁺³	1.6 _{-0.3} ^{+0.2}	3.5 _{-0.6} ^{+0.6}	0.4 _{-0.8} ^{+1.5}	0.98 _{-0.29} ^{+0.01}	fix_{-fix}^{+fix}	33 ₋₉ ⁺¹⁶	433 ₋₁₉₆ ⁺²³	539 ₋₁₆₈ ⁺²³³	0.0 _{-0.0} ^{+0.0}					
Si IV	—	—	—	—	—	—	—	fix_{-fix}^{+fix}	—	—	—	—	—	—	—	

Table 8: Parameter Values

Name	Ion	$\alpha(^{\circ})$	$\psi(^{\circ})$	γ	δ	$\log(\tau)$	f_c	$\log(k)$	$v_0(km/s)$	$v_{lu}(km/s)$	$v_{ap}(km/s)$	$\log(n_0)$	RSF	RAW	N
J1359+5726	Si II	68^{+12}_{-19}	10^{+31}_{-5}	$1.0^{+0.4}_{-0.3}$	$4.1^{+0.4}_{-1.1}$	$0.3^{+1.0}_{-1.1}$	$0.53^{+0.18}_{-0.07}$	fix^{+fix}_{-fix}	25^{+21}_{-11}	1028^{+134}_{-443}	97^{+118}_{-38}	$0.0^{+0.0}_{-0.0}$			
	Si III	86^{+2}_{-24}	45^{+12}_{-24}	$0.5^{+1.0}_{-0.0}$	$1.6^{+1.5}_{-0.1}$	$1.3^{+0.9}_{-0.6}$	$0.99^{+0.01}_{-0.05}$	fix^{+fix}_{-fix}	2^{+4}_{-0}	495^{+51}_{-42}	2^{+5}_{-0}	$0.0^{+0.0}_{-0.0}$			
	Si IV	78^{+7}_{-29}	22^{+19}_{-11}	$1.7^{+0.2}_{-0.5}$	$4.0^{+0.4}_{-1.2}$	$1.1^{+0.9}_{-0.8}$	$0.84^{+0.03}_{-0.06}$	fix^{+fix}_{-fix}	11^{+7}_{-3}	861^{+232}_{-361}	13^{+8}_{-4}	$0.0^{+0.0}_{-0.0}$			
J1416+1223	Si II	—	—	—	—	—	—	—	—	—	—	—	—	—	—
	Si III	—	—	—	—	—	—	—	—	—	—	—	—	—	—
	Si IV	—	—	—	—	—	—	—	—	—	—	—	—	—	—
J1418+2102	Si II	-5672^{+5672}_{-5672}	-5672^{+5672}_{-5672}	$-^{+-}$	$-^{+-}$	$-^{+-}$	$-^{+-}$	$-^{+-}$	fix^{+fix}_{-fix}	$-^{+-}$	$-^{+-}$	$-^{+-}$	$-^{+-}$	$-^{+-}$	$-^{+-}$
	Si III	—	—	—	—	—	—	—	—	—	—	—	—	—	—
	Si IV	2^{+30}_{-1}	88^{+1}_{-35}	$1.3^{+0.4}_{-0.4}$	$3.9^{+0.5}_{-1.1}$	$0.7^{+1.1}_{-1.4}$	$0.27^{+0.32}_{-0.14}$	fix^{+fix}_{-fix}	106^{+22}_{-53}	283^{+408}_{-48}	398^{+248}_{-221}	$0.0^{+0.0}_{-0.0}$			
J1428+1653	Si II	72^{+5}_{-6}	69^{+4}_{-10}	$1.4^{+0.4}_{-0.2}$	$2.1^{+1.3}_{-0.7}$	$1.6^{+0.6}_{-0.8}$	$0.45^{+0.07}_{-0.07}$	fix^{+fix}_{-fix}	40^{+12}_{-10}	444^{+43}_{-13}	476^{+371}_{-75}	$0.0^{+0.0}_{-0.0}$			
	Si III	80^{+5}_{-28}	6^{+22}_{-3}	$1.0^{+0.3}_{-0.3}$	$2.2^{+0.7}_{-0.4}$	$1.2^{+0.9}_{-0.7}$	$0.95^{+0.03}_{-0.05}$	fix^{+fix}_{-fix}	3^{+6}_{-0}	1106^{+94}_{-251}	10^{+22}_{-2}	$0.0^{+0.0}_{-0.0}$			
	Si IV	45^{+9}_{-13}	24^{+19}_{-13}	$1.4^{+0.2}_{-0.6}$	$4.6^{+0.2}_{-2.3}$	$2.9^{+0.1}_{-0.5}$	$0.9^{+0.05}_{-0.05}$	fix^{+fix}_{-fix}	9^{+5}_{-8}	1102^{+81}_{-674}	61^{+75}_{-42}	$0.0^{+0.0}_{-0.0}$			
J1429+0643	Si II	88^{+1}_{-7}	66^{+6}_{-24}	$0.7^{+0.3}_{-0.1}$	$2.9^{+0.5}_{-0.5}$	$0.6^{+0.7}_{-0.6}$	$0.59^{+0.09}_{-0.03}$	fix^{+fix}_{-fix}	54^{+12}_{-14}	963^{+156}_{-276}	233^{+133}_{-25}	$0.0^{+0.0}_{-0.0}$			
	Si III	54^{+10}_{-13}	5^{+2}_{-2}	$1.7^{+0.1}_{-0.6}$	$2.5^{+1.1}_{-0.4}$	$2.6^{+0.2}_{-2.4}$	$0.89^{+0.05}_{-0.1}$	fix^{+fix}_{-fix}	73^{+30}_{-39}	458^{+450}_{-12}	2827^{+1874}_{-2120}	$0.0^{+0.0}_{-0.0}$			
	Si IV	57^{+8}_{-11}	4^{+13}_{-12}	$1.8^{+0.1}_{-0.8}$	$4.4^{+0.4}_{-1.2}$	$-0.9^{+1.4}_{-0.3}$	$0.99^{+0.01}_{-0.16}$	fix^{+fix}_{-fix}	117^{+33}_{-39}	629^{+134}_{-66}	5937^{+1675}_{-4843}	$0.0^{+0.0}_{-0.0}$			
J1444+4237	Si II	65^{+15}_{-10}	4^{+20}_{-2}	$1.0^{+0.2}_{-0.2}$	$2.7^{+0.6}_{-0.5}$	$2.0^{+0.6}_{-0.8}$	$0.96^{+0.02}_{-0.05}$	fix^{+fix}_{-fix}	2^{+2}_{-0}	278^{+97}_{-29}	13^{+24}_{-3}	$0.0^{+0.0}_{-0.0}$			
	Si III	—	—	—	—	—	—	—	—	—	—	—	—	—	—
	Si IV	16^{+40}_{-7}	73^{+7}_{-46}	$1.2^{+0.4}_{-0.5}$	$2.2^{+1.6}_{-0.3}$	$0.2^{+1.4}_{-1.7}$	$0.87^{+0.06}_{-0.33}$	fix^{+fix}_{-fix}	20^{+50}_{-9}	261^{+485}_{-55}	0^{+3}_{-0}	$0.0^{+0.0}_{-0.0}$			
J1448-0110	Si II	15^{+46}_{-4}	5^{+31}_{-3}	$0.9^{+0.4}_{-0.2}$	$4.0^{+0.4}_{-1.0}$	$2.1^{+0.5}_{-2.0}$	$0.62^{+0.11}_{-0.06}$	fix^{+fix}_{-fix}	15^{+40}_{-5}	262^{+39}_{-19}	77^{+369}_{-20}	$0.0^{+0.0}_{-0.0}$			
	Si III	—	—	—	—	—	—	—	—	—	—	—	—	—	—
	Si IV	—	—	—	—	—	—	—	—	—	—	—	—	—	—
J1521+0759	Si II	-5672^{+5672}_{-5672}	-5672^{+5672}_{-5672}	$-^{+-}$	$-^{+-}$	$-^{+-}$	$-^{+-}$	$-^{+-}$	fix^{+fix}_{-fix}	$-^{+-}$	$-^{+-}$	$-^{+-}$	$-^{+-}$	$-^{+-}$	$-^{+-}$
	Si III	51^{+19}_{-13}	33^{+14}_{-18}	$0.6^{+0.4}_{-0.0}$	$1.2^{+1.5}_{-0.1}$	$-2.0^{+3.2}_{-0.0}$	$0.65^{+0.07}_{-0.07}$	fix^{+fix}_{-fix}	35^{+6}_{-21}	792^{+267}_{-119}	87^{+46}_{-43}	$0.0^{+0.0}_{-0.0}$			
	Si IV	67^{+11}_{-19}	34^{+19}_{-19}	$0.9^{+0.3}_{-0.2}$	$3.7^{+0.9}_{-0.4}$	$2.4^{+0.3}_{-1.6}$	$0.32^{+0.14}_{-0.11}$	fix^{+fix}_{-fix}	22^{+34}_{-6}	1234^{+33}_{-366}	82^{+139}_{-23}	$0.0^{+0.0}_{-0.0}$			
J1525+0757	Si II	58^{+11}_{-17}	53^{+12}_{-20}	$0.8^{+0.3}_{-0.1}$	$4.1^{+0.2}_{-1.4}$	$2.1^{+0.5}_{-0.9}$	$0.86^{+0.03}_{-0.04}$	fix^{+fix}_{-fix}	64^{+9}_{-30}	676^{+48}_{-66}	243^{+126}_{-101}	$0.0^{+0.0}_{-0.0}$			
	Si III	66^{+13}_{-21}	6^{+26}_{-3}	$0.6^{+0.3}_{-0.0}$	$3.8^{+0.3}_{-0.9}$	$2.2^{+0.4}_{-1.1}$	$0.89^{+0.05}_{-0.04}$	fix^{+fix}_{-fix}	72^{+17}_{-29}	1003^{+174}_{-262}	184^{+78}_{-59}	$0.0^{+0.0}_{-0.0}$			
	Si IV	83^{+3}_{-30}	75^{+4}_{-44}	$0.8^{+0.4}_{-0.2}$	$4.1^{+0.3}_{-1.1}$	$0.7^{+0.8}_{-0.6}$	$0.74^{+0.06}_{-0.1}$	fix^{+fix}_{-fix}	94^{+21}_{-44}	710^{+137}_{-83}	367^{+340}_{-143}	$0.0^{+0.0}_{-0.0}$			
J1545+0858	Si II	28^{+37}_{-8}	4^{+23}_{-2}	$2.0^{+0.0}_{-0.6}$	$3.2^{+0.9}_{-0.8}$	$1.5^{+0.8}_{-0.7}$	$0.79^{+0.01}_{-0.03}$	fix^{+fix}_{-fix}	7^{+11}_{-2}	388^{+27}_{-14}	9^{+12}_{-3}	$0.0^{+0.0}_{-0.0}$			
	Si III	—	—	—	—	—	—	—	—	—	—	—	—	—	—
	Si IV	32^{+23}_{-4}	18^{+19}_{-10}	$0.6^{+0.5}_{-0.0}$	$2.4^{+1.0}_{-0.4}$	$2.6^{+0.2}_{-1.0}$	$0.62^{+0.07}_{-0.04}$	fix^{+fix}_{-fix}	4^{+9}_{-1}	568^{+233}_{-200}	10^{+53}_{-3}	$0.0^{+0.0}_{-0.0}$			
J1612+0817	Si II	32^{+15}_{-8}	8^{+26}_{-4}	$2.0^{+0.0}_{-1.0}$	$4.8^{+0.1}_{-0.1}$	$1.7^{+0.8}_{-0.8}$	$0.72^{+0.04}_{-0.07}$	fix^{+fix}_{-fix}	44^{+9}_{-14}	780^{+83}_{-26}	1739^{+301}_{-152}	$0.0^{+0.0}_{-0.0}$			
	Si III	43^{+17}_{-11}	10^{+16}_{-5}	$1.6^{+0.2}_{-0.7}$	$3.9^{+0.4}_{-1.6}$	$2.6^{+0.2}_{-1.0}$	$0.96^{+0.02}_{-0.07}$	fix^{+fix}_{-fix}	8^{+10}_{-3}	853^{+133}_{-60}	141^{+151}_{-87}	$0.0^{+0.0}_{-0.0}$			
	Si IV	—	—	—	—	—	—	—	—	—	—	—	—	—	—
Average	Put averages here														

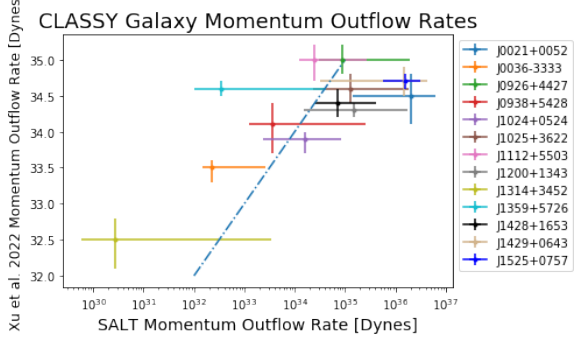


Figure 10: Our SALT predicted momentum outflow rates for the CLASSY galaxies vs. the Xu et al. 2022 predicted momentum outflow rates. While there exists a positive correlation between these two predictions, our predictions tend to be about an order of magnitude smaller.

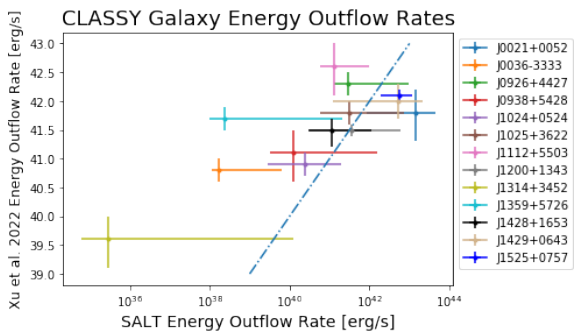


Figure 11: Our SALT predicted energy outflow rates for the CLASSY galaxies vs. the Xu et al. 2022 predicted energy outflow rates. While there exists a positive correlation between these two predictions, our predictions tend to be several orders of magnitude smaller.

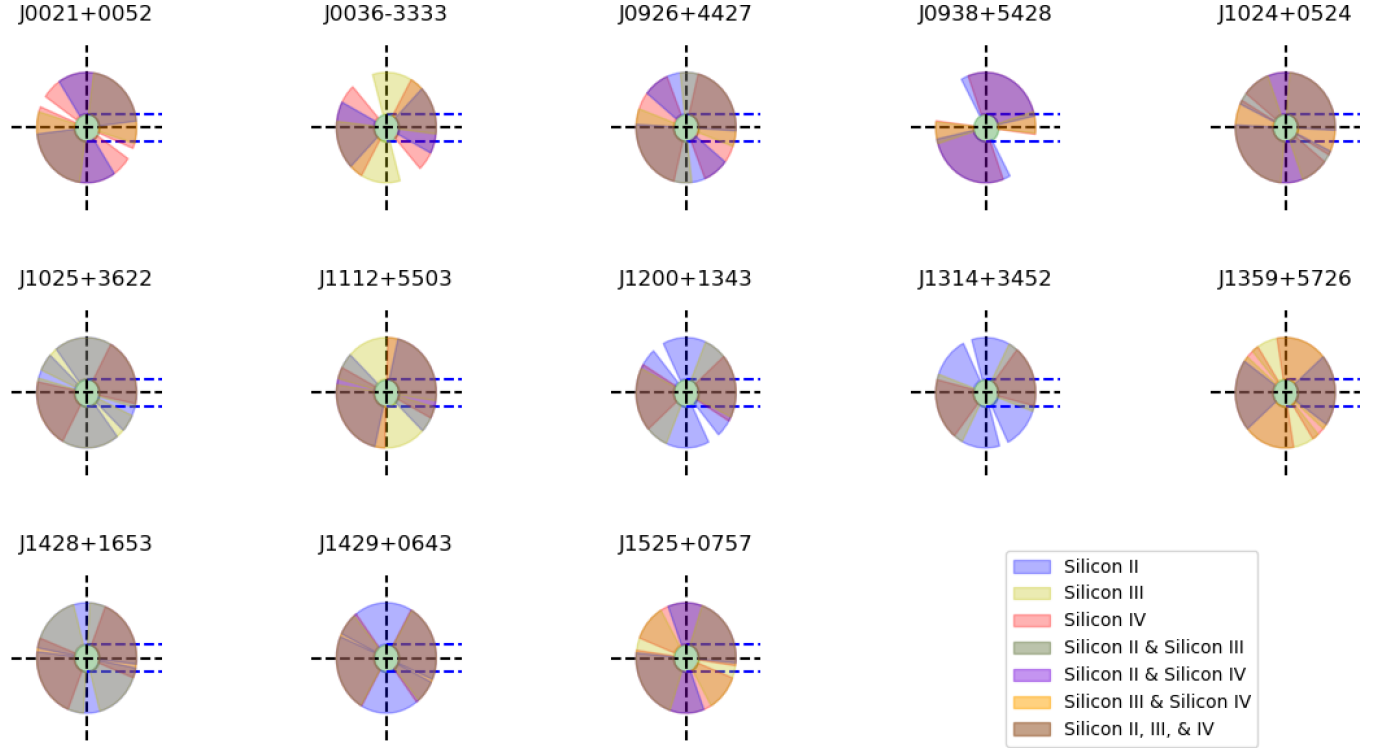


Figure 12: Composite illustrations of outflows for the 13 CLASSY galaxies that the mass outflow rates are calculated for. Large opening angles are observed in most (but not all!) ionization states of each galaxy.

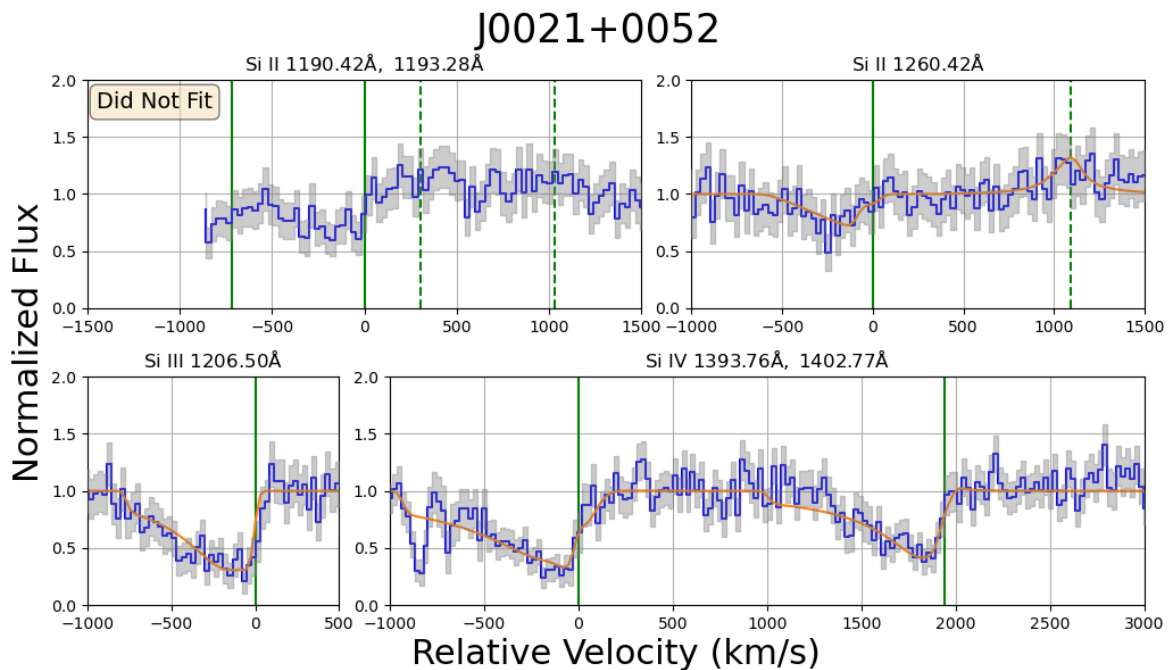


Figure 13: SALT fits for J0021+0052. The Si II 1190.42Å/1193.28Å doublet was not fit due to lack of data in the region of interest.

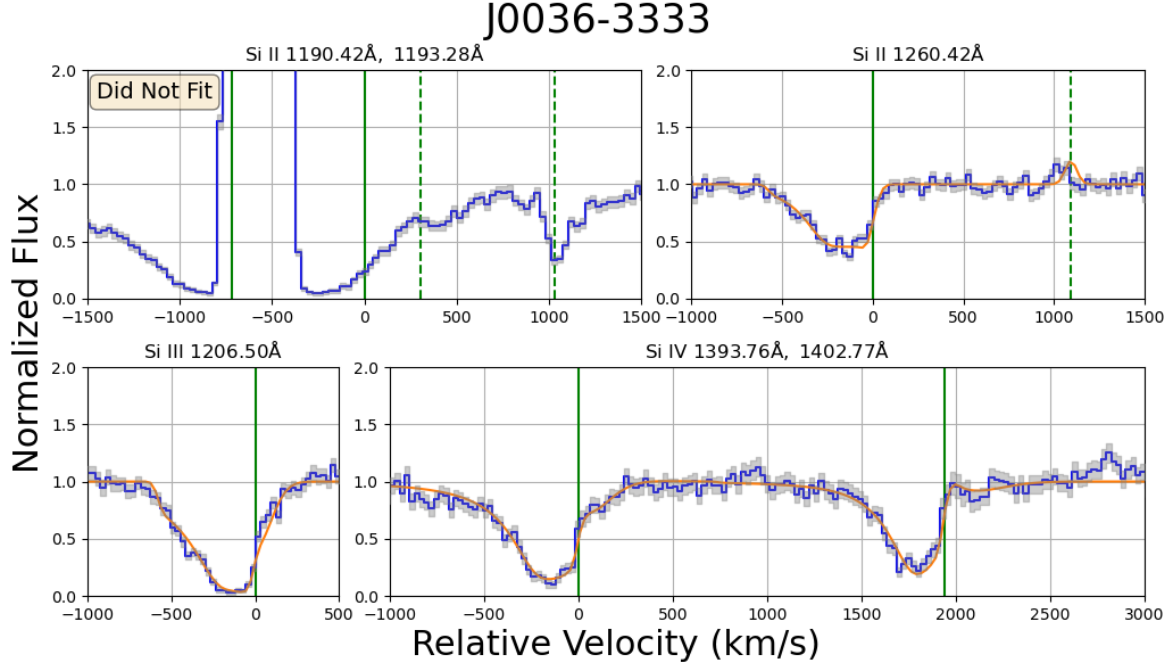


Figure 14: SALT fits for J0036-3333. The Si II 1190.42Å/1193.28Å doublet was not fit due to geocoronal Lyman α contamination.

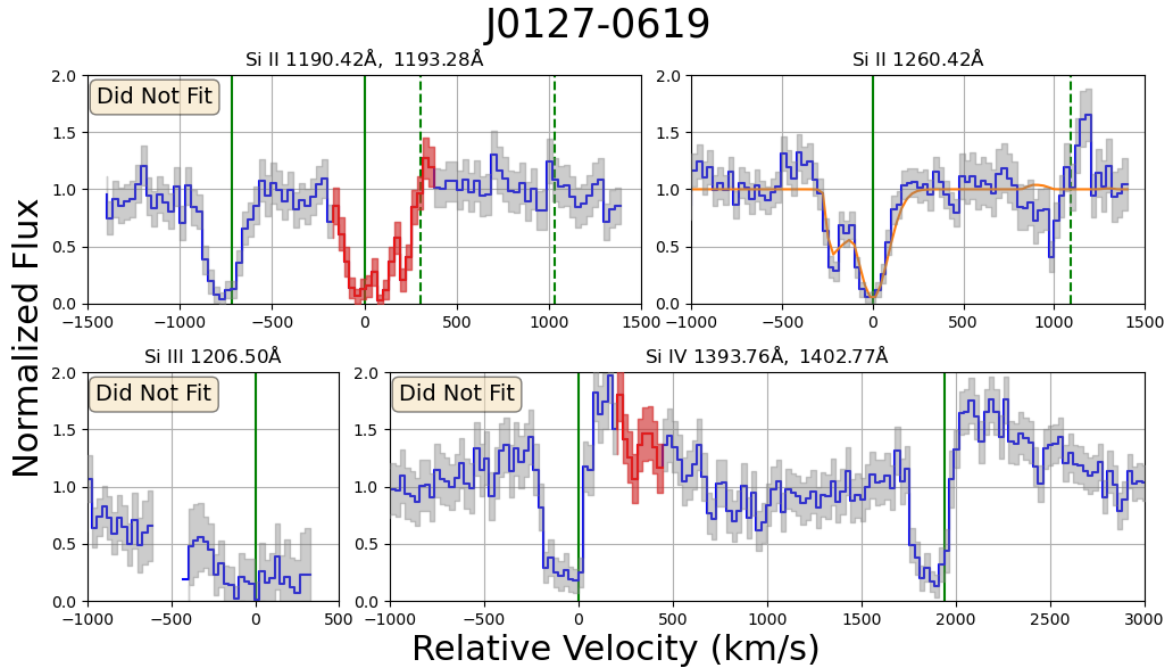


Figure 15: SALT fits for J0127-0619. The Si II 1190.42Å/1193.28Å doublet was not fit due to Milky Way contamination. The Si III 1206.50Å line was not fit due to interference from the nearby geocoronal Lyman α line. The Si IV 1393.76Å/1402.77Å doublet was not fit due to failure to normalization.

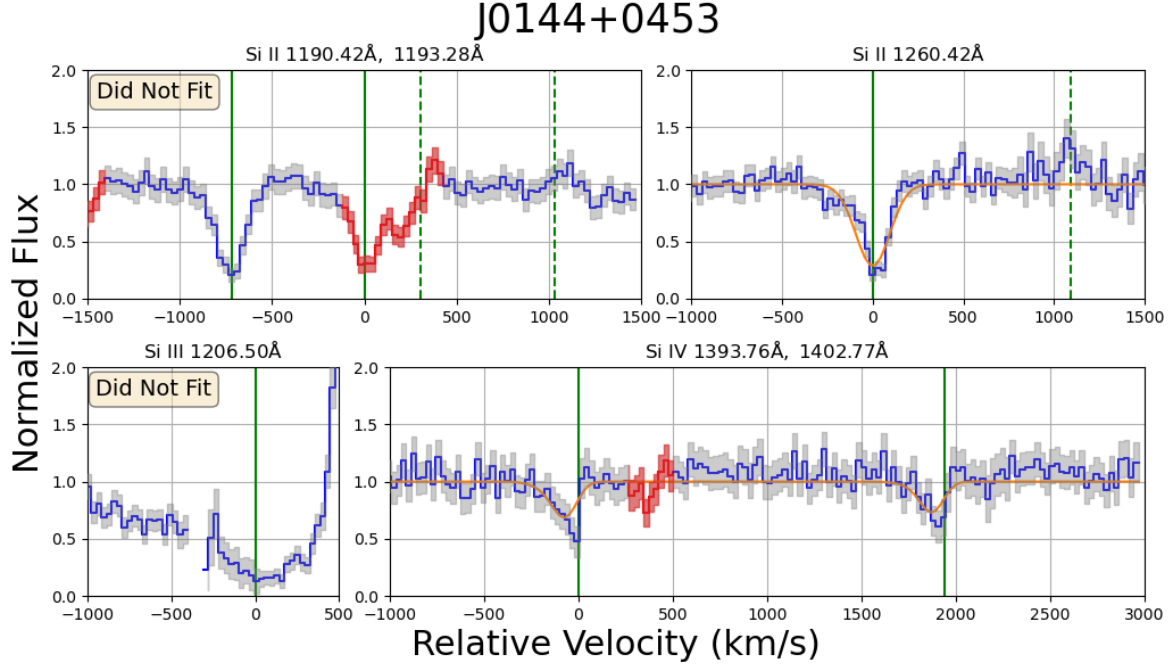


Figure 16: SALT fits for J0144+0453. The Si II 1190.42Å/1193.28Å doublet was not fit due to Milky Way contamination. The Si III 1206.50Å line was not fit due to interference from the nearby geocoronal Lyman α line.

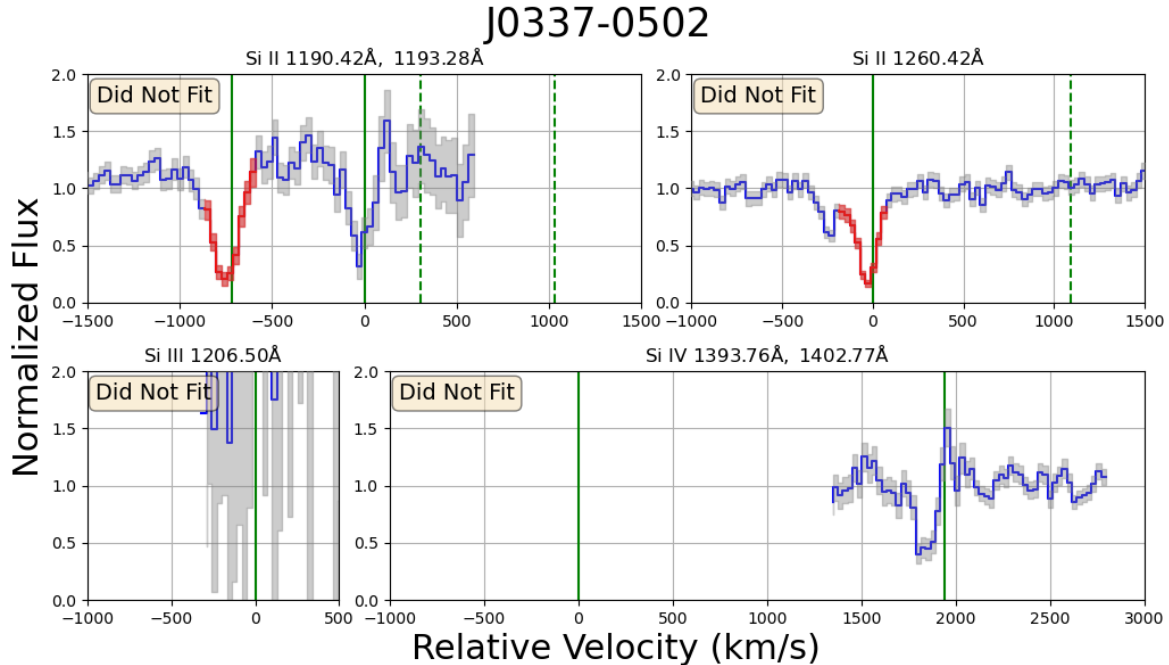


Figure 17: No SALT fits were made for J0337-0502. The Si II 1190.42Å/1193.28Å doublet and the 1260.42Å line was not fit due to Milky Way contamination. The Si III 1206.50Å line was not fit due to noise.

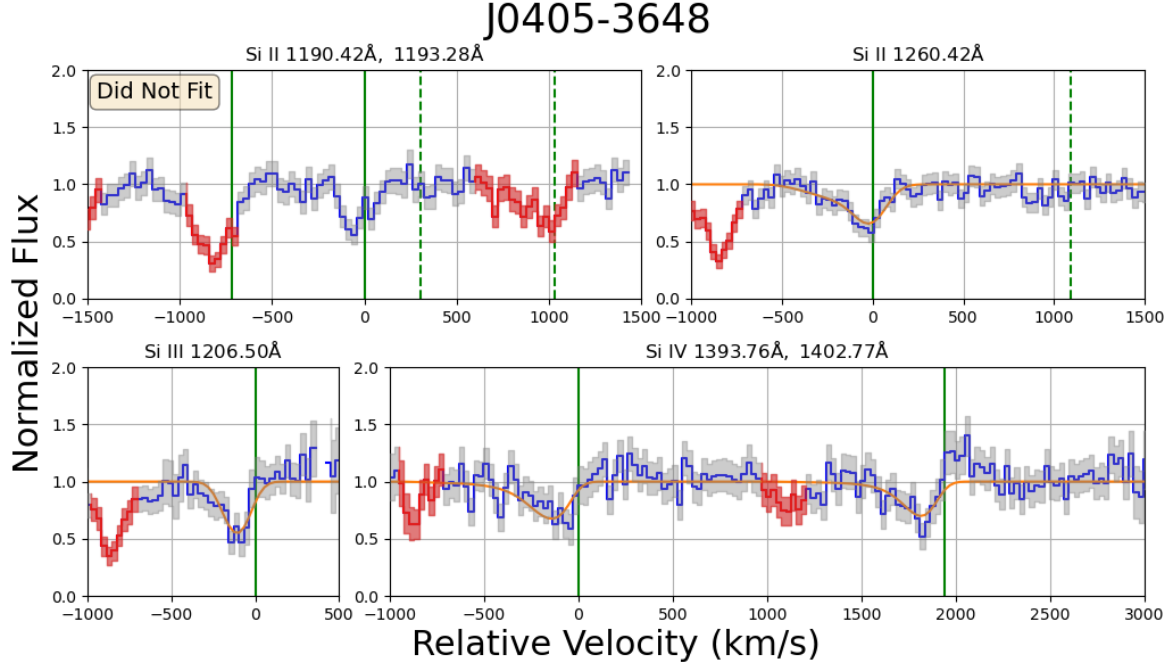


Figure 18: SALT fits for J0405-3648. The Si II 1190.42Å/1193.28Å doublet was not fit due to Milky Way contamination.

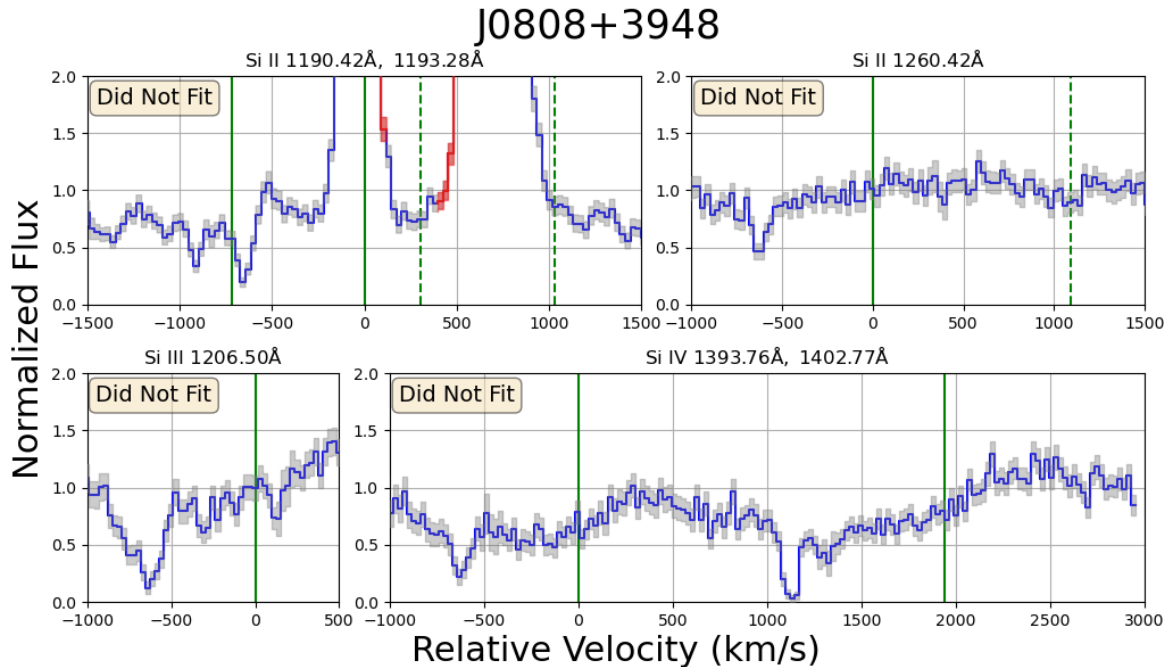


Figure 19: No SALT fits were made for J0808+3948. For all relevant lines, SALT was unable to locate and model an appropriate P-Cygni profile.

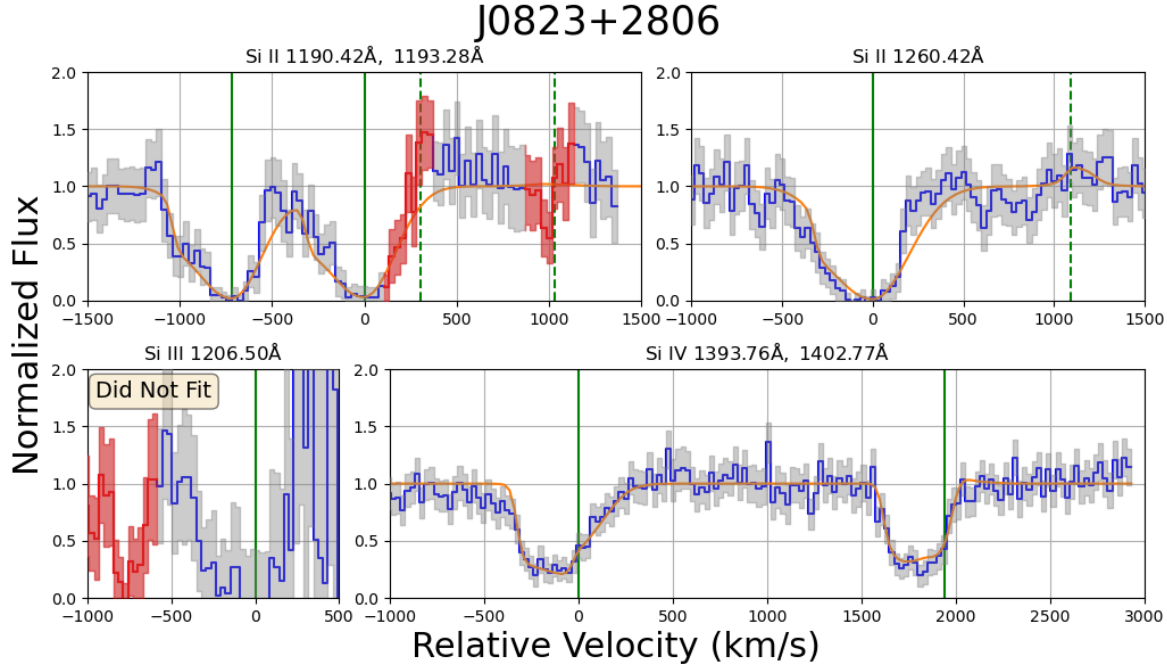


Figure 20: SALT fits for J0823+2806. The Si III 1206.50Å line was not fit due to noise.

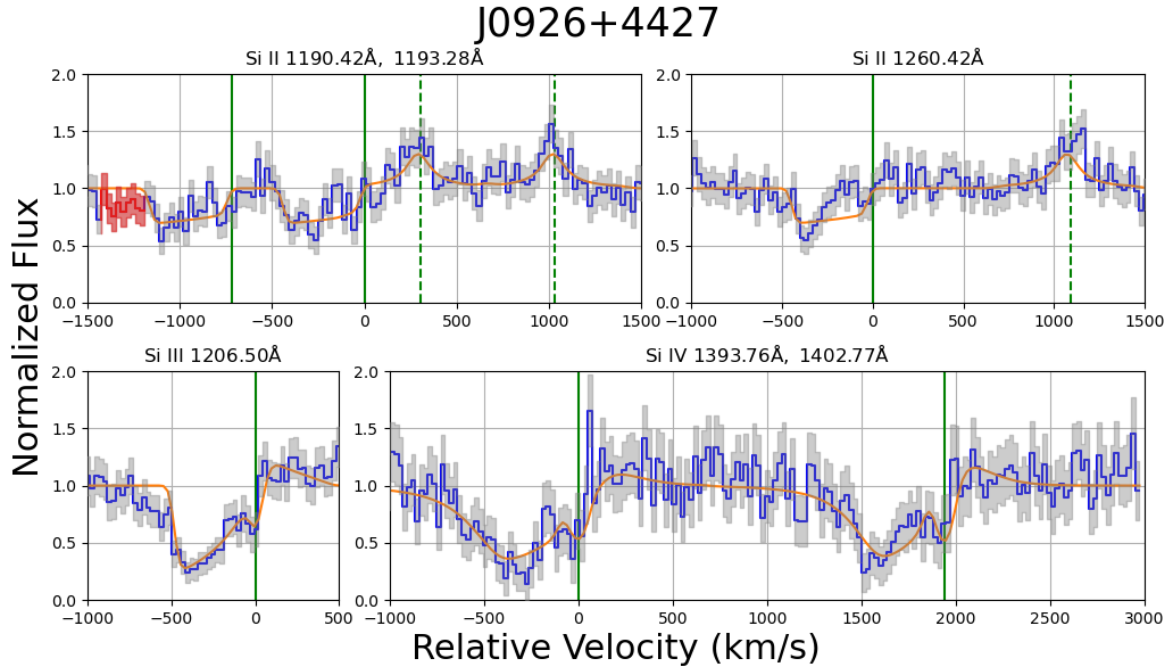


Figure 21: SALT fits for J0926+4427.

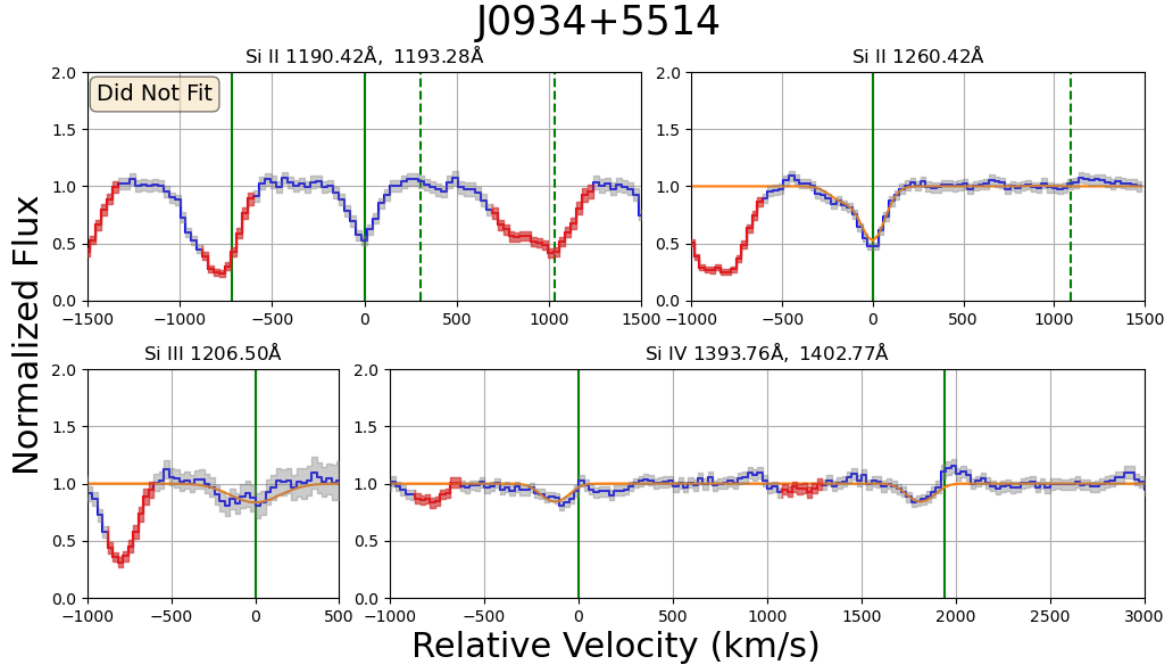


Figure 22: SALT fits for J0934+5514. The Si II 1190.42Å/1193.28Å doublet was not fit due to Milky Way contamination.

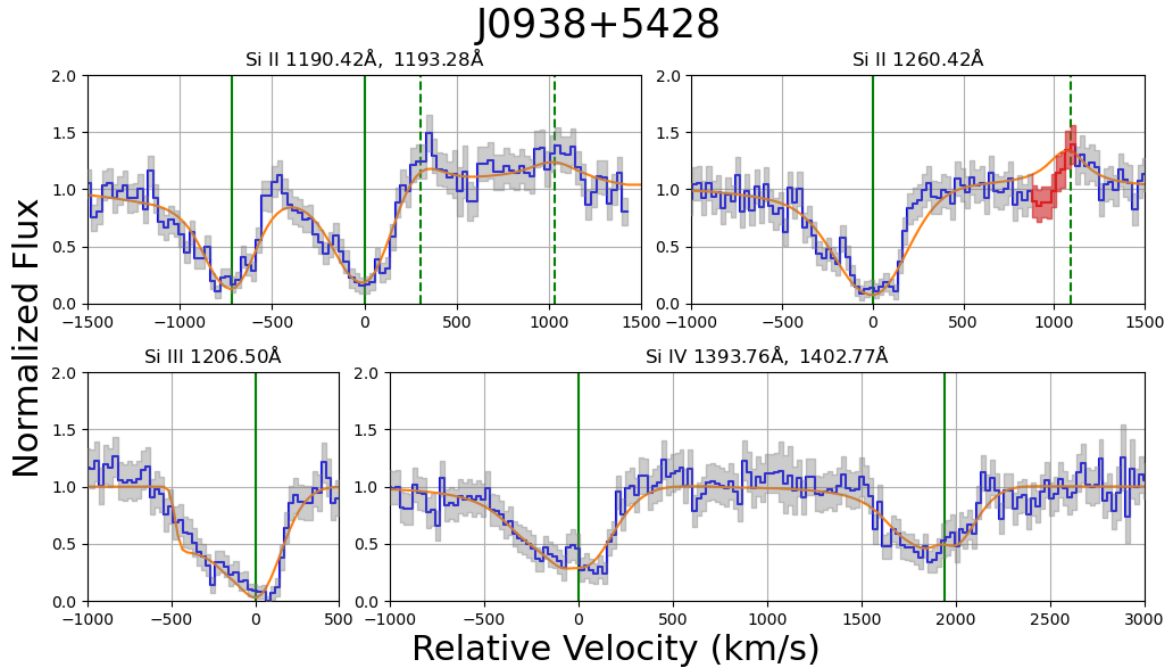


Figure 23: SALT fits for J0938+5428.

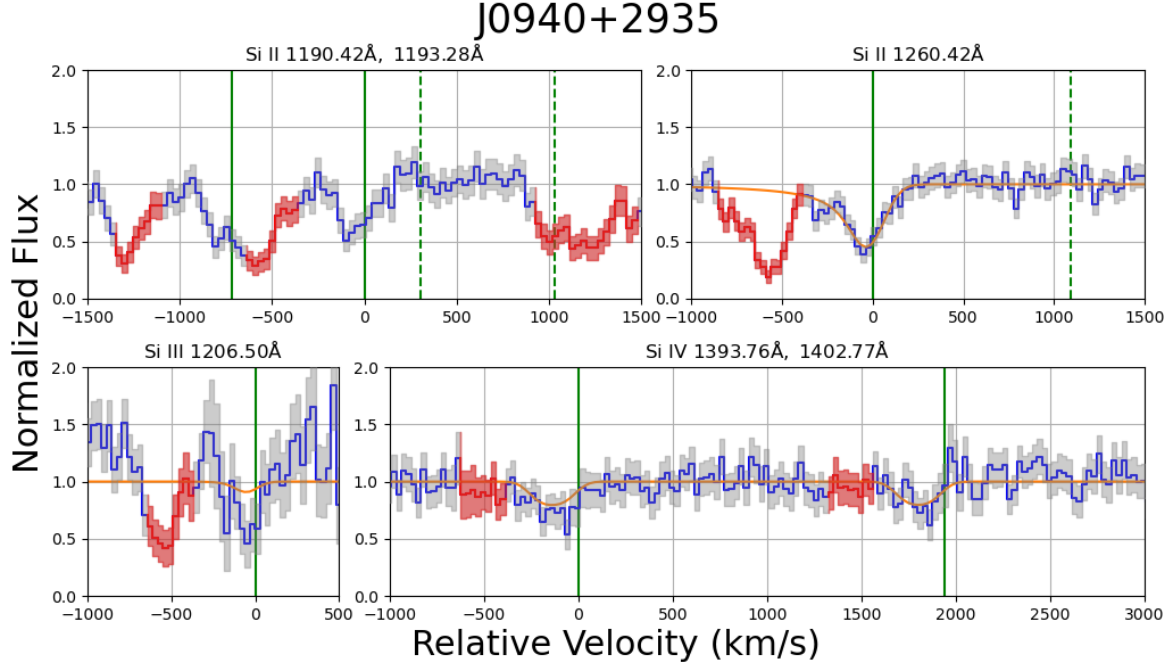


Figure 24: SALT fits for J0940+2935.

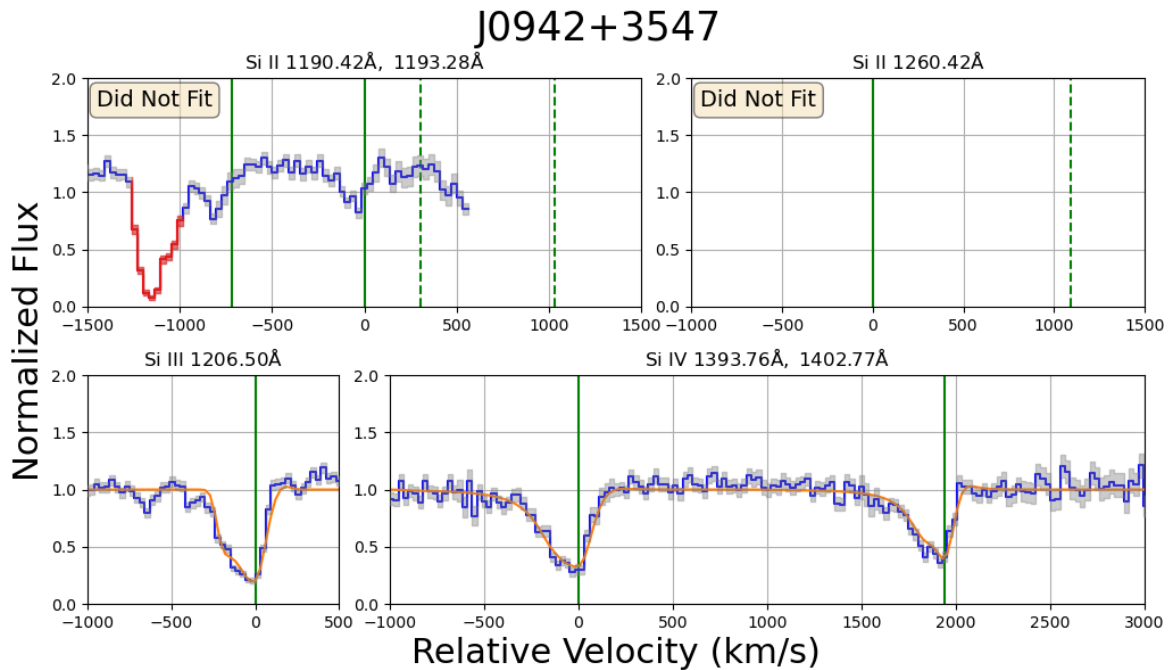


Figure 25: SALT fits for J0942+3547. The Si II 1190.42Å/1193.28Å doublet and the 1260.42Å line was not fit due to lack of data in the region of interest.

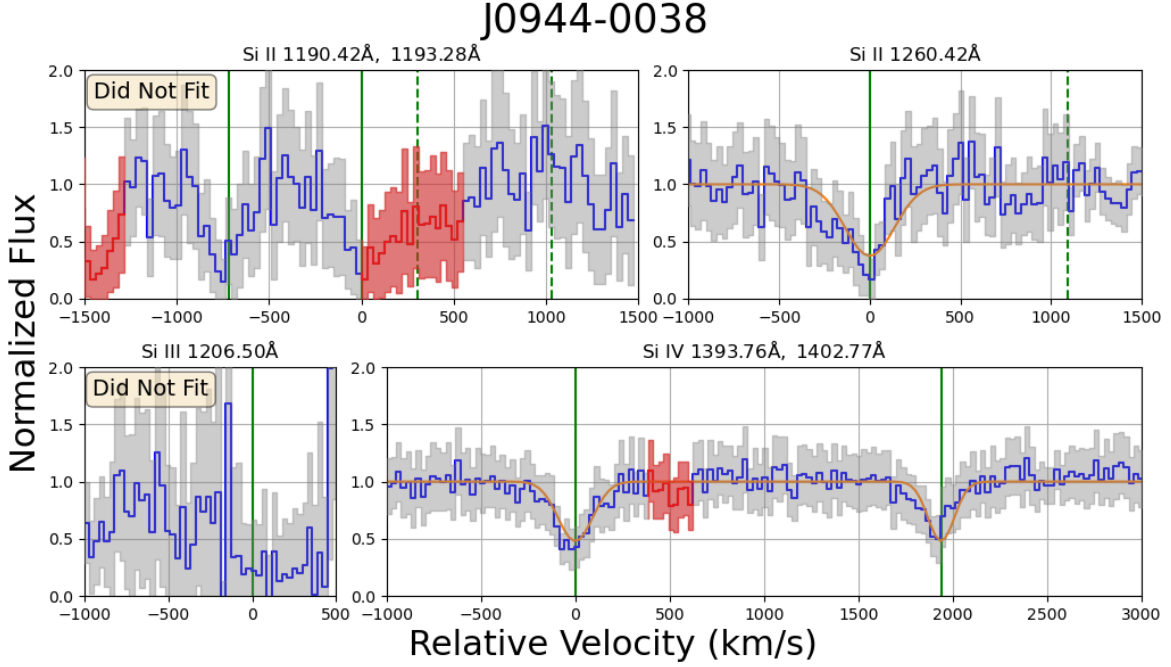


Figure 26: SALT fits for J0944-0038. The Si II 1190.42Å/1193.28Å doublet was not fit due to Milky Way contamination. The Si III 1206.50Å line was not fit due to noise.

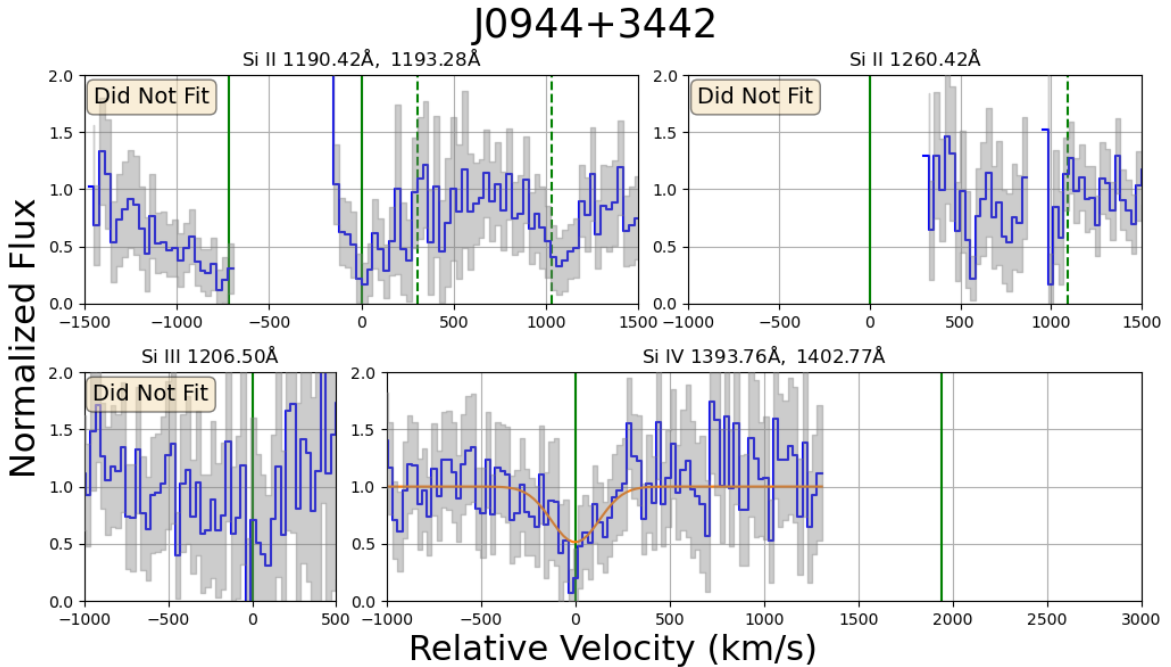


Figure 27: SALT fits for J0944+3442. The Si II 1190.42Å/1193.28Å doublet and the 1260.42Å line were not fit due to lack of data in the region of interest and the geocoronal Lyman α line. The Si III 1206.50Å line was not fit due to noise.

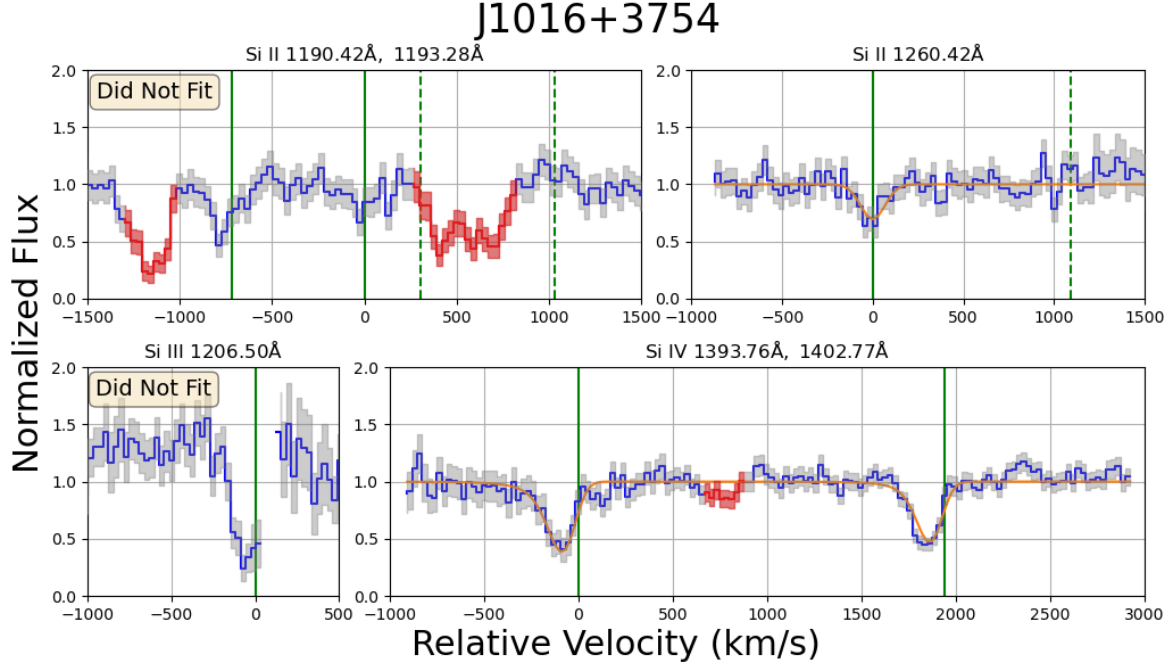


Figure 28: SALT fits for J1016+3754. The Si II 1190.42Å/1193.28Å doublet was not fit due to Milky Way contamination. The Si III 1206.50Å line was not fit due to lack of data in the region of interest.

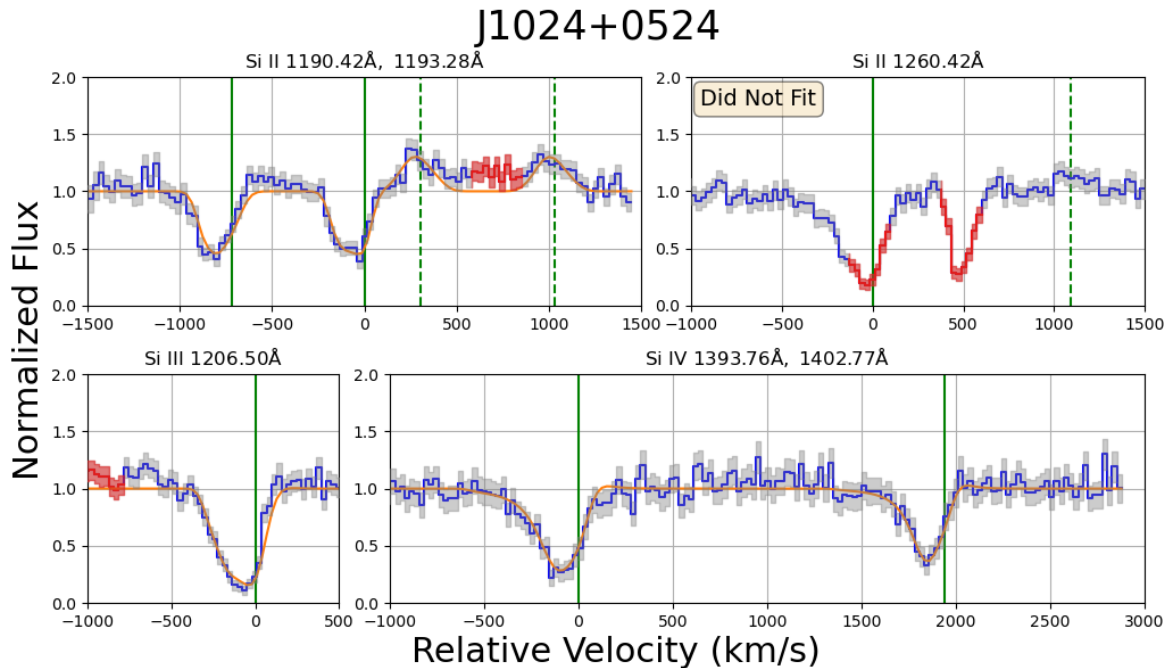


Figure 29: SALT fits for J1024+0524. The Si II 1260.42Å line was not fit due to Milky Way contamination.

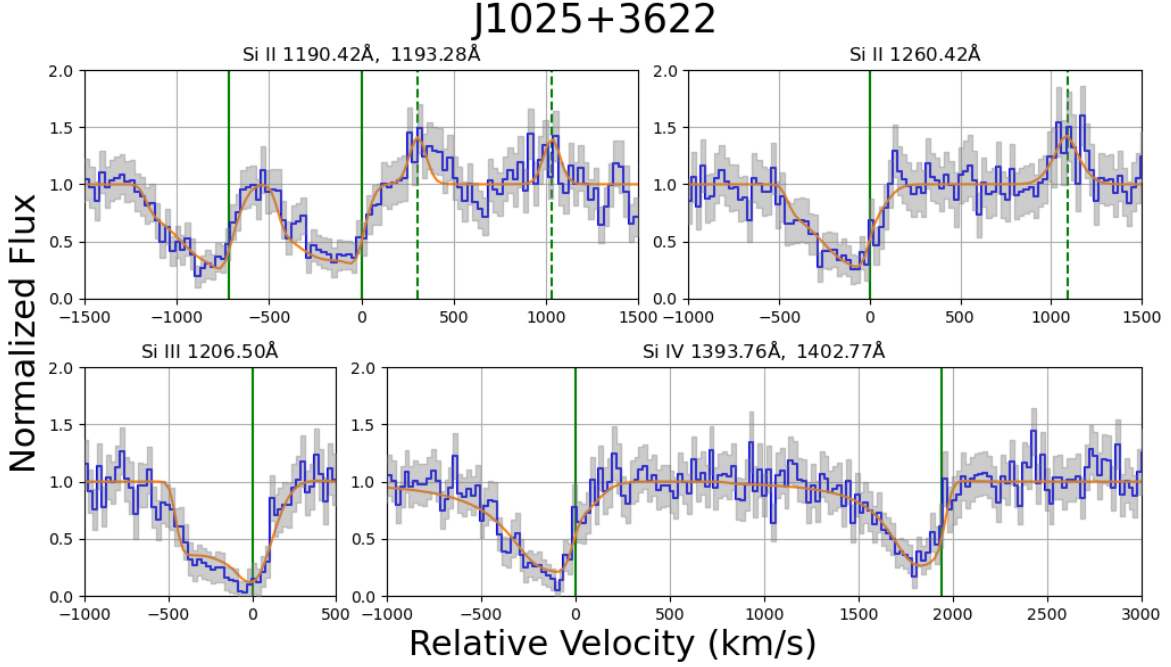


Figure 30: SALT fits for J1025+3622.

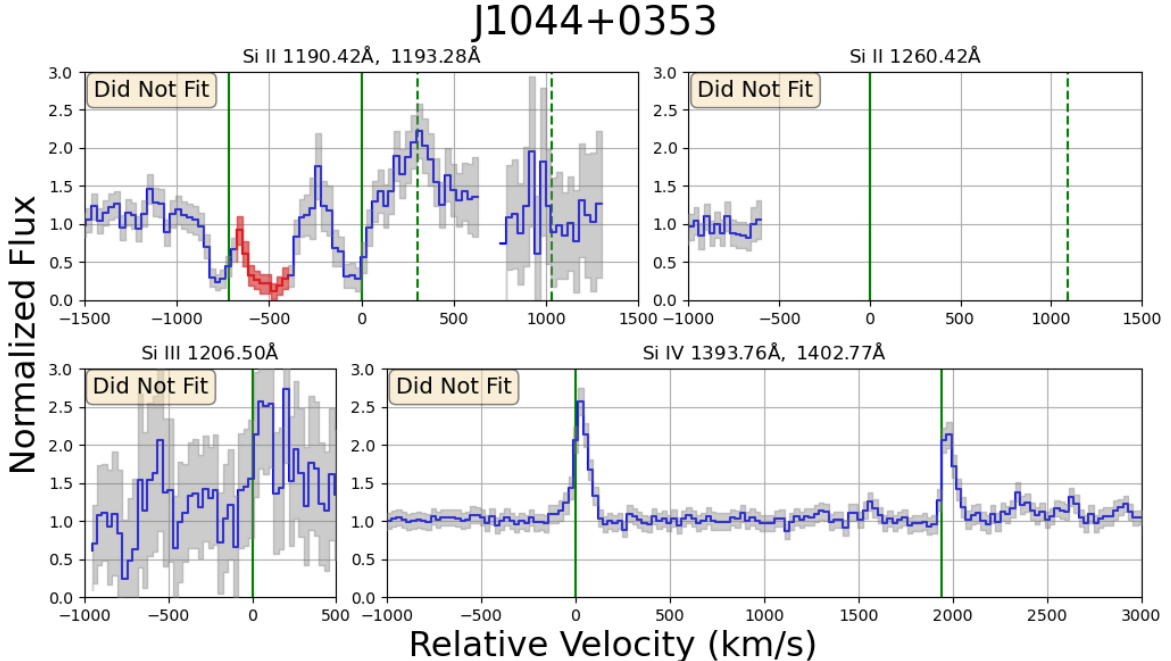


Figure 31: No SALT fits were made for J1044+0353. The Si II 1190.42Å/1193.28Å doublet and the 1260.42Å line were not fit due to lack of data in the region of interest. The Si III 1206.50Å line was not fit due to noise. The Si IV 1393.76Å/1402.77Å doublet was not fit due to the appearance that these lines resulted from nebular emission, as opposed to absorption and emission resulting from the CGM.

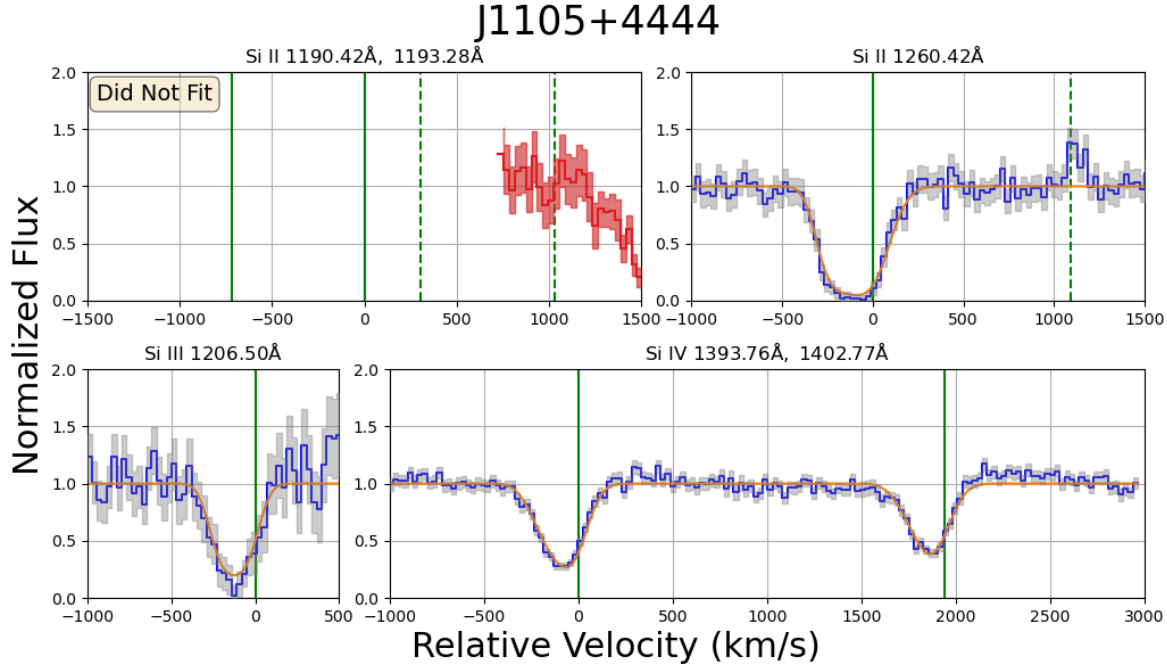


Figure 32: SALT fits for J1105+4444. The Si II 1190.42Å/1193.28Å doublet was not fit due to lack of data in the region of interest.

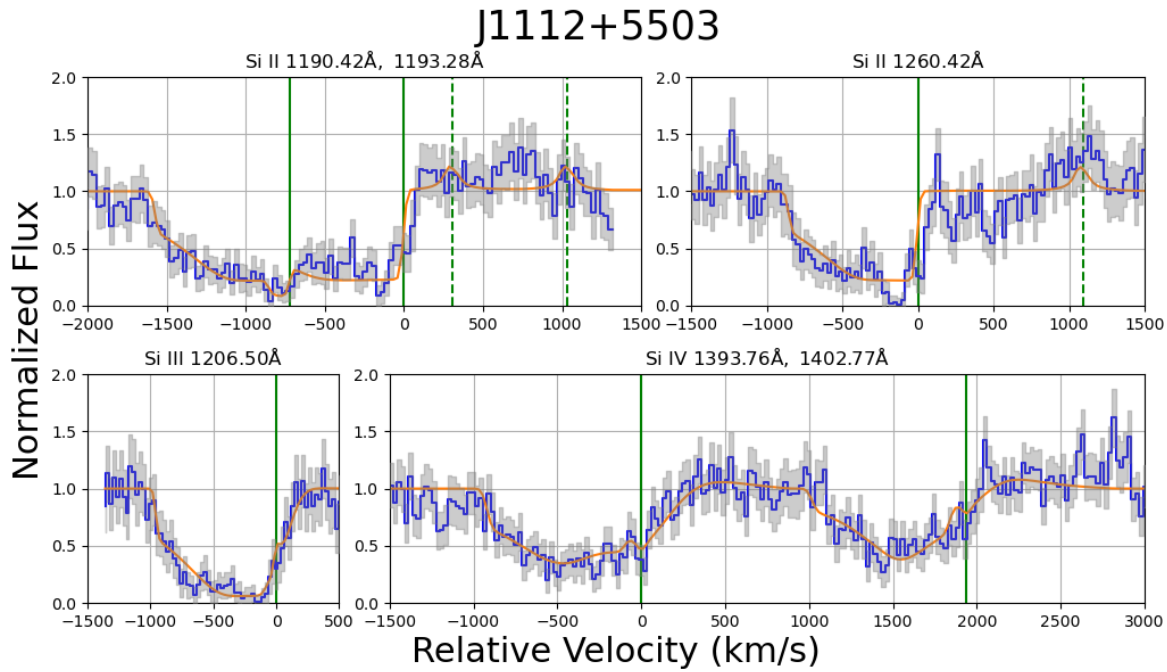


Figure 33: SALT fits for J1112+5503.

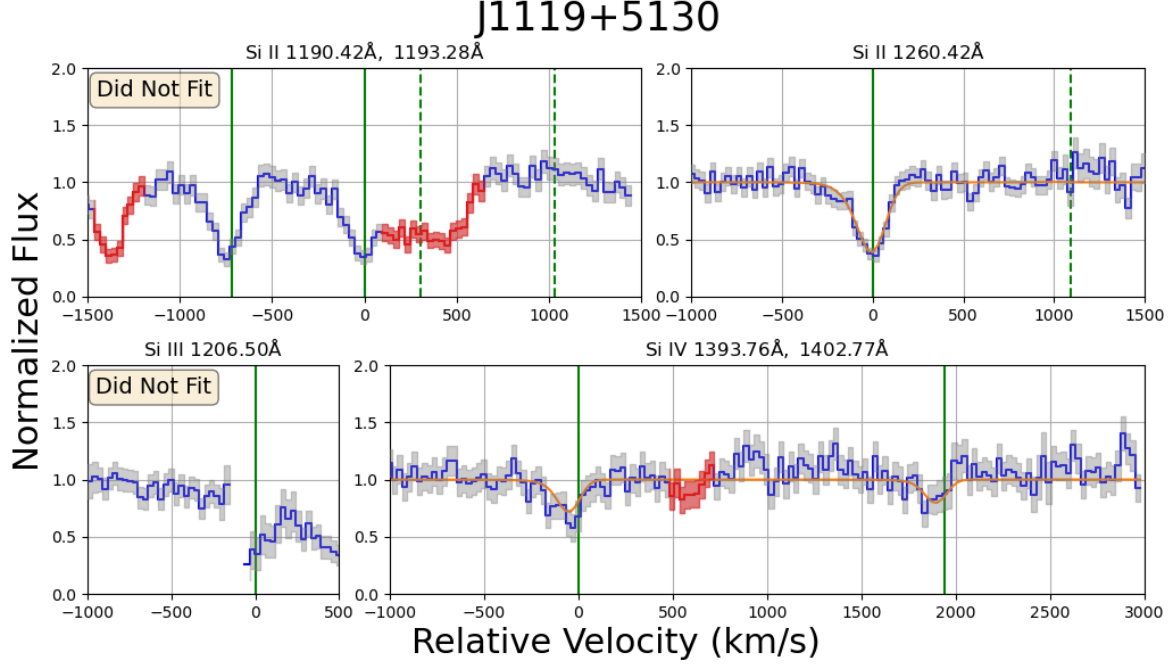


Figure 34: SALT fits for J1119+5130. The Si II 1190.42Å/1193.28Å doublet was not fit due to Milky Way contamination. The Si III 1206.50Å line was not fit due to lack of data in the region of interest.

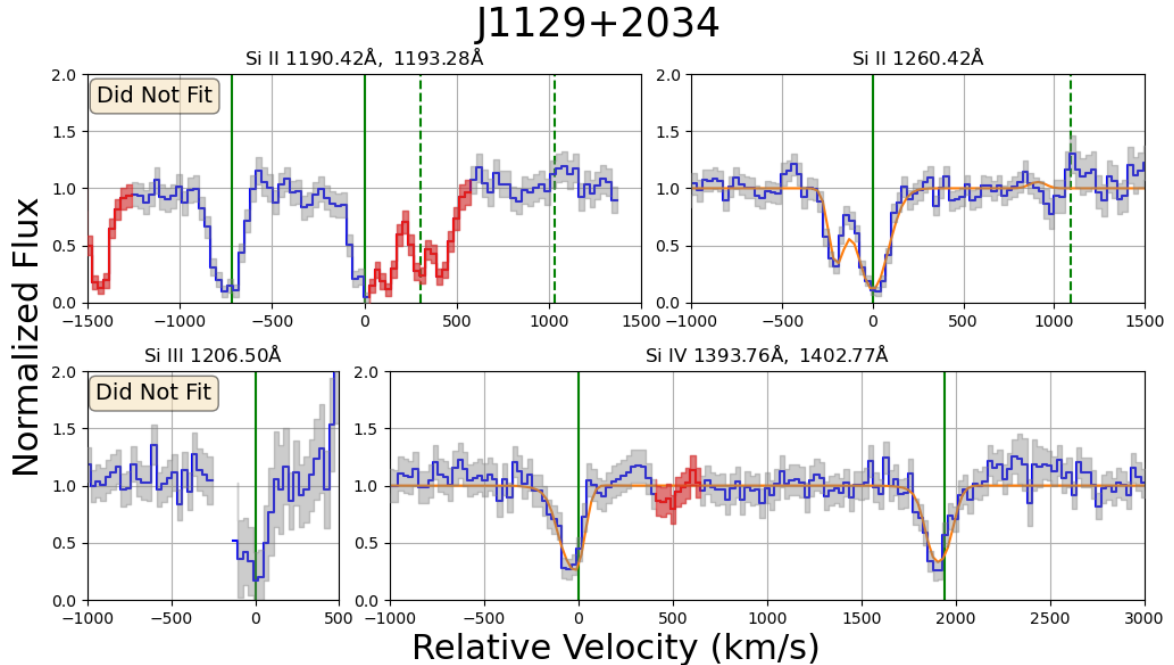


Figure 35: SALT fits for J1129+2034. The Si II 1190.42Å/1193.28Å doublet was not fit due to Milky Way contamination. The Si III 1206.50Å line was not fit due to lack of data in the region of interest.

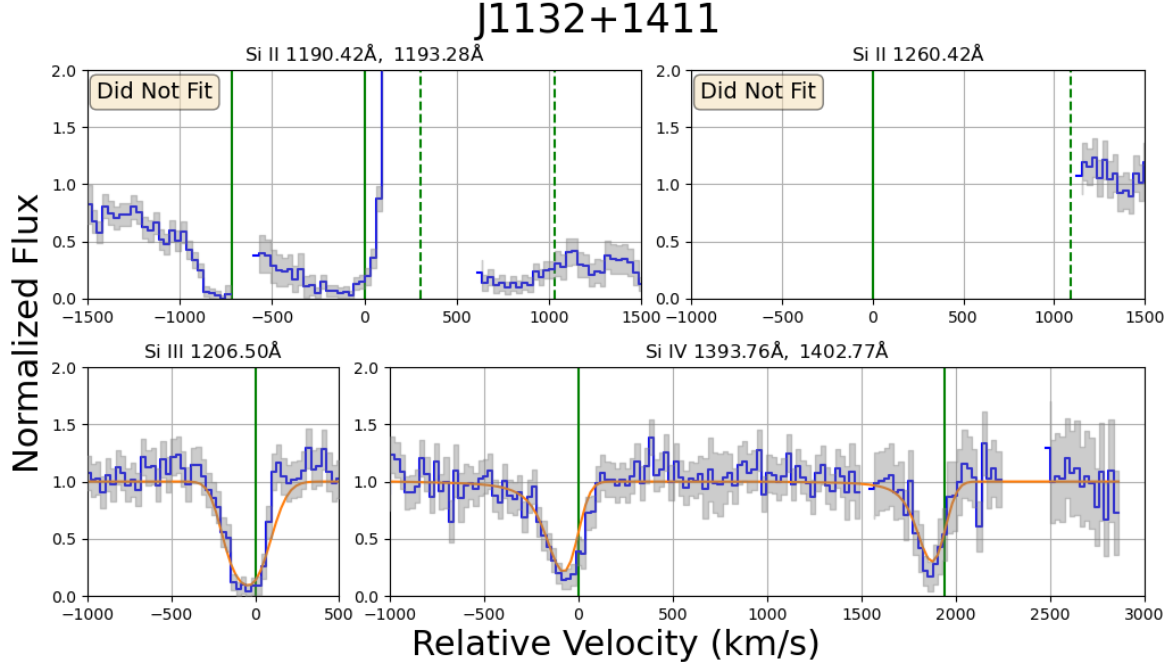


Figure 36: SALT fits for J1132+1411. The Si II 1190.42Å/1193.28Å doublet and the 1260.42Å line were not fit due to lack of data in the region of interest and the geocoronal Lyman α line

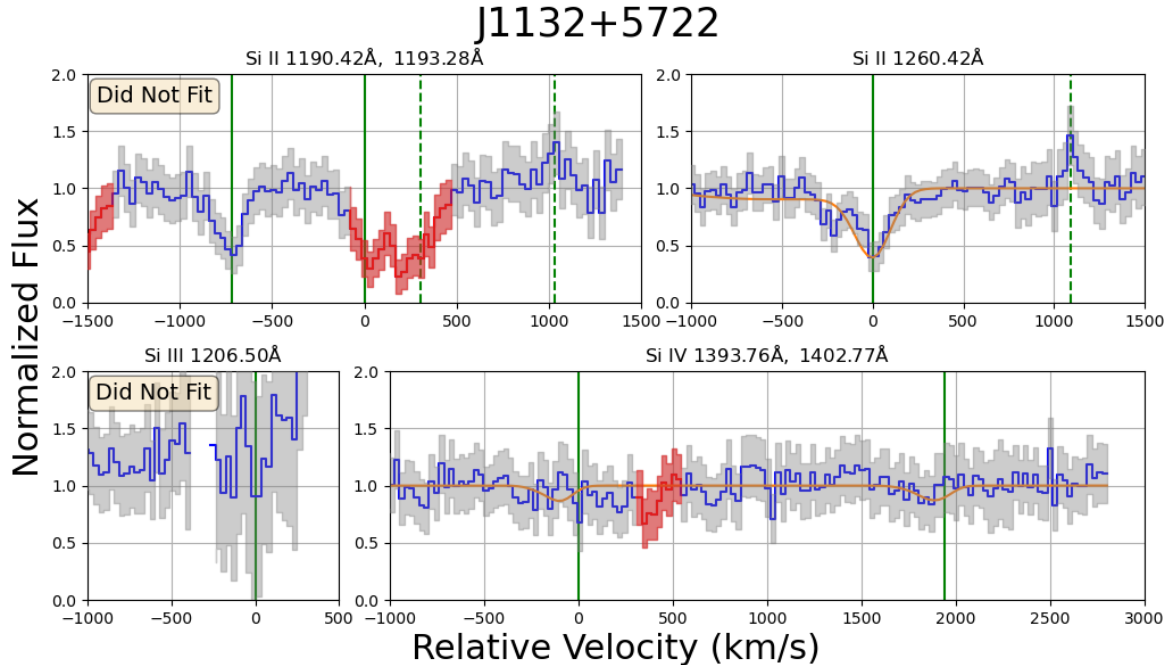


Figure 37: SALT fits for J1132+5722. The Si II 1190.42Å/1193.28Å doublet was not fit due to Milky Way contamination. The Si III 1206.50Å line was not fit due to noise.

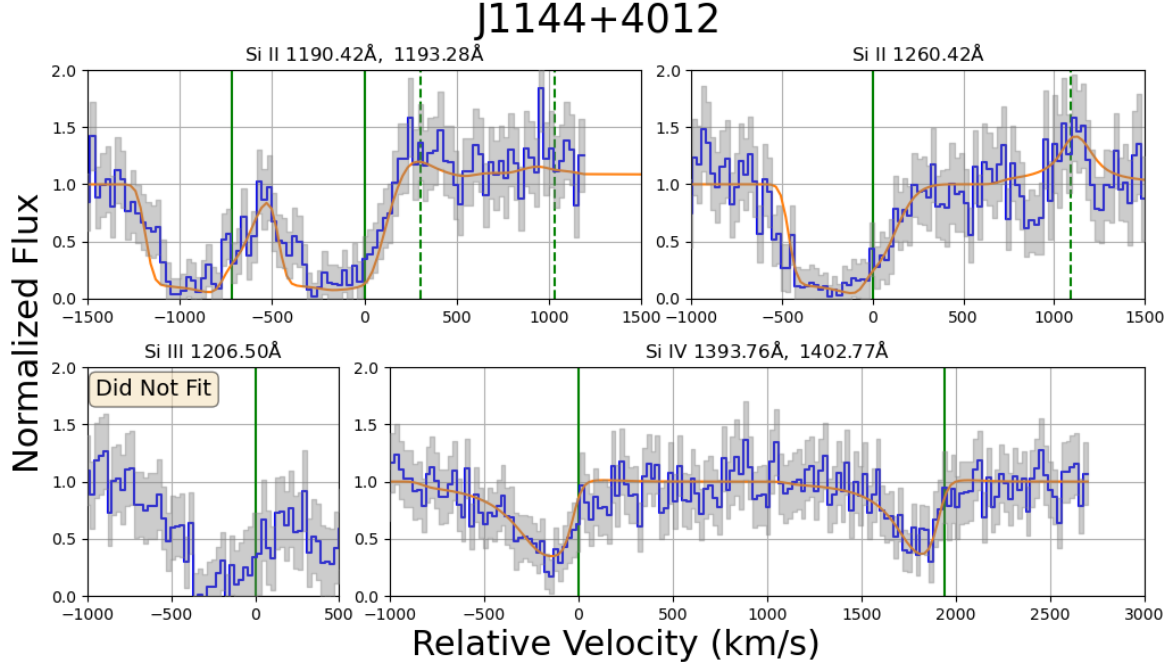


Figure 38: SALT fits for J1144+4012. The Si III 1206.50 \AA line was not fit due to interference from the nearby geocoronal Lyman α line.

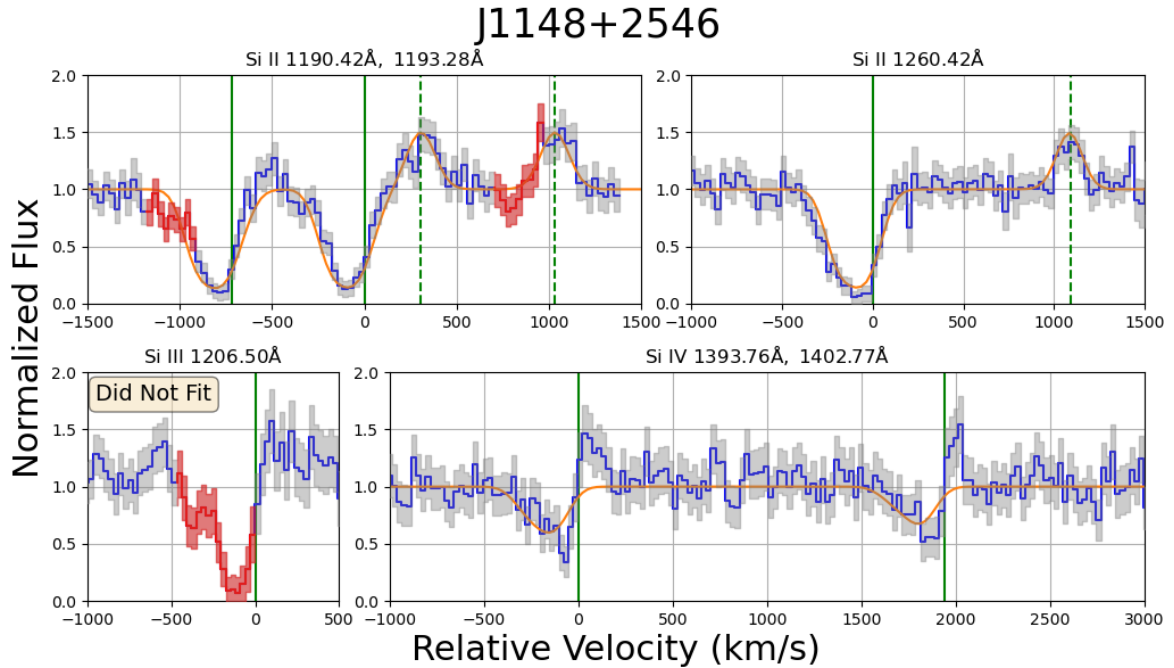


Figure 39: SALT fits for J1148+2546. The Si III 1206.50 \AA line was not fit due to Milky Way contamination.

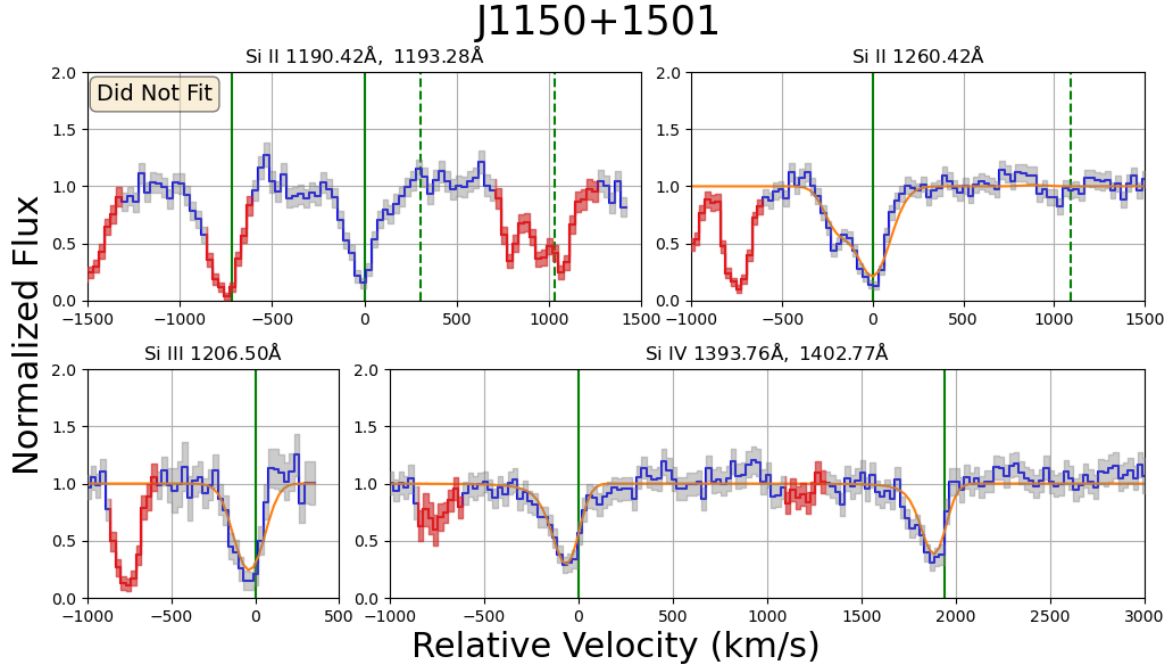


Figure 40: SALT fits for J1150+1501. The Si II 1190.42Å/1193.28Å doublet was not fit due to Milky Way contamination.

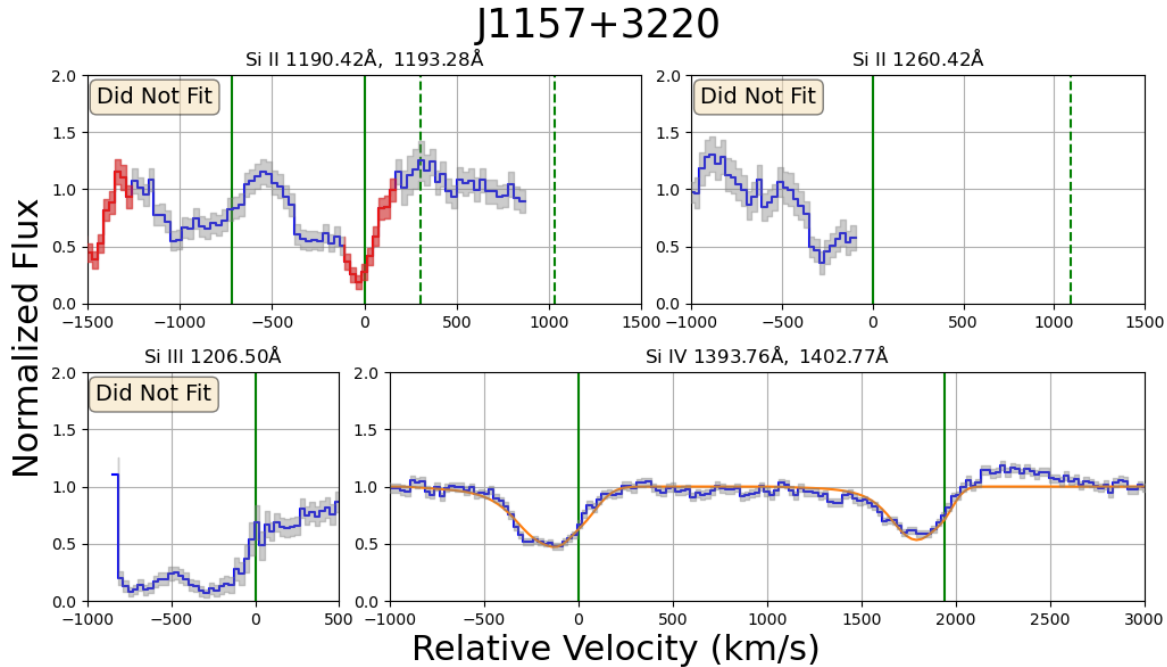


Figure 41: SALT fits for J1157+3220. The Si II 1190.42Å/1193.28Å doublet and the 1260.42Å line were not fit due to lack of data in the region of interest and Milky Way contamination. The Si III 1206.50Å line was not fit due to interference from the nearby geocoronal Lyman α line.

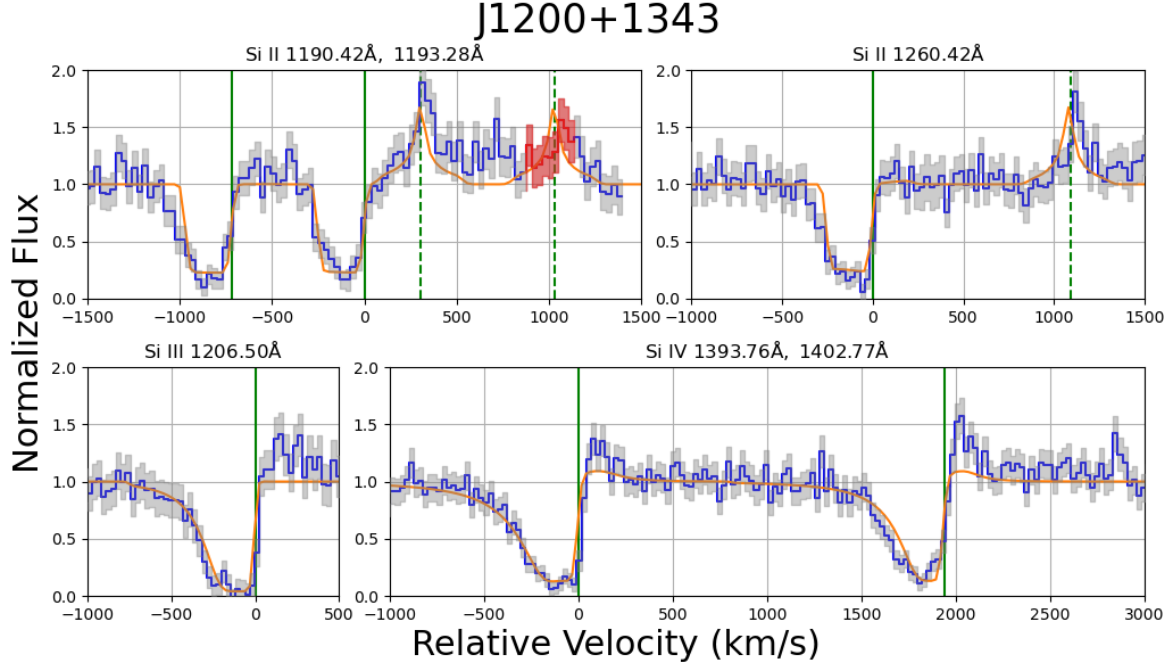


Figure 42: SALT fits for J1200+1343.

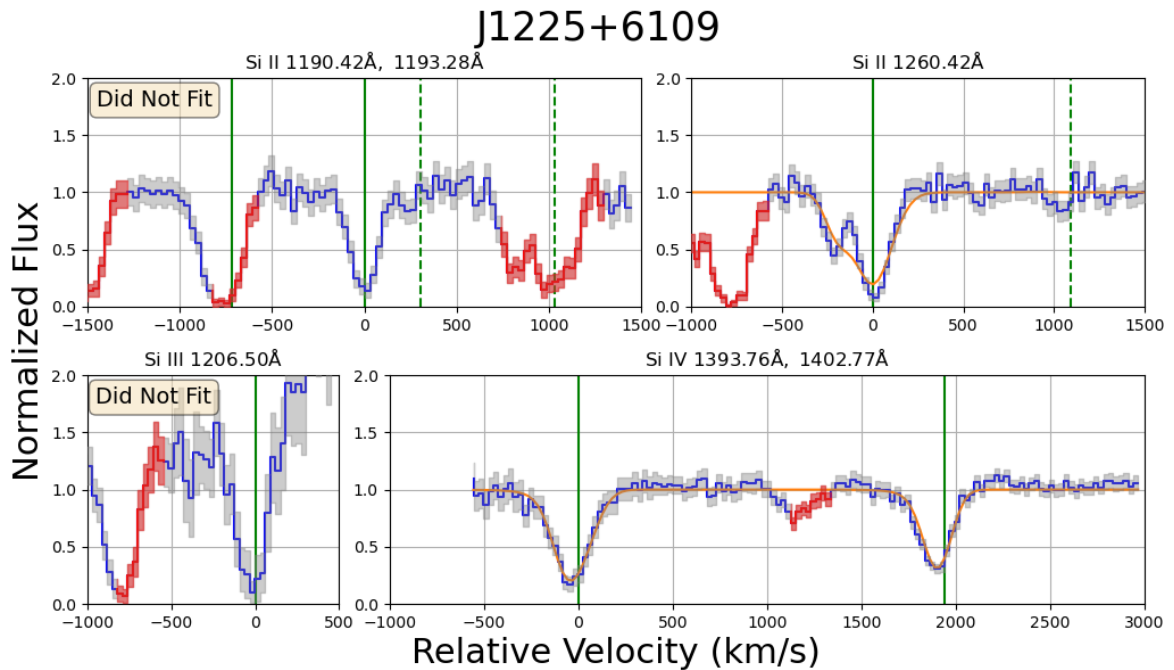


Figure 43: SALT fits for J1225+6109. The Si II 1190.42Å/1193.28Å doublet was not fit due to Milky Way contamination. The Si III 1206.50Å line was not fit due to interference from the nearby geocoronal Lyman α line.

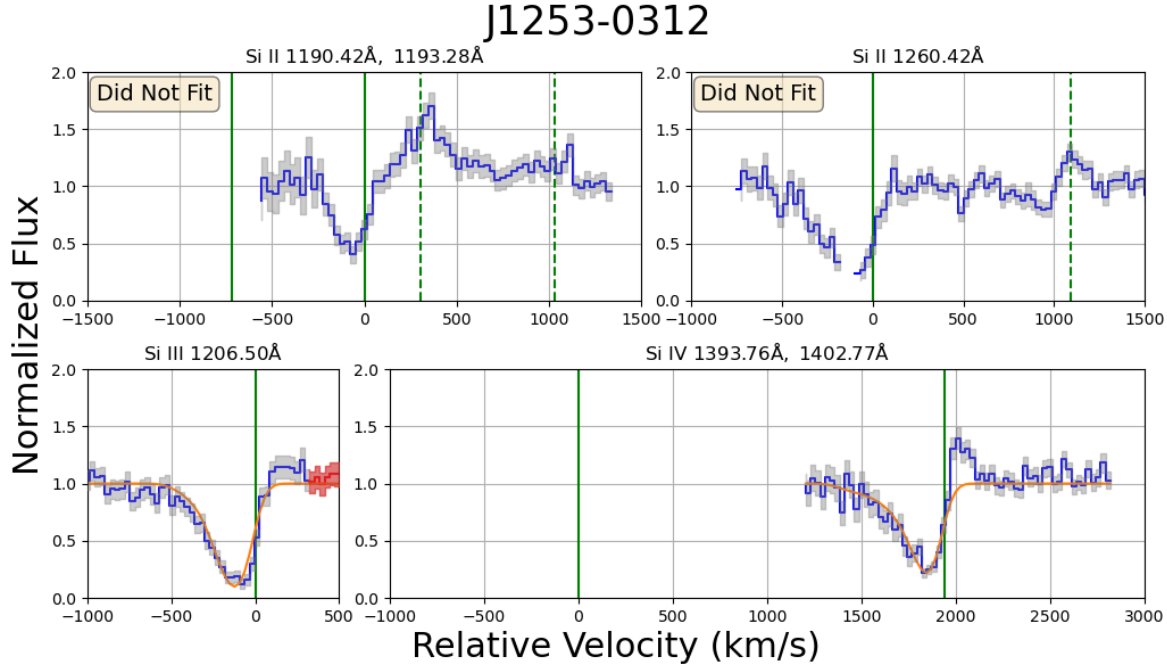


Figure 44: SALT fits for J1253-0312. The Si II 1190.42Å/1193.28Å doublet and the 1260.42Å line were not fit due to lack of data in the region of interest.

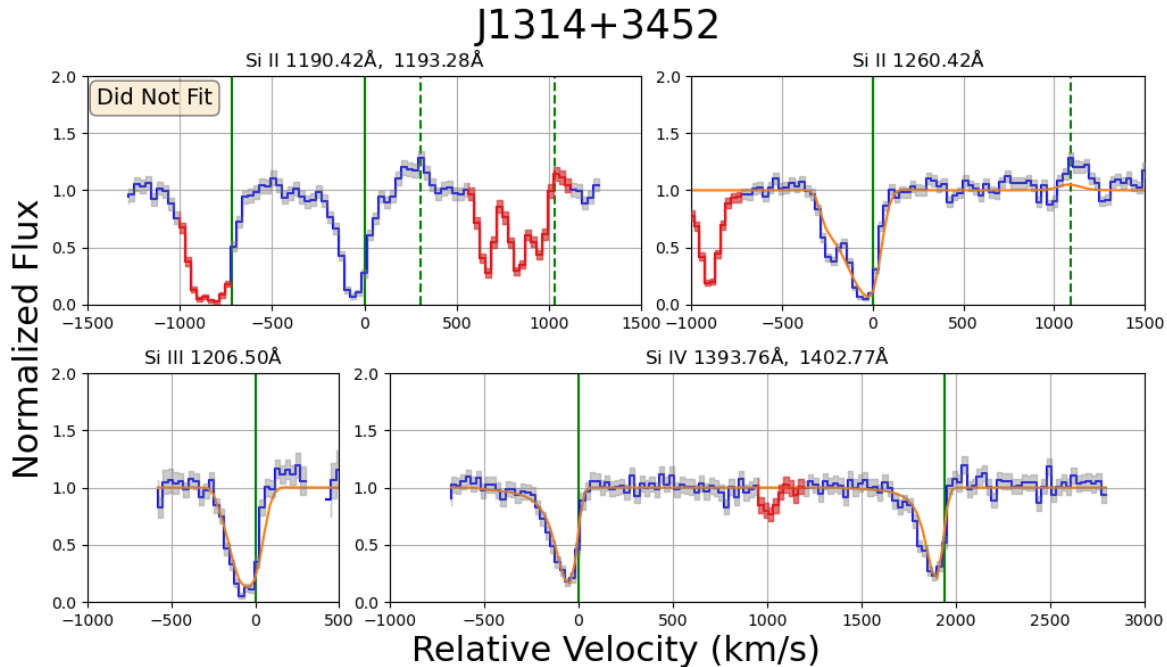


Figure 45: SALT fits for J1314+3452. The Si II 1190.42Å/1193.28Å doublet was not fit due to Milky Way contamination.

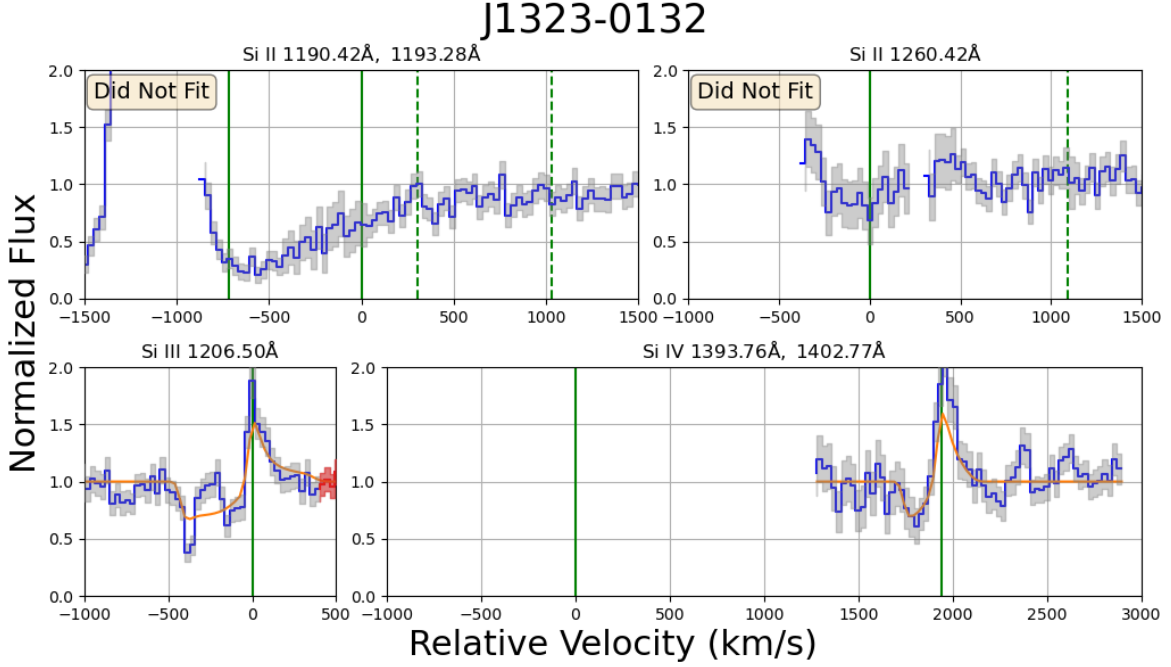


Figure 46: SALT fits for J1323-0132. The Si II 1190.42Å/1193.28Å doublet and the 1260.42Å line were not fit due to lack of data in the region of interest and the geocoronal Lyman α line.

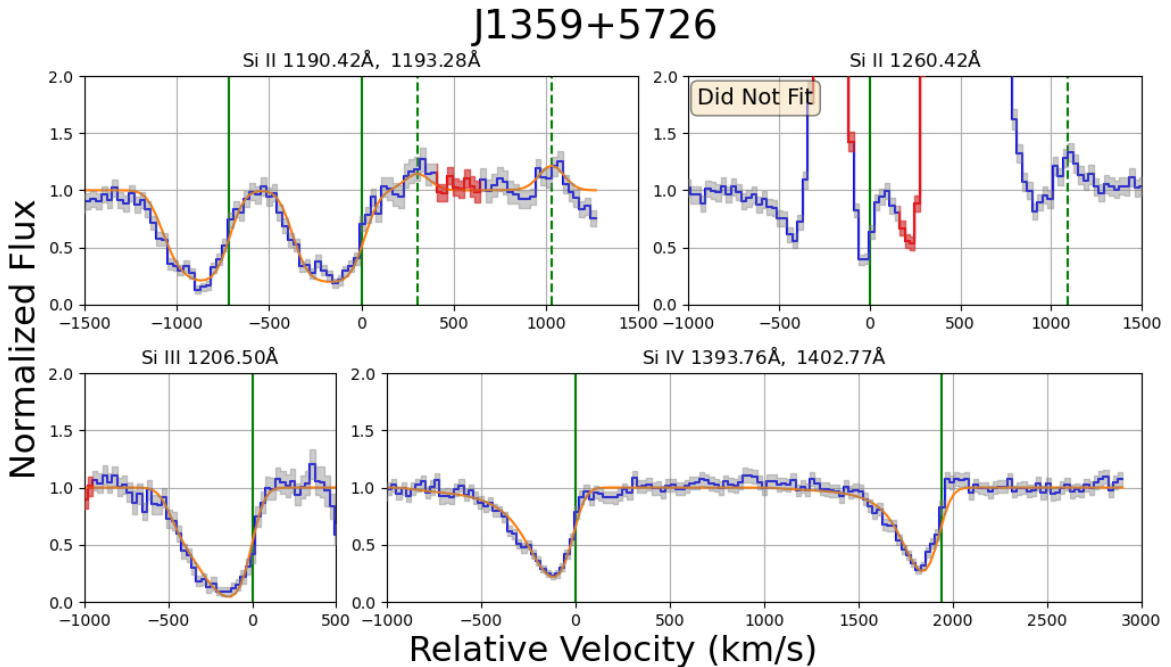


Figure 47: SALT fits for J1359+5726. The Si II 1260.42Å line was not fit due to the presence of the geocoronal Lyman α line.

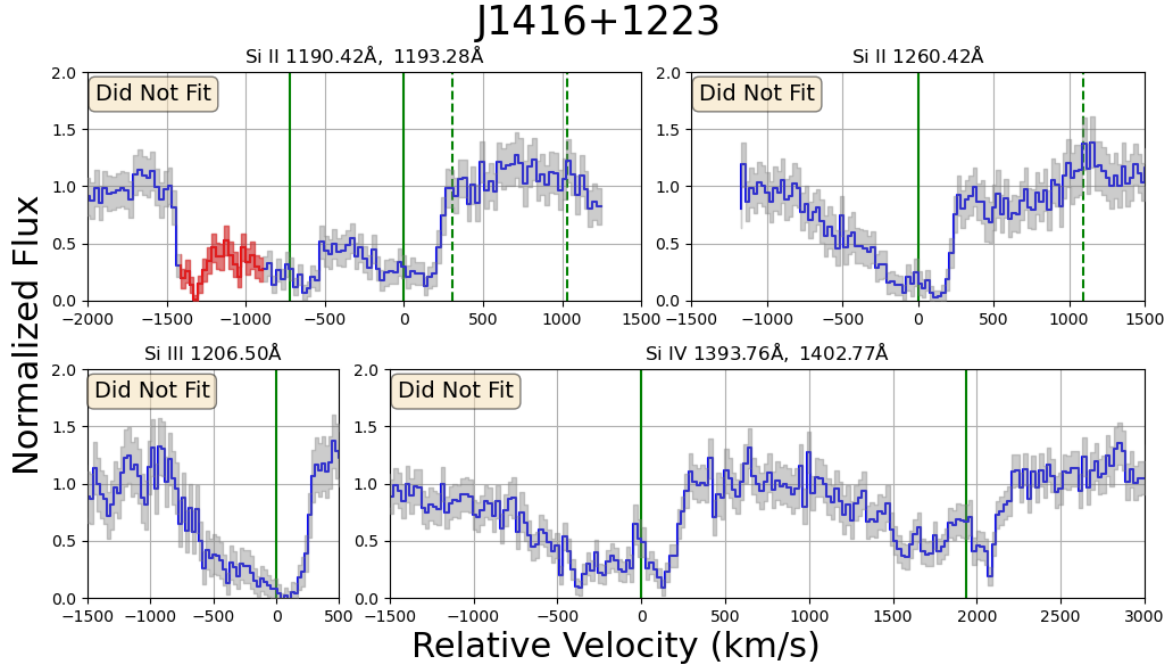


Figure 48: No SALT fits were made for J1416+1223. The spectra is more indicative of a galactic inflow than a galactic outflow (see the comment in Section 3).

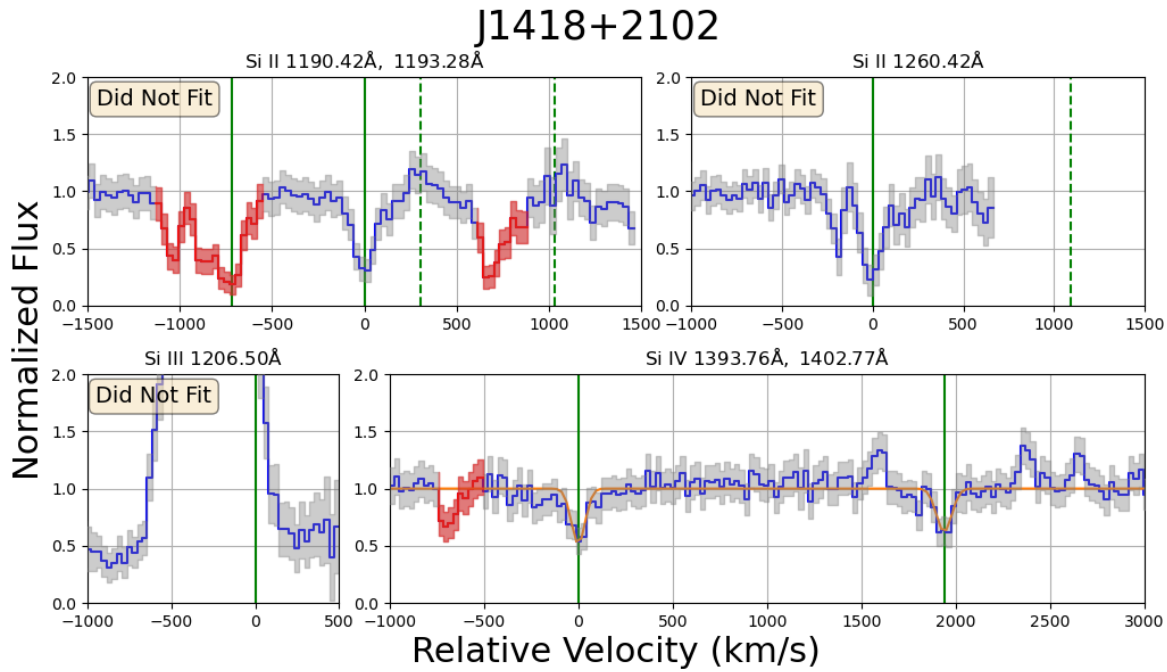


Figure 49: SALT fits for J1418+2102.

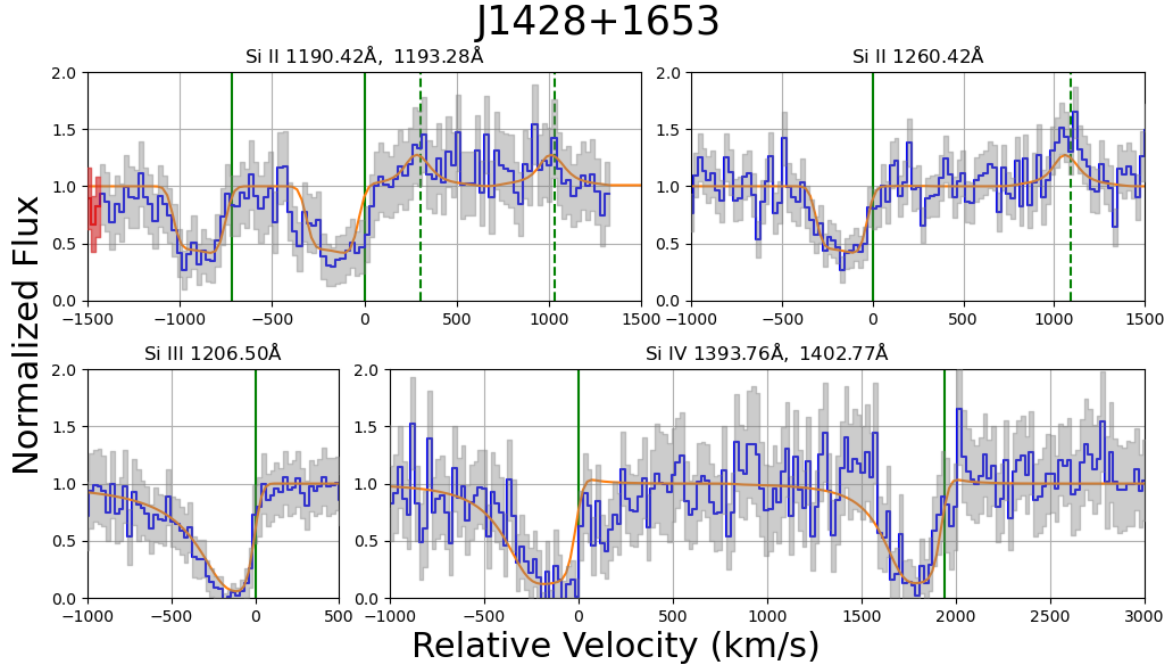


Figure 50: SALT fits for J1428+1653.

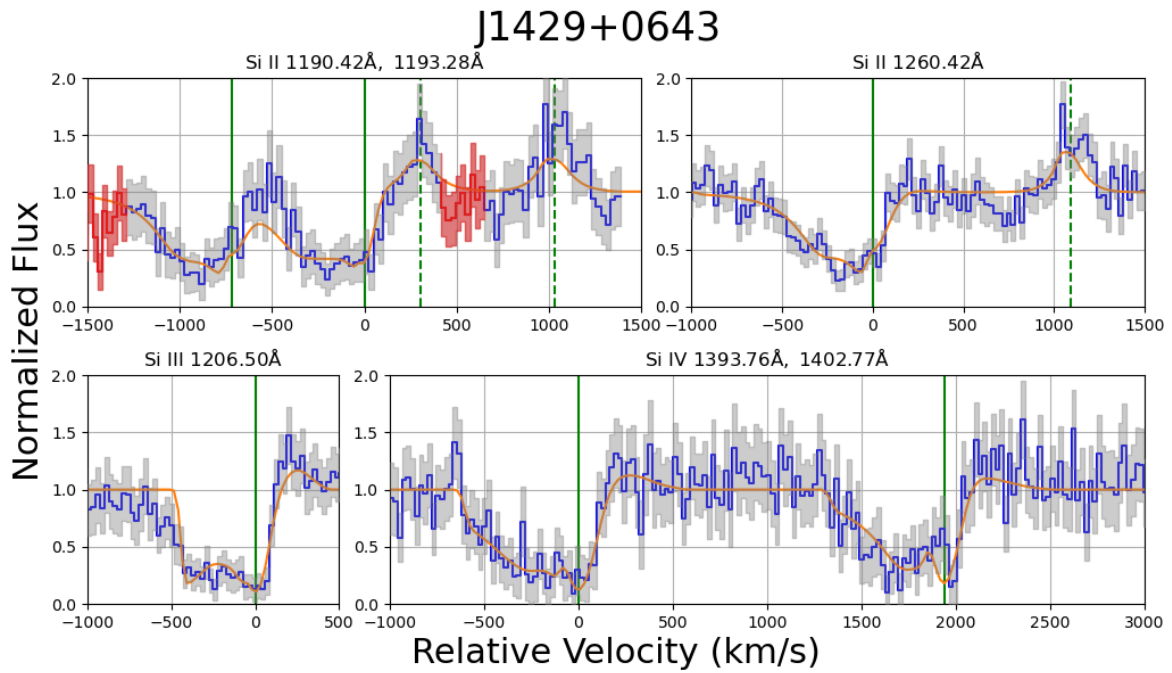


Figure 51: SALT fits for J1429+0643.

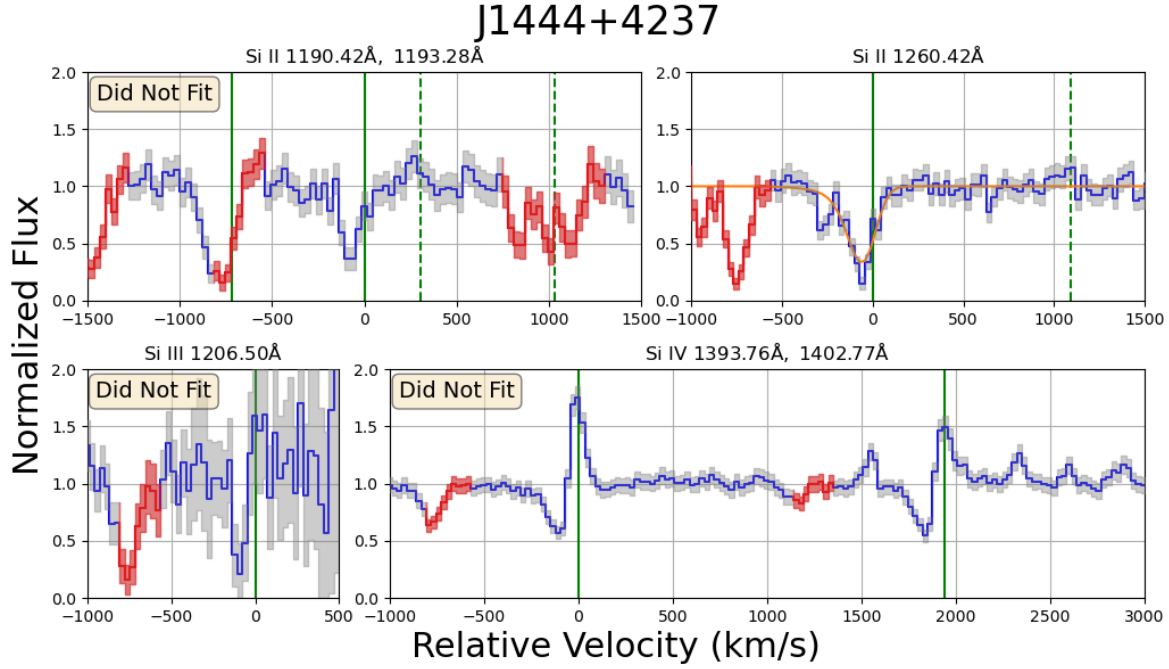


Figure 52: SALT fits for J1444+4237.

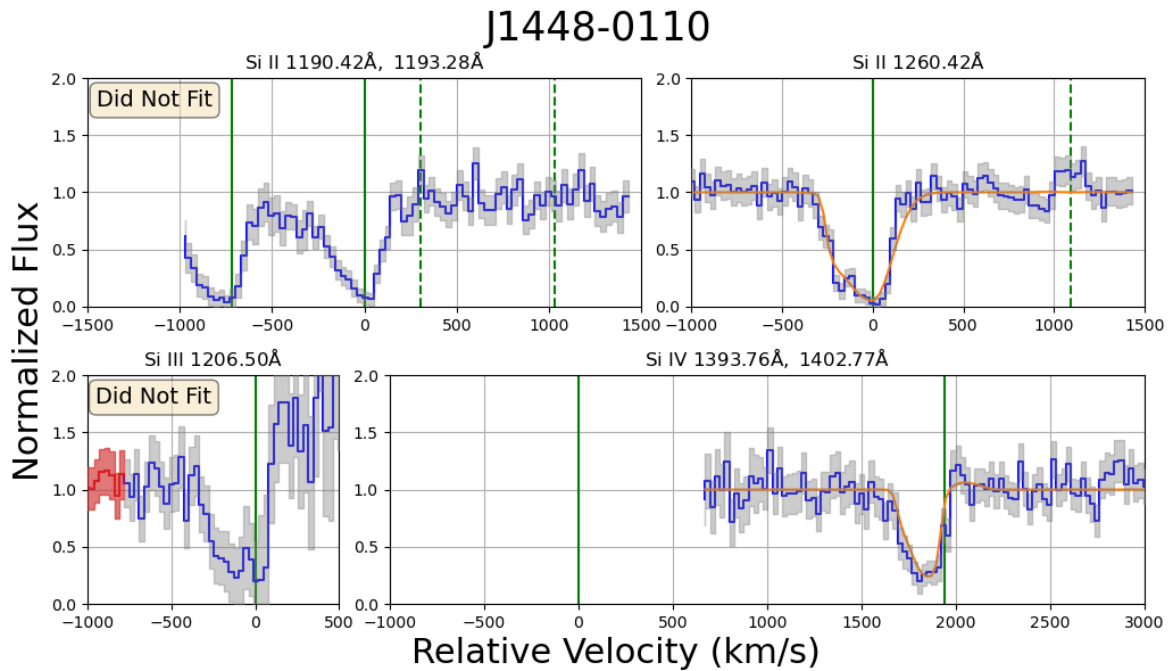


Figure 53: SALT fits for J1448-0110.

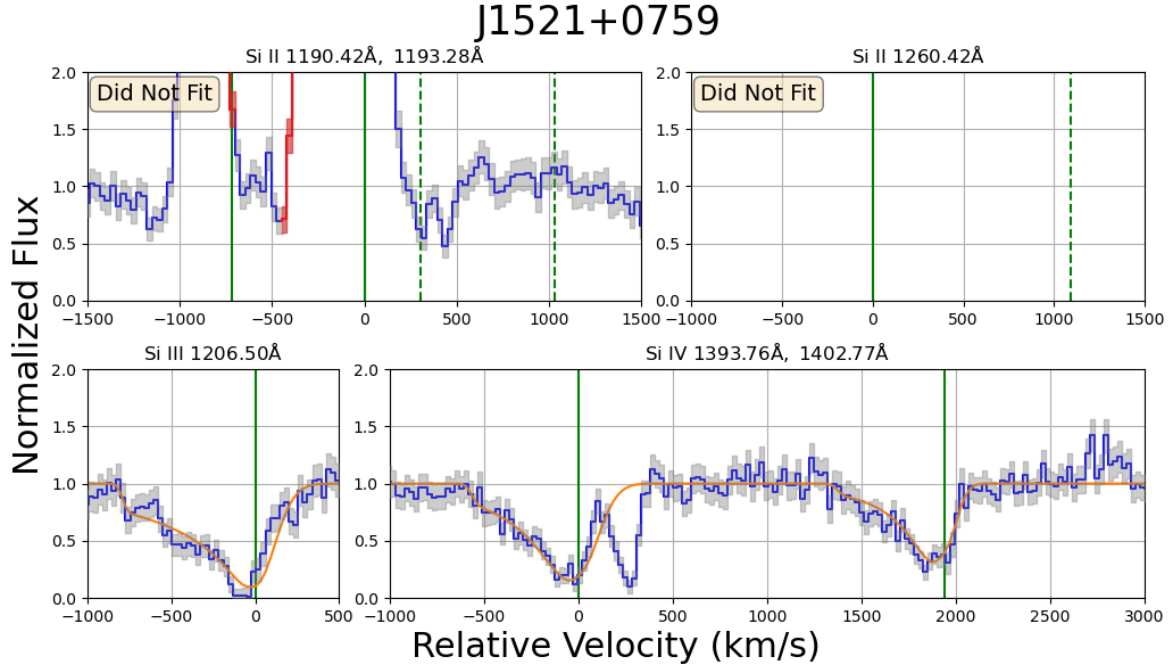


Figure 54: SALT fits for J1521+0759.

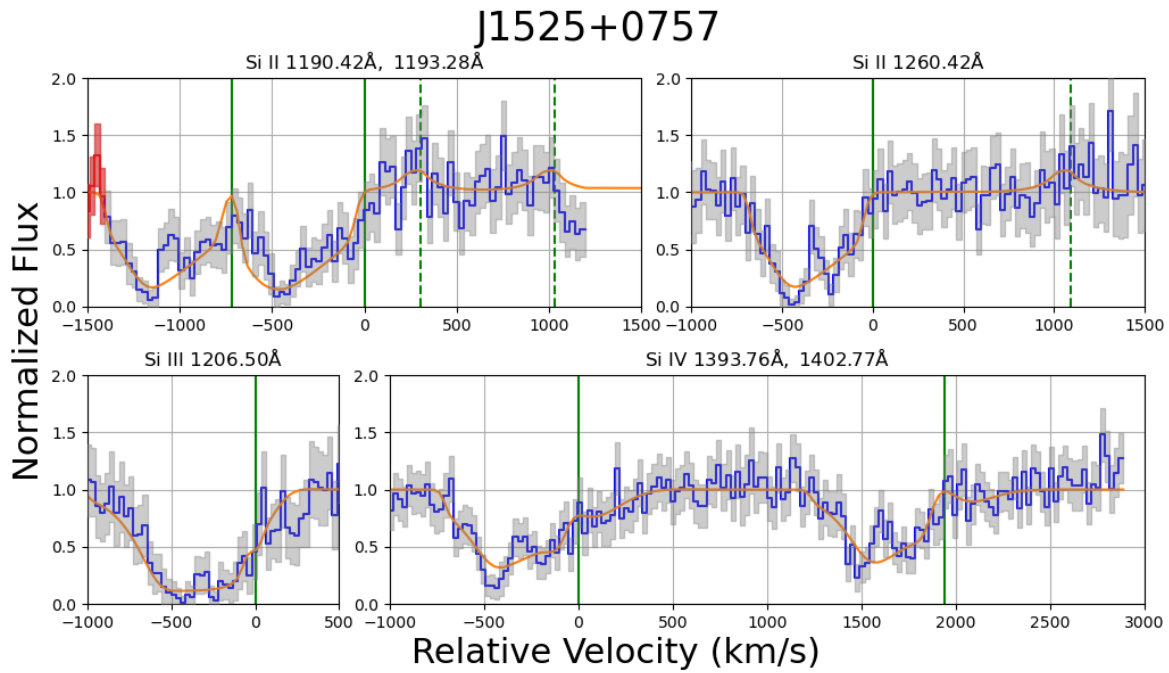


Figure 55: SALT fits for J1525+0757.

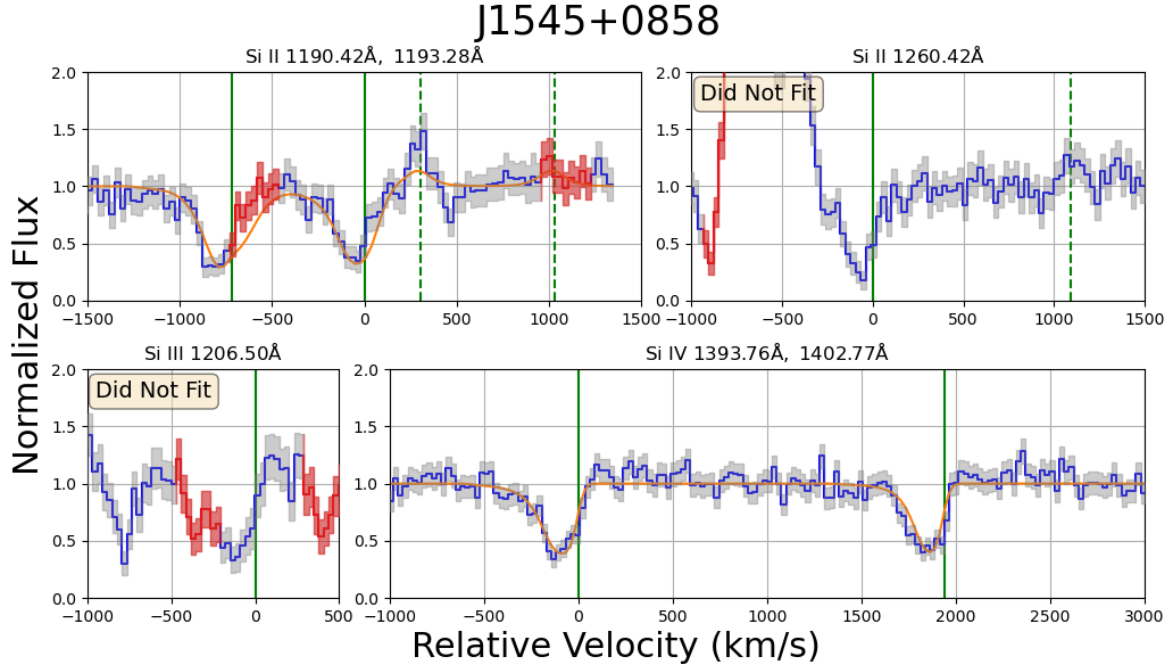


Figure 56: SALT fits for J1545+0858.

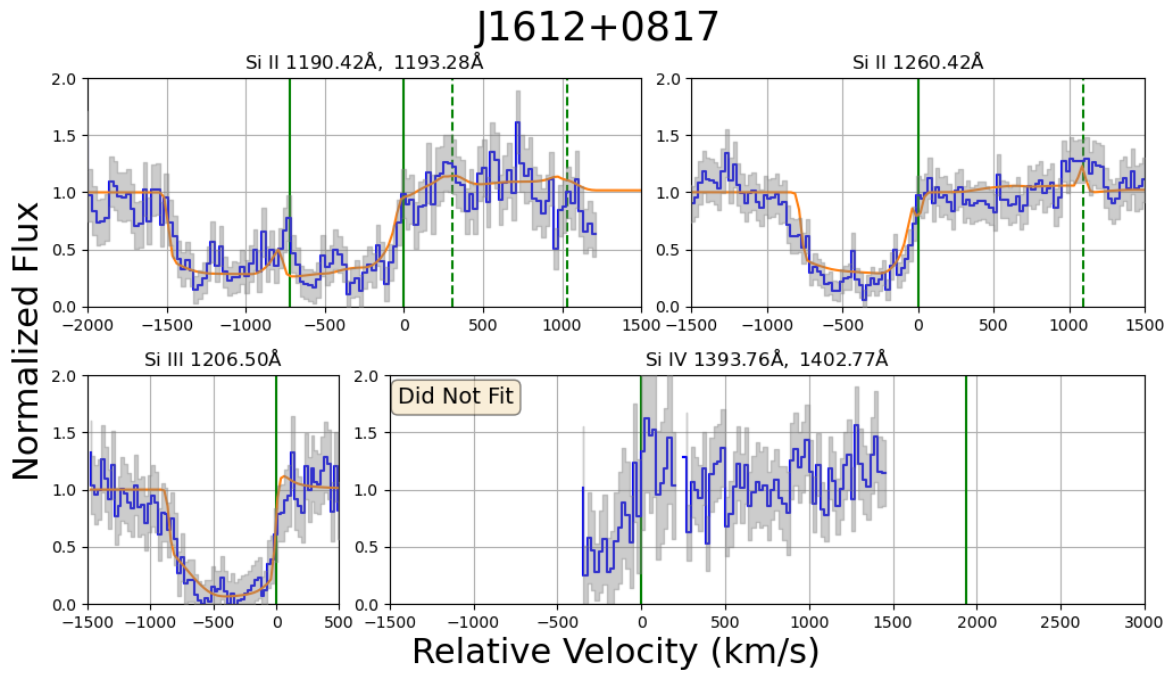


Figure 57: SALT fits for J1612+0817.

REFERENCES

- Berg, D. A., James, B. L., King, T., et al. 2022, ApJS, 261, 31. doi:10.3847/1538-4365/ac6c03
- Burchett, J. N., Rubin, K. H. R., Prochaska, J. X., et al. 2021, ApJ, 909, 151. doi:10.3847/1538-4357/abd4e0
- Calzetti, D. 1997, The ultraviolet universe at low and High redshift, 408, 403. doi:10.1063/1.53764
- Carr, C., Scarlata, C., Panagia, N., et al. 2018, ApJ, 860, 143. doi:10.3847/1538-4357/aac48e
- Carr, C., Scarlata, C., Henry, A., et al. 2021, ApJ, 906, 104. doi:10.3847/1538-4357/abc7c3
- Carr, C. & Scarlata, C. 2022, arXiv:2209.14485
- Chisholm, J., Tremonti, C. A., Leitherer, C., et al. 2017, MNRAS, 469, 4831. doi:10.1093/mnras/stx1164
- Chisholm, J., Bordoloi, R., Rigby, J. R., et al. 2018, MNRAS, 474, 1688. doi:10.1093/mnras/stx2848
- Foreman-Mackey, D., Hogg, D. W., Lang, D., et al. 2013, PASP, 125, 306. doi:10.1086/670067
- Hayward, C. C. & Hopkins, P. F. 2017, MNRAS, 465, 1682. doi:10.1093/mnras/stw2888
- Heckman, T. M., Alexandroff, R. M., Borthakur, S., et al. 2015, ApJ, 809, 147. doi:10.1088/0004-637X/809/2/147
- Hopkins, P. F., Kereš, D., Oñorbe, J., et al. 2014, MNRAS, 445, 581. doi:10.1093/mnras/stu1738
- Ivezić, Ž., Connelly, A. J., VanderPlas, J. T., et al. 2014, Statistics, Data Mining, and Machine Learning in Astronomy, by Z. Ivencić et al. Princeton, NJ: Princeton University Press, 2014
- Leitherer, C., Schaerer, D., Goldader, J. D., et al. 1999, ApJS, 123, 3. doi:10.1086/313233
- Martin, C. L. 2005, ApJ, 621, 227. doi:10.1086/427277
- McKinney, J. H., Jaskot, A. E., Oey, M. S., et al. 2019, ApJ, 874, 52. doi:10.3847/1538-4357/ab08eb
- Murray, N., Quataert, E., & Thompson, T. A. 2005, ApJ, 618, 569. doi:10.1086/426067
- Pandya, V., Fielding, D. B., Anglés-Alcázar, D., et al. 2021, MNRAS, 508, 2979. doi:10.1093/mnras/stab2714
- Rubin, K. H. R. 2017, Gas Accretion onto Galaxies, 430, 95. doi:10.1007/978-3-319-52512-9_5
- Scarlata, C. & Panagia, N. 2015, ApJ, 801, 43. doi:10.1088/0004-637X/801/1/43
- Shapley, A. E., Steidel, C. C., Pettini, M., et al. 2003, ApJ, 588, 65. doi:10.1086/373922
- Tumlinson, J., Peeples, M. S., & Werk, J. K. 2017, ARA&A, 55, 389. doi:10.1146/annurev-astro-091916-055240
- Xu, X., Heckman, T., Henry, A., et al. 2022, arXiv:2204.09181